UNIVERSITY OF OKLAHOMA

GRADUATE COLLEGE

INNOVATIVE GROWTH TECHNIQUES AND HETEROGENEOUS STRUCTURES FOR PbSe-BASED MWIR PHOTODETECTORS

A DISSERTATION

SUBMITTED TO THE GRADUATE FACULTY

in partial fulfillment of the requirements for the

Degree of

DOCTOR OF PHILOSOPHY

By

LANCE MCDOWELL

Norman, Oklahoma
2022

INNOVATIVE GROWTH TECHNIQUES AND HETEROGENEOUS STRUCTURES FOR PbSe-BASED MWIR PHOTODETECTORS

A DISSERTATION APPROVED FOR THE

SCHOOL OF ELECTRICAL AND COMPUTER ENGINEERING

BY THE COMMITTEE CONSISTING OF

Dr. Zhisheng Shi

Dr. Ian Sellers

Dr. Hong Liu

Dr. Patrick Skubic

Dr. Rui Yang

Abstract

Innovative Growth Techniques and Heterogeneous Structures for PbSe-Based MWIR Photodetectors

by

Lance McDowell

Lead-chalcogenide semiconductor materials such as PbSe are an attractive class of narrow band-gap semiconductors due to their unique optical and electrical properties, finding their way into numerous mid-wave infrared (MWIR) optoelectronic and topological device applications. While PbSe is a mature material system with research efforts dating back almost a century, the full potential of its physical properties has yet to be realized in fabricated devices. Much of the difficulty lies in the unique bonding nature and crystal structure of PbSe films, which gives both advantageous MWIR optoelectrical properties along with a limited selection of suitable substrates for high-quality growth. Further, PbSe homojunction devices on dissimilar substrates face issues with doping, where diffusion of PbSe dopants through defect channels inhibit the formation of an abrupt junction resulting in degraded device performance. Further, p-n heterojunction formation with PbSe is difficult due to the small bandgap of PbSe, resulting in a shortlist of suitable materials with the corresponding band alignment to form a type-II heterojunction. Even for material systems that share a suitable band alignment, issues often arise with dissimilar crystallinity, lattice constant, and thermal expansion coefficient. The dissimilarity between these films introduces large stress/ strain relations at the interface, resulting in the formation of cracks or dislocations which ruin the interface and bulk electrical properties. For these reasons, PbSe-based MWIR devices have been surpassed by more competitive material systems such as II-VI HgCdTe, and Sb-based type-II superlattices.

In this work, new methods for improving PbSe film quality are explored, along with the growth and design of new heterogeneous structures and MWIR photodetectors which may improve the PbSe-based MWIR sensing platform. Presented here will be a new approach for creating heterogeneous material structures with PbSe by molecular beam epitaxy (MBE). Demonstration of a new heterogenous p-n junction structure between mismatched germanium substrates and epitaxial lead selenide thin-films will be introduced utilizing a vicinal growth surface. Extending from this, epitaxial PbSe films with enhanced surface morphology will also be demonstrated on vicinal silicon substrates, showcasing record low surface defect densities compared to traditional growth on nominal silicon. Regarding the former, germanium will also serve as an active layer in the formation of a p-n heterojunction structure due to its suitable type-II band alignment with PbSe. However, large differences in lattice constant and thermal expansion coefficient will need to be addressed to form such a structure. These challenges are tackled by optimizing the surface kinetics of PbSe adatoms through high-temperature surface treatment, along with utilizing misfit accommodation steps induced by the periodic atomic step edges from the high degree of vicinal miscut of the germanium growth surface. Further, different structures and device applications of PbSe-based material systems will be explored, including the growth of a new PbOSe complex oxide thin-film via oxygen-plasma assisted MBE deposition. Fabrication of a single phase (cubic) all-epitaxial n-CdSe/p-PbSe heterojunction structure with room temperature MWIR detection capabilities will also be presented, along with the fabrication of MWIR transparent contacts using cadmium oxide thin-films for enhanced photodetector device design. The combined results of these efforts provide multiple avenues for the development of state-of-the-art MWIR PbSe-based photodetectors, enabling future commercial MWIR sensing capabilities with reduced size, weight, power consumption, and cost.

Table of Contents

CHAPTER PAGE

Table of Figures

1. Introduction to Lead Selenide

Lead Selenide has experienced fluctuations in popularity over the decades as a viable candidate for MWIR photodetector applications operating at near room-temperature. The attraction is largely due to the high-performance potential of PbSe films resulting from its low Auger coefficient when compared to other state-of-the-art material systems such as mercury cadmium telluride (MCT) and Sb-based type-II superlattices (T2SL). However, a well-known obstacle in realizing the high-performance potential of PbSe films is reducing the Shockley-Read-Hall (SRH) contribution below that of Auger contributions to achieve an Auger limited detector for near room-temperature operation. This challenge has resulted in a massive effort by the scientific community over many years to solve this problem, with a variety of innovative techniques and tricks developed by various research groups in effort to enhance PbSe material quality. However, no clear method has shown the ability to consistently produce high-quality PbSe films operating close to its Auger limit. The strongest candidate to date is the sensitized chemical bath deposited (CBD) PbSe photoconductors, which in 2014, showcased a record breaking detectivity of 4.2×10^{10} Jones at room temperature. However, this promising detectivity is overshadowed by the inconsistent nature of these PbSe films, with large inhomogeneity in both film property and pixel performance. For this reason, innovations in high-quality epitaxial PbSe films are the next logical step in the evolution of PbSe-based optoelectronic devices, taking advantage of growth methods such as molecular beam epitaxy (MBE) to produce PbSe films with high uniformity and extreme surface smoothness. With these films, higher relationships in pixel-pixel performance can be achieved, along with the design of more complex device structures and high-quality interface formation, allowing for photovoltaic detector fabrication.

I. MATERIAL PROPERTY

This chapter is dedicated to the characterization of material properties relevant to heterogeneous material growth and PbSe-based MWIR photodetector devices. The materials discussed here represent a few chosen material systems that are found to be an attractive avenue for high-yield epitaxial PbSe films with the potential to grow various heterojunction device structures for MWIR sensing applications. The properties discussed here are designed to link possible growth mechanisms with controlled growth parameters to better exploit the high-performance potential of PbSe films when surface and bulk defect densities are sufficiently suppressed. These properties include crystal structure, lattice parameter, thermal expansion coefficient, and band alignment. Growth-related properties and defects will also be discussed such as 2D and 3D growth modes, misfit dislocations, and dislocation slip systems.

II. LEAD SELENIDE AND ASSOCIATED GROWTH SURFACES

Structure and Properties of Lead Selenide

Lead Selenide is an IV-VI compound semiconductor material which shares the PbX structure of other lead-chalcogenides such as PbS, PbTe, and SnTe. Lead-chalcogenides all share a face-centered cubic unit cell with a NaCl “rock salt” crystal structure. For PbSe, each lead atom is surrounded by 6 selenium atoms in the crystal, and each selenium atom is surrounded by 6 lead atoms, resulting in the coordination number of PbSe to be 6:6. This contrasts with most other semiconductors such as column IV, III-Vs, and II-VIs which have only 4 bonds per atom and four-

fold coordination. The result of this is the formation of 90° angles between bond orbitals producing the iconic Pb-salt crystal structure as depicted in Figure 1.1.

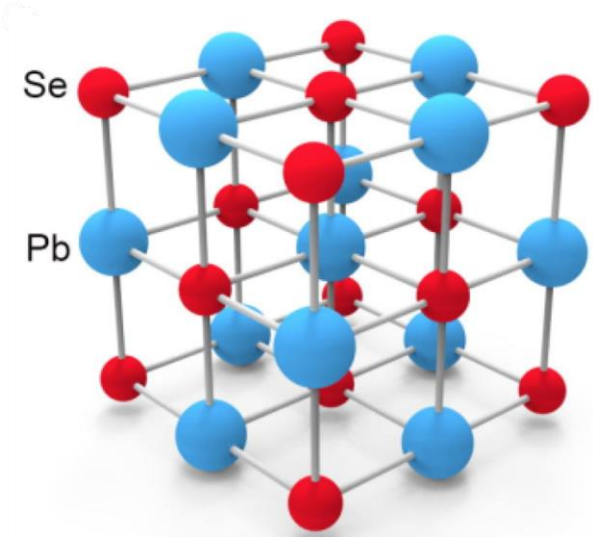

Figure 1.1 ***PbSe Crystal Structure*** *(Pb: blue Se: red)*

Interestingly, the bonding nature of lead and selenium atoms introduces some unique effects due to the small electronegativity difference between Pb atoms (2.23) and Se atoms (2.55). The small difference in electronegativity between these atoms does not allow for sufficient charge transfer to form an ionic solid like NaCl, despite the shared crystal structure. Instead, a type of metavalent bonding ensues, which describes the unique bonding nature of materials such as PbSe whose charge transfer between neighboring atoms cannot be fully described with the metallic, ionic, and covalent bonding schemes[1].

The band structure produced by the cation-anion interactions in PbSe results in a direct narrow bandgap material system, with a positive temperature coefficient which can be approximated by the following Preier's equation [2]:

$$E_g(T) = 125 + \sqrt{400 + 0.25T^2} \quad \ldots\ldots\ldots\ldots\ldots \quad 1.1$$

Here, $E_g(T)$ is the temperature dependent energy bandgap in meV, giving a room temperature bandgap for PbSe of 0.276 eV. The positive temperature coefficient of PbSe results in a shrinking of the bandgap at lower temperatures, resulting in a red shift of the optical absorption band. This effect has been observed in real world devices, with radiometric measurements of PbSe based photodetectors showing the cut-off and peak optical absorption red shifted to longer wavelengths at lower operating temperatures[3].

Nucleation

Understanding the nature in which epitaxial growth occurs and the forces governing crystal formation is vital to producing high-quality epitaxial films. The initial stage of crystal growth is known as nucleation, where a small number of atoms incident on a substrate (adatoms) arrange themselves forming a crystalline solid. The nucleation process is perhaps the most crucial step in crystal growth, as it sets the foundation for subsequent deposited layers. There are many factors that influence the nucleation process ranging from substrate and material selection to growth environment conditions. However, the initial deposition can be simplified by considering that adatoms only have two possible outcomes when incorporating into the film. First, adatoms incident on the substrate can interact with another adatom (nucleation) forming an island or growth site. Second, adatoms can interact with an already formed island contributing to layer growth. The competition between nucleation (island formation), and layer growth, are heavily dependent on the adatom diffusion coefficient along the growth surface. Since this work seeks to investigate methods for optimizing control of deposited films, it is beneficial to write equations expressing these outcomes to better understand island formation. The rate that adatoms interact with either an island or another adatom can be expressed by the following equation,

$$\frac{n}{\tau_A} = 2W_{AA} + W_{AI} \quad \ldots\ldots\ldots\ldots 1.2$$

Where $n = R\tau_A$ is the number of adatoms per unit area, R is the deposition rate, τ_A is the adatom lifetime, W_{AA} is the adatom-to-adatom collision rate, and, W_{AI} is the adatom to island collision rate. The average area occupied by an adatom or island is $\frac{1}{na^2}$ and $\frac{1}{Na^2}$ respectively, where N is the number of islands per unit area.

In an adatom's lifetime, it will visit a number of potential interaction sites before finally interacting with one. The number of sites visited is dependent on its diffusion coefficient and is related by the following equation,

$$\Gamma\tau_A = \frac{D\tau_A}{a^2} \quad \ldots\ldots\ldots\ldots 1.3$$

Where Γ is the number of sites visited per unit time, and D is the surface diffusion coefficient.

The probability of adatom-to-adatom interaction is then expressed as,

$$\frac{\frac{D\tau_A}{a^2}}{\frac{1}{na^2}} = nD\tau_A \quad \ldots\ldots\ldots\ldots 1.4$$

and an adatom interacting with an existing island can be expressed as,

$$\frac{\frac{D\tau_A}{a^2}}{\frac{1}{Na^2}} = ND\tau_A \quad \ldots\ldots\ldots\ldots 1.5$$

After some substitutions, the final relationship for island density formation can be expressed as,

$$N \sim \left(\frac{R}{D}\right)^{\frac{1}{3}} \quad \ldots\ldots\ldots\ldots\ldots\ldots 1.6$$

This result shows that island density is largely dependent on deposition rate and surface diffusion. To reduce island density resulting in larger grain growth or to encourage two-dimensional growth, the deposition rate should be sufficiently low so adatoms have time to find and interact with existing islands before encountering another adatom. Subsequently, enhanced surface mobility

from increasing D allows for adatoms to find and interact with potential growth sites within a shorter amount of time, promoting layer growth over island formation.

Growth Modes

Although equation 1.6 gives some insight into the initial nucleation process, a more detailed investigation of the growth process requires analysis of the substrate-film interaction energies. In this model, there are three terms of interest, $\gamma_{substrate}$, γ_{film}, and $\gamma_{interface}$, which describe the surface energy of the substrate, film, and the interfacial energy between them respectively. The relationship between these three energies will determine the growth mode of the film on the substrate, as well as influence subsequent deposition layers [4]. The three fundamental growth modes resulting from these energies are detailed below.

Frank-Van der Merwe mode: Layer-by-layer growth

$$\gamma_{substrate} \geq \gamma_{film} + \gamma_{interface}$$

Figure 1.2 ***Schematic drawing of Frank-Van der Merwe growth mode.***

When the surface energy of the substrate is greater than the deposited film and interface energy, adatoms can easily diffuse across the surface (wetting) and form a relatively uniform layer. This mode is most characterized by single crystalline growth, as interface energies between film and substrate are relatively low due to either careful substrate selection or control of growth parameters. However, as is often the case in polycrystalline film deposition, substrates with

increased lattice mismatch or difference in thermal expansion coefficient may induce larger interface energies during deposition, resulting in the following growth mode.

Vollmer-Weber mode: island growth

$$\gamma_{substrate} < \gamma_{film} + \gamma_{interface}$$

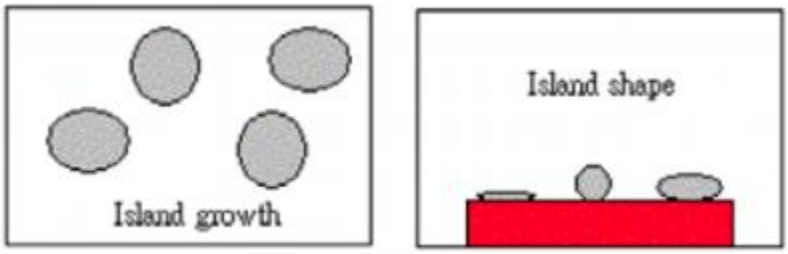

Figure 1.3 ***Schematic drawing of Vollmer-Weber growth mode.***

When film and interfacial energies exceed the substrate surface energy, adatom surface diffusion becomes weaker, resulting in non-wetting of the surface contributing to island growth. Although islands may coalesce as growth continues, neighboring islands with differing orientations may instead form interfaces between them leading to grain growth.

Stranski-Krastanov (SK) mode: transition growth

Initially: $\gamma_{substrate} \geq \gamma_{film} + \gamma_{interface}$

Subsequently: $\gamma_{substrate} < \gamma_{film} + \gamma_{interface}$

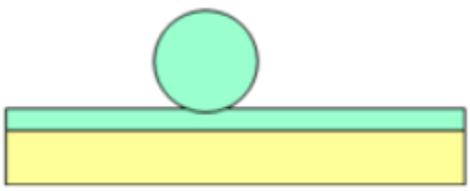

Figure 1.4 ***Schematic drawing of Stranski-Krastanov growth mode.***

SK mode is interesting because it involves a change in the balance of forces during the initial deposition. For example, while the initial energy relations may favor layer-by-layer growth, strain effects from lattice mismatch or thermal expansion can shift the growth mode due to increased interfacial energy. This is often found to be the case in polycrystalline films, where substrate and deposited films are different regarding their structural properties.

Interface Energy

Due to the nature of this work, interfacial energy becomes exceedingly important to understand as it plays a major role in dictating the mechanism of growth. One of the advantages of polycrystalline films is their ability to grow on a wider variety of substrates with differing properties. Single crystal films however, are limited to a smaller selection of viable substrates due to the induced strain from their mismatch, causing a reduction in material quality and therefore device performance. To better understand interfacial energies, it is important to distinguish the energy contributions that make up the total interface energy. First, we have the energy due to the atoms in the film on the substrate $\varepsilon_{\lambda,j}(\frac{F}{S})$, where j is the jth atom in the λth film layer. Next, we have the energy due to atoms in the substrate under the film $\varepsilon_{\beta,j}(\frac{S}{F})$, where j is the jth atom in the βth substrate layer. Then we have the energy due to atoms in the pure film layer $\varepsilon_{\lambda,j}(\frac{F}{F};a_s)$, where a_s is the lattice constant of the substrate. Lastly, we have the energy contribution from the atoms in the substrate $\varepsilon_{\beta,j}(\frac{S}{F})$. It is important to note that the energy contributions of two separate surfaces related to the bulk system is expressed as,

$$\sigma = \frac{[E_{two\ surface\ system} - E_{bulk}]}{A} \quad \ldots\ldots\ 1.7$$

Where A is the total combined surface area from each separate surface. The total interface energy given by the contribution of each system described above results in the expression [4],

$$\sigma_I = \{\sum_{\lambda=1}^{N_L^F}\sum_{j}^{N_A}[\varepsilon_{\lambda,j}\left(\frac{F}{S}\right) - \varepsilon_{\lambda,j}(\frac{F}{F};a_s)] + \sum_{\beta=N_L^F+1}^{N_L^F+N_L^S}\sum_{j}^{N_\beta}[\varepsilon_{\beta,j}\left(\frac{S}{F}\right) - \varepsilon_{\beta,j}(\frac{S}{S})]\}/A \quad \ldots 1.8$$

Where N_L^F and N_L^S are the number of layers in the film and substrate respectively, and N_A and N_β are the number of atoms in each of the λth and βth layers respectively. Equation 1.8 gives useful insight into the dynamics of interfacial energies during growth. We can observe that as film thickness increases, the coupling between newly deposited atomic layers and the substrate surface becomes weaker. Eventually, newly deposited layers are simply growing on similar surface material, and $\varepsilon_{\lambda,j}\left(\frac{F}{S}\right) = \varepsilon_{\lambda,j}(\frac{F}{F};a_s)$. The second term also experiences a similar change, where deeper substrate atoms no longer interact with atoms in the newly deposited layer, and $\varepsilon_{\beta,j}\left(\frac{S}{F}\right) = \varepsilon_{\beta,j}(\frac{S}{S})$. Therefore, continued growth of crystalline films will see a drop in interfacial energy as the film thickness increases.

Defects in PbSe

The IV-VI rocksalt family has an emergent property associated with their unique atomic bonding nature, giving rise to a form of "defect tolerance." This tolerance has been a large factor in lead selenide's popularity, as its relatively large static dielectric constant (ϵ_{PbSe} = 210 at RT) results in the screening of defects through lattice distortion in response to charged point defects and can therefore maintain high carrier mobilities even at relatively high doping concentrations [5]. Figure 5 depicts the relationship between carrier mobility and conductivity versus doping concentration in PbTe epitaxial films for different temperatures [6].

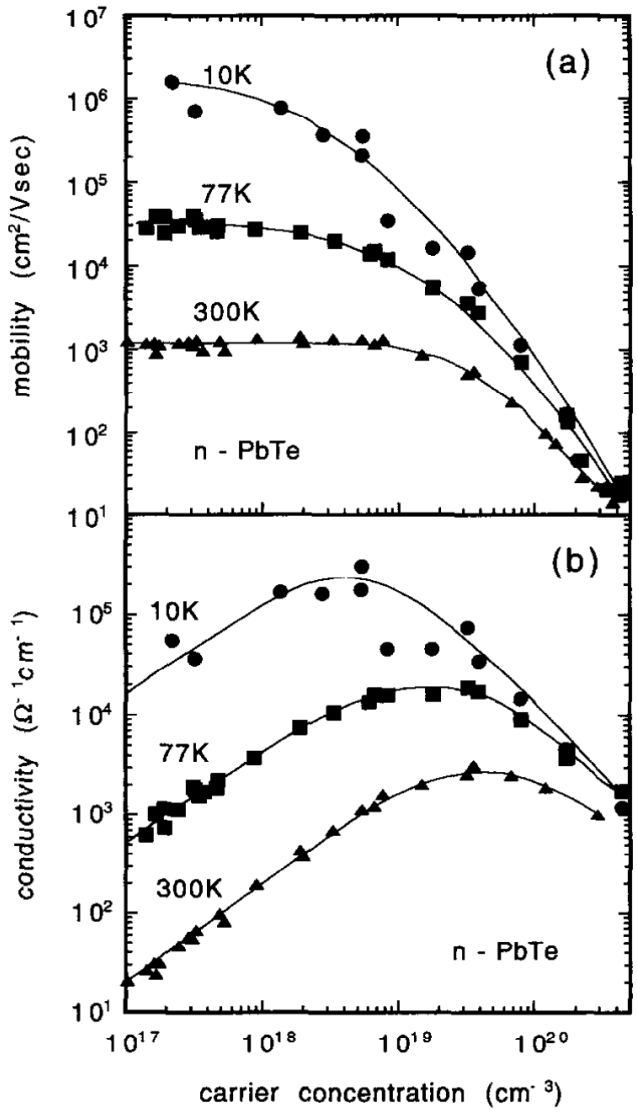

Figure 1.5 ***Hall mobility (a) and conductivity (b) of PbTe films as a function of carrier concentration.*** *[6]*

While the promise of lead selenide's robustness to high defect densities in the lattice are encouraging, challenges remain regarding the growth of epitaxial PbSe films on suitable substrates for low-cost and competitive MWIR optoelectronic device applications. Here, misfit dislocations, growth pits, and anti-phase defects become of particular interest regarding the growth of epitaxial films on foreign substrates.

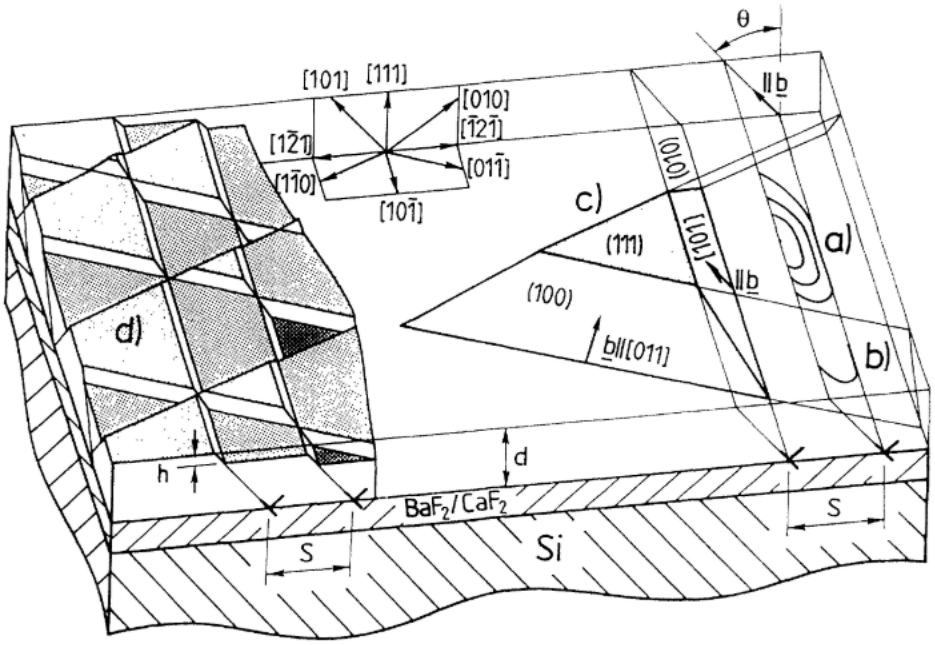

Figure 1.6 ***Defect Slip System for PbSe:*** *The primary slip system for PbSe is along {001} <110>, which results in a negligible Schmid factor for PbSe(001) thin films.*

The IV−VI rocksalt family faces challenges regarding growth orientation due to the nature of their active defect slip planes. IV−VI rock salt structure materials like PbSe have a primary slip system along {001} <110>, resulting in the preferential dislocation gliding along the {001} plane. The result this slip system provides a condition for accumulated dislocations in PbSe films grown in the (100) orientation to feel no resolved shear stress from in-plain strain, locking dislocations in place. The relative amount of shear stress from in-plain strain for different orientations is typically related by their Schimd factor.

$$m = cos\varphi cos\lambda \ldots\ldots\ldots 1.9$$

Where m is the Schmid factor, and φ and λ are the angles between the slip plane and the normal and glide direction angles of the film respectively. The resolved shear stress is then related simply by the following equation,

$$\tau = m\sigma \ldots\ldots\ldots 1.10$$

Where, τ is the resolved shear stress, m is the Schmid factor, and σ is the stress being applied to the material. For PbSe(001) thin films, the {001} <110> active slip plane results in a zero Schmid factor, while PbSe(111) thin films yield a Schmid factor of 0.41. This handicap for PbSe films grown in the (100) orientation is often avoided by simply utilizing (111) orientated substrates. With this knowledge, researchers are able to exploit PbSe's native slip plane, where PbSe(111) films defects can be reduced by encouraging lateral diffusion and eventual annihilation through post-growth treatment process such as temperature-cycling.

Comparison of PbSe, Si, and Ge

Compared with popular substrate materials like silicon and germanium, PbSe is fortunate in that it shares a base cubic crystal structure with these materials. However, this is where their similarities end. Large mismatch in lattice constant and thermal expansion coefficient yields high stresses in deposited films, leading to the formation of cracks and defects. Table 1.1 provides the relevant material parameters of CaF_2, Si, and Ge in reference to PbSe.

Table 1.1 Lattice constant, thermal expansion coefficient, and energy bandgap at 300K.

Material	Lattice Constant (Å)	α at 300K (10^{-6} K^{-1})	Band Gap (eV)
PbSe	6.126	19.4	0.278
CaF_2	5.464	19.1	11.6
Si	5.431	2.6	1.17
Ge	5.658	5.9	0.67

It is quickly noted from the above table that such a high mismatch in lattice constant and thermal expansion coefficient between PbSe and Si would result in low quality epitaxial films, inhibiting high-performance electronic devices. This effect has been experimentally observed early on in the study of PbSe growth. For this reason, buffer layers were sought out which could help mitigate the stresses induced by such a mismatch. Looking at Table 1.1, we observe that CaF_2 is closely lattice matched with Si while sharing a similar thermal expansion coefficient with PbSe. Over the years, epitaxial PbSe films have been deposited on thin CaF_2 buffer layers on silicon substrates with some success. The relaxation of mismatch of this buffer layer has produced PbSe films on Si with much lower defect densities, bringing it down from 10^9 cm^{-2} to high 10^6 cm^{-2}. While CaF_2 buffer layers have shown marked improvement in epitaxial PbSe films on Si, the Shockley-Read-Hall contributions from defect densities in this range are still too high to compete with other state-of-the-art infrared material systems.

III. LEAD SELENIDE GROWTH

History of Lead Selenide Growth

The history of Lead Selenide growth dates back longer than most would expect. Early on in the 20^{th} century, researchers were intrigued by the unique properties of lead-chalcogenides, including PbSe, noting observations of a high photoconductive effect observed in these films. Upon further investigation, the notably high dielectric constant, narrow direct-bandgap, and opto-electronic properties of PbSe pushed researchers to study the film's growth and material characteristics for use in MWIR optoelectronic device applications. Very quickly however, researchers discovered that scalable homoepitaxy of high-quality PbSe films on PbSe substrates

would not be achievable. This is due to the poor stability and mechanical properties of PbSe when compared to more robust material systems such as silicon. Compared to silicon, PbSe is extremely soft. Even picking up a PbSe wafer or film with soft tweezers can damage the PbSe crystal structure, introducing a large number of defects or cracks. In the case of large area PbSe wafers, the wafer itself will break under its own weight when handled. For this reason, researchers have been forced to pursue other potential avenues of high-yield PbSe film growth. For decades, researchers have had to rely on either polycrystalline PbSe film growth on severely mismatched or poly/ amorphous substrates, or try to find ways to overcome the mismatch and high defect generation associated with PbSe heteroepitaxy. Regarding the later, extensive efforts have been made to find solutions for growing high-quality PbSe films on industry scalable substrate materials such as silicon or various III-Vs. The most common solution used in heteroepitaxy of PbSe films on Si substrates is the implementation of a fluoride buffer layer such as CaF_2 or BaF_2. For example, researchers noted that CaF_2 could reduce the strain effects of the mismatch between PbSe and Si by acting as a buffer layer, reducing the 12.1% lattice mismatch between PbSe and Si to <1% for CaF_2 and Si. Further, calcium fluoride's thermal expansion coefficient is much closer to lead selenide, with a mismatch of only 1.5% as observed in Table 1.1.

Recent Progress of PbSe

More recently, efforts have been made to expand the list of suitable substrates for the epitaxial growth of PbSe to include III−V materials such as GaAs, GaSb, and InAs [7]–[9]. While there has been promising success on these substrates, each material system comes with its own design hurdles, such as small critical thickness, high defect densities, and substrate orientation selection due to the nature of lead selenide's defect slip plane.

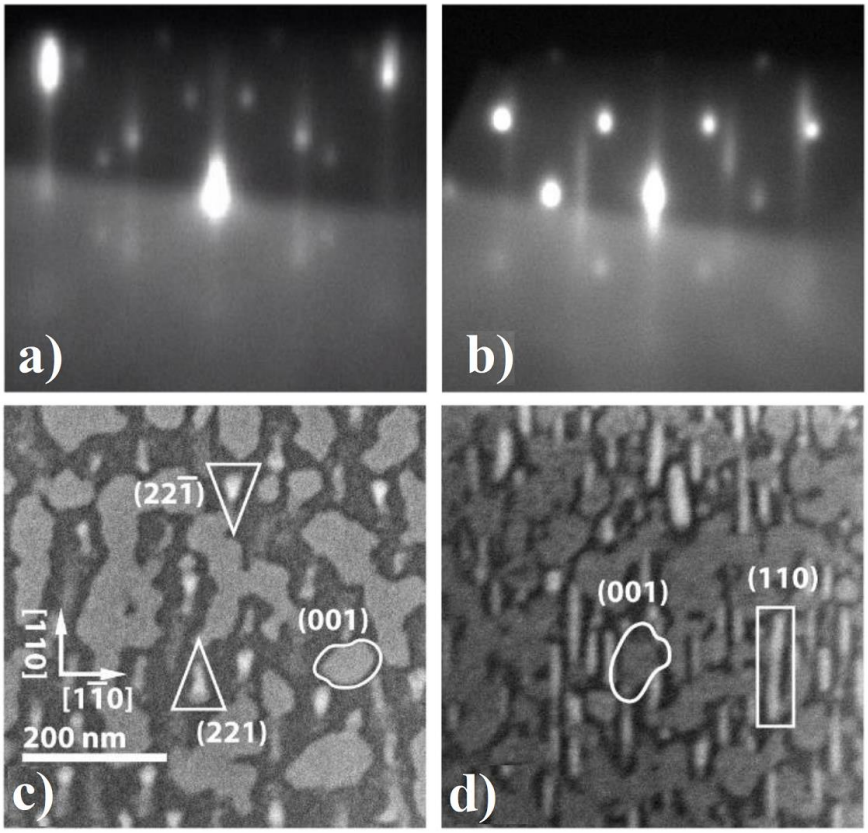

Figure 1.7 ***PbSe nucleation behavior on III-V GaSb substrate:*** *a) RHEED pattern for PbSe nucleation at substrate temperatures >330°C, b) RHEED pattern for PbSe nucleation below 300°C, and c) & d) SEM investigation of mis-oriented nucleated PbSe grains above 330°C and below 300°C respectively.[8]*

Figure 1.7 provides a direct visualization of the challenges PbSe faces when growing epitaxial films directly on foreign substrates. Interfacial stresses impede the formation of highly oriented nuclei, giving rise to varying oriented nucleation of 3D islands. While accumulated deposition beyond the initial nucleation layer may result in a bulk single crystal film, the presence of some these mis-oriented islands at the interface promote potential defect centers, potentially contributing to the introduction of growth pits and anti-phase defects often observed on the surface of epitaxial PbSe films.

Regarding PbSe growth on poly/ amorphous substrates, polycrystalline PbSe films have shown great promise in recent years due to the application of a “photosensitization” process. This process involves a post-growth annealing treatment of PbSe films, typically involving oxygen,

iodine, or some combination of the two. Under certain conditions, researchers have found the background carrier concentration of sensitized films to be drastically reduced, lowering the dark current density of PbSe-based photodetectors by multiple orders of magnitude.

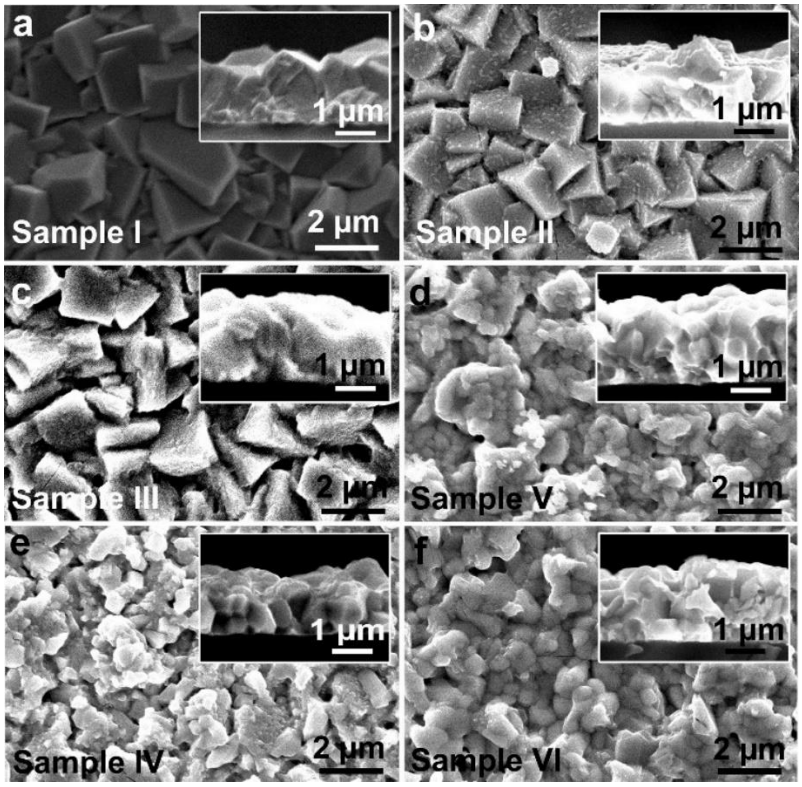

Figure 1.8 ***Top-and side (inset)-view SEM images of:*** *as-grown (a) and sensitized PbSe annealed at 380 °C in (b) pure nitrogen for 30 min, (c) 20-min nitrogen followed by 10-min oxygen, (d) 25-min nitrogen followed by 5-min iodine, (e) pure oxygen for 30 min, and (f) 25-min oxygen followed by 5-min iodine.[10]*

While MWIR photoconductive detectors using this technology have reported astounding room temperature detectivities values, the 1/f noise and pixel performance uniformity is still a major challenge limiting their progression. Figure 1.8 depicts the morphology of polycrystalline PbSe films before and after various post-growth treatment conditions, where only samples V and VI observed strong detector performance. However, both samples display nonuniform film properties with large varying degrees of pixel performance. Due to the inhomogeneous nature of the current PbSe PC detector design, special readout integrated circuits (ROIC) are required to extract the

relative signal intensity from each pixel to form a MWIR imaging camera, where each new detector array requires its own ROIC calibration and relative signal intensity correction to form an accurate image. Efforts to produce consistent pixel performance levels using finely controlled experimental conditions have proven to be extremely challenging, keeping the overall cost and power consumption of the PbSe-based PC detector technology higher than desired.

The missing link in PbSe technology development now is the ability to fabricate a low defect density film with high yield. Various methods for achieving this include designing techniques to passivate or "sensitize" epitaxial PbSe films similar to the methods used in CBD grown poly-PbSe films, or innovative methodologies for growing low defect density epitaxial PbSe thin-films on foreign/ mismatched substrates to begin utilizing lead selenide's true potential for higher operating temperature MWIR photodetector applications. Researchers are still investigating new methods for improving both the polycrystalline and epitaxial PbSe film technologies, with efforts towards more reproducible and stable sensitization conditions for poly-PbSe films, inclusion of oxygen and iodine atoms in PbSe epitaxial films, and enhanced growth methods and control schemes for improving epitaxial film quality on mismatched substrates.

2. Experimental Methods

I. INTRODUCTION

This chapter is dedicated to the numerous experimental equipment and procedures involved in material growth, characterization, and device fabrication. In the following sections, I intend to provide a useful overview regarding the working principles behind the growth, characterization, and fabrication of MWIR PbSe-based optoelectronic devices. Due to the large number of experiments and efforts it takes to develop either a new material, material structure, or device in this work, I will focus more on establishing the core principles relevant to the techniques employed here rather than providing a full breakdown of the complex theory and mathematical equations that fully describe each process. Regarding thin film growth, although other physical vapor deposition techniques are routinely used, the main focus of this body of works will revolve around molecular beam epitaxy. Material characterization, device processing/ fabrication, and device characterization techniques will also be discussed with a focus on visualization for better understanding of working principles, which may also act as an introduction of the processing flow in which optoelectronic devices are fabricated for future students. This chapter is important to me, as early in my research career I was fortunate enough to learn everything from material growth, characterization, processing, and device testing from veteran members in our group who have since moved on to other stages in their career. I hope the information provided here will help give readers a broad understanding of the processes and techniques used in developing thin film materials, structures, and devices, while also finding usefulness for the next generation of students so they can positively impact the research and development efforts here at OU.

II. MOLECULAR BEAM EPITAXY

Introduction to the MBE system

Molecular beam epitaxy is a complex ultra-high vacuum deposition system that provides extreme precision and control of adatom nucleation and bulk growth on various substrate surfaces and film interfaces. In recent years, MBE growth has begun to find its way into practical industry applications, no longer serving as a purely research-oriented growth system. This is due in large part to the advancements made in both our understanding and fabrication of complex material structures and devices, and the design of material properties which cannot be replicated by any other deposition technique.

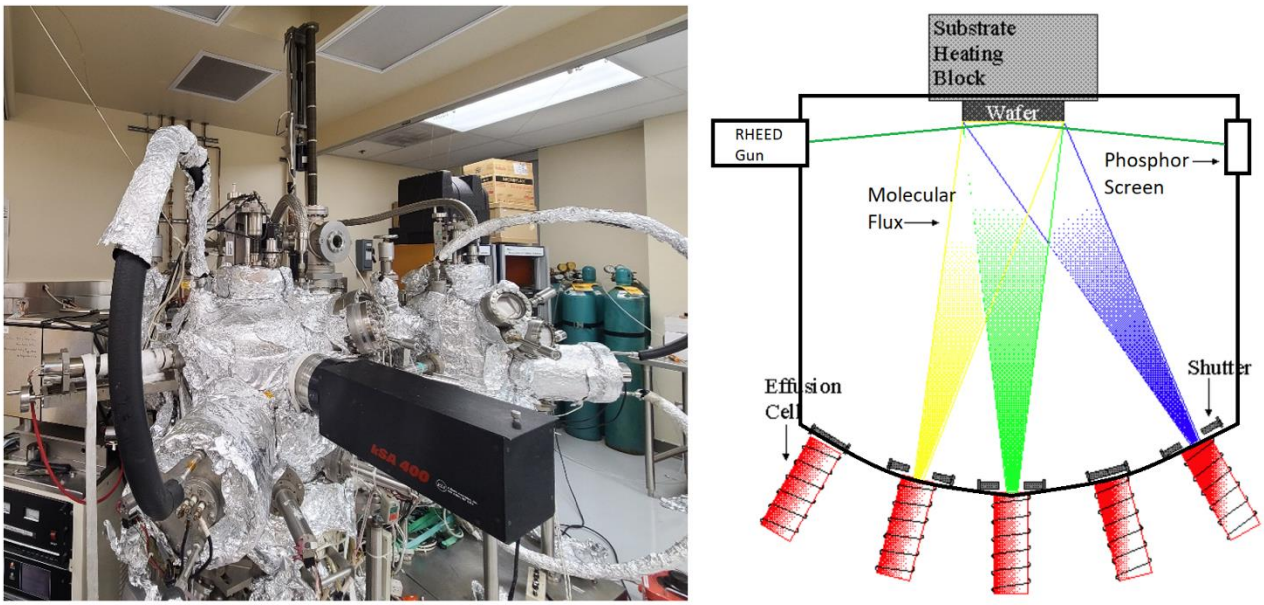

Figure 2.1 ***Custom MBE System for IV-VI deposition.***

When operating complex vacuum systems such as the MBE, it is crucial to understand the various aspects that dictate its proper function. For this reason, the nickname “Most Broken Equipment” has been used for MBE to describe the numerous ways in which something can go wrong. Figure 2.1 showcases the custom MBE system used in our experiments. The large chamber on the left is the main chamber for IV-VI growth and contains 7 effusion cells and one custom oxygen plasma source. The chamber on the right is used for thermal cleaning and deposition of fluoride buffer layers such as calcium fluoride. The two growth chambers are connected via the buffer chamber, with a separate loading chamber located above isolated by a gate valve. This custom MBE system allows for the growth of separate crystalline materials in an ultra-high vacuum environment without concern of cross-contamination or needing to break vacuum at any time. This is exceedingly important when dealing with common IV-VI materials such as PbSe, as elements like Se can easily contaminate neighboring effusion sources, requiring a multiple growth chamber set-up as depicted in Figure 2.1

Molecular Flux

Unlike other epitaxial growth methods such as the various chemical vapor deposition techniques, MBE utilizes a molecular flux generated from its effusion cells in a solid-vapor-solid deposition process without the use of extraneous chemical precursors. While some reactions may be used in MBE before epitaxy begins, such as a selenium cracker when performing co-deposition, the only precursors involved in MBE growth are those that will be directly incorporated into the desired crystalline film. However, this is not to say that the majority of the species will actually be deposited and add to the growth of the film. For instance, it is common practice when growing GaAs to supply a non-stoichiometric ratio of gallium and arsenic flux to achieve high-quality films.

This is due to the large difference in vapor pressure of gallium and arsenic, where the higher volatility of arsenic requires a much higher molecular flux during growth to achieve a GaAs film with the right composition. For growth of III-Vs, the molecular flux ratio of V:III sources can be higher than 5, which in the case of GaAs for example, results in growth rates limited by the molecular flux of gallium adatoms. It is important to note however, that while most of the atomic species may not find its way into the film, every adatom evaporated from the effusion cells has the *potential* to contribute to film growth. Taking this understanding further, the goal of any researcher is then to find how the change of each growth parameter impacts the statistical probability in which these adatoms either scatter, nucleate, interact, or desorb from the growth surface.

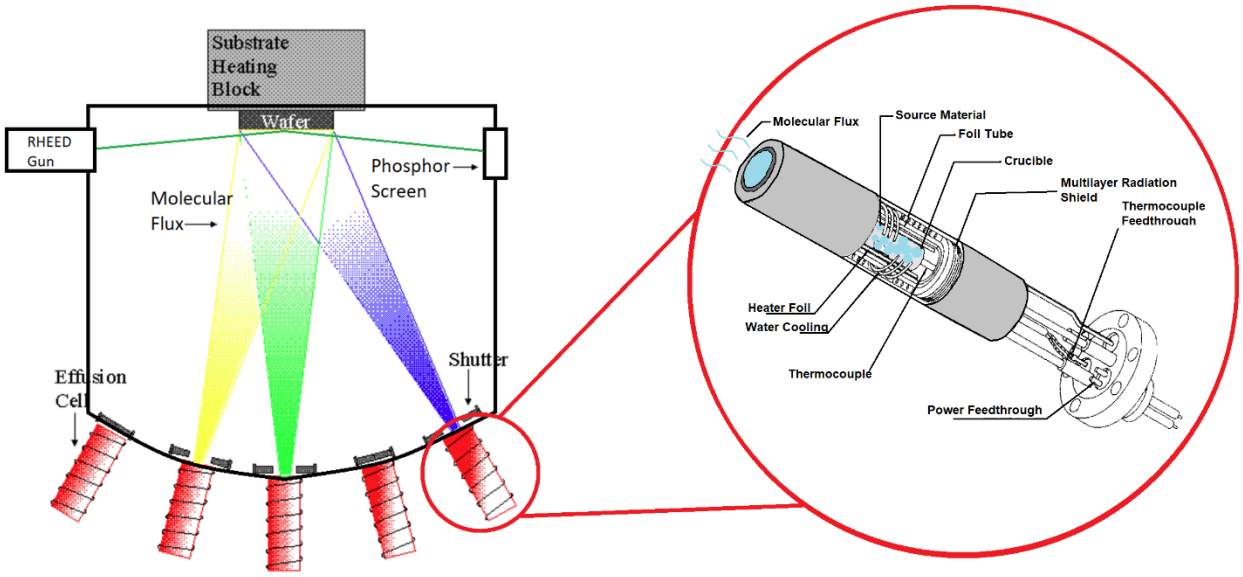

Figure 2.2 ***MBE Effusion Cell:*** *Schematic for a standard MBE effusion cell with the source material housed in the crucible, surrounded by the heater foil and radiation shield. Water cooling is utilized for high temperature effusion to discourage thermal transfer to neighboring effusion cells.*

As pictured in Figure 2.2, the solid source material sits inside the crucible, which is surrounded by a heating element to generate the molecular flux. While the mechanism behind the generation of molecular flux is relatively simple, this process remains the first stage of control researchers have for controlling growth behavior. In generating molecular flux, understanding the resulting

molecular species is important for controlling growth characteristics. For example, compound materials such as PbSe can be deposited by either using a single compound PbSe source material, or by co-evaporating Pb and Se with independent effusion cells. For the case of compound PbSe source material, the compositional makeup of the molecular flux may not be entirely consistent throughout the beam flux. For instance, when heating the crucible, compound PbSe can be evaporated, or can be decomposed into elemental Pb and Se components, or even compound molecules such as Se_2, $PbSe_2$, Pb_2Se_2, and Pb_2Se_3. Further, the higher rate of evaporation of Se causes the compound PbSe source material composition to trend towards a more Pb-rich composition after every growth. Regarding the former, the majority of the molecular flux is dominated by the Pb_1Se_1 species, however, the presence of these other contributions shouldn't be ignored, as they can directly impact the material quality of the deposited film. This effect has been directly observed in compound PbSe MBE growth, where a Pb-rich PbSe source produces Pb droplets or bunches imbedded in the bulk PbSe film, negatively impacting its electrical properties. Further, the insufficient presence of Se results in a high number of vacancy defects in the PbSe films, further impacting the material quality. For this reason, MBE grown PbSe films in this work will be deposited using a co-evaporation of compound PbSe and Se sources to balance the stoichiometry and avoid these occurrences.

Achieving Ultra-High Vacuum

In order to achieve ultra-high vacuum conditions, our system utilizes a three-stage pumping system. The first stage of our pumping process utilizes an Edwards XDS 35i dry scroll pump, which pumps the system from atmosphere down to 10^{-3} Torr. Once a high enough vacuum is achieved, the second stage of our pumping process begins using a Shimadzu Mag-Lev

Turbomolecular pump to achieve a vacuum level around 10^{-7} Torr while backed by the Edwards XDS. Finally, a Gamma Vacuum Titan Ion Pump is used to achieve ultra-high vacuum pressures of 10^{-11} Torr. When pumping the entire chamber from atmosphere, it is necessary to heat the walls of the chamber to encourage desorption of water and other organic and inorganic contaminants found in air. The chamber is heated by wrapping the system with heating belts, while tin foil is used to uniformly transfer heat across the system as to not invoke stress on fragile areas due to thermal expansion. This process can be observed in Figure 2.1, where the system is currently encased with tin foil after having performed maintenance on one of the substrate heaters and refilling of source materials. During this time, the MBE system is at its most vulnerable, with numerous ways in which the system may be susceptible to leaks. For this reason, an EXtorr mass spectrometer inside the MBE is connected to a computer equipped with Vacuum Plus software to monitor levels of relevant elements and compounds such as H_2O, O_2, and N_2.

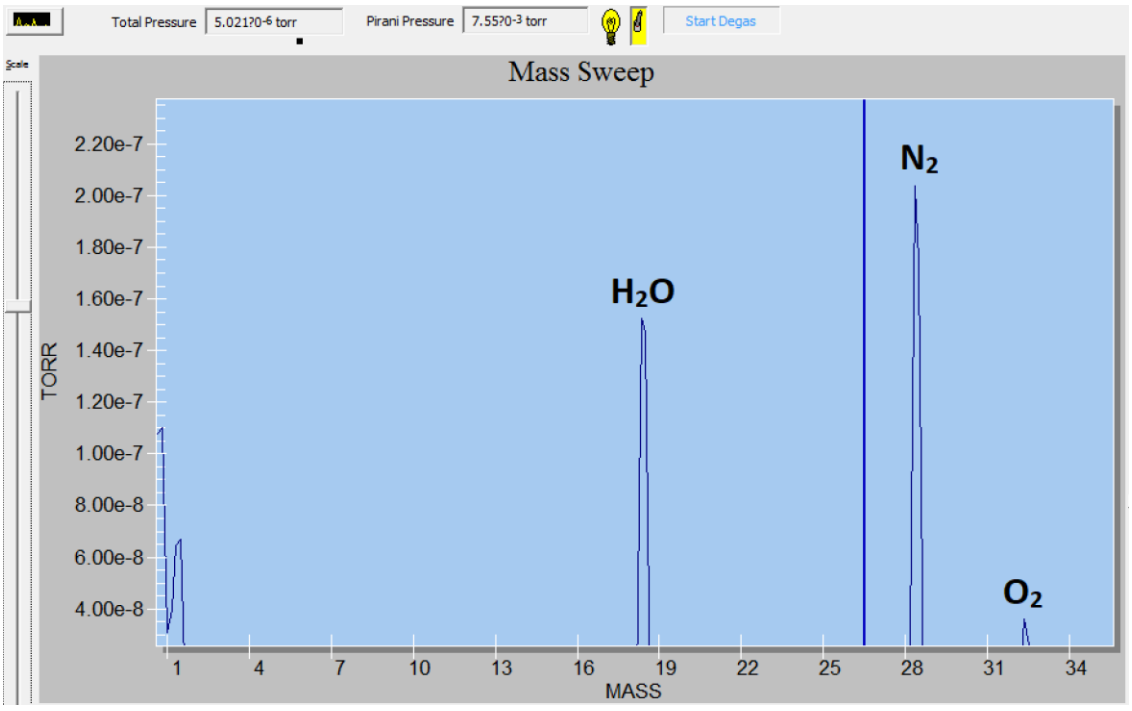

Figure 2.3 ***Mass spectrum analysis using the Vacuum Plus monitoring software in conjunction with the EXtorr mass spectrometer:*** *Mass sweep indicating partial pressure contributions from H_2O, N_2, and O_2.*

The mass spectrometer, combined with constant vacuum monitoring, provides a clear view of the MBE vacuum environment. When a large leak is present, obvious barriers are observed in vacuum level and can usually be discovered and easily corrected. However, smaller leaks below 10^{-8} Torr can be more difficult to diagnose without directly monitoring the relative mass ratio of contributing compounds inside the MBE chamber. For example, the ratio of N_2 to O_2 in air is around 4:1, but the pumping rate of O_2 and N_2 has a non-linear relationship. This allows for easy leak detection via mass spectrometer analysis. Further, isolation of chambers can help identify leak sources, with the help of noble gasses not commonly found in the system such as He. Purposely introducing the outside of the MBE to helium can be a useful technique, where the mass spectrometer detects helium inside the chamber as it leaks in from the outside.

MBE influence on growth dynamics

Epitaxial growth by MBE is a process in which adatoms evaporated from the effusion cells organize into a crystal structure influenced by the crystalline interface or substrate in which they are deposited on. The behavior of adatoms is dictated by thermodynamics, in which the MBE system, adatom, and interface all contribute to the resulting bulk crystal formation. For heteroepitaxy, in which the substrate and film contain different elemental composition, changes in adatom dynamics and resulting crystal growth are extremely sensitive to MBE growth parameters. This is due to the relatively small thermodynamic window in which certain atoms can interact favorably with another to allow for uninterrupted crystal formation.

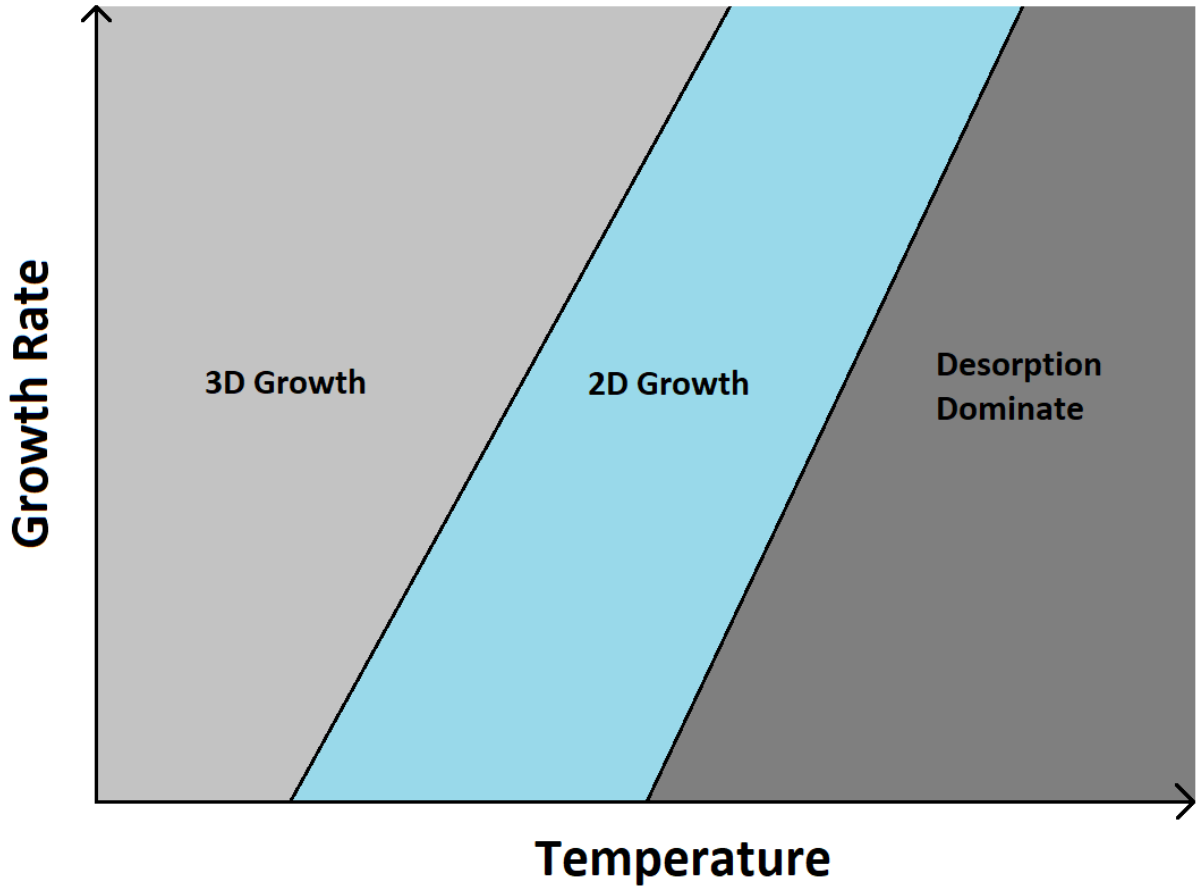

Figure 2.4 ***Impact of growth rate and temperature on adatom formation:*** *At higher growth rates, more thermal energy is needed to encourage adatom diffusion to achieve 2D growth over 3D island formation. Beyond a critical temperature, thermal energy exceeds the desorption condition of the adatom species resulting in poor quality films.*

Molecular flux, partial pressures, and substrate temperature all contribute to the total thermodynamic and kinetic processes in which adatoms either drift, interact, bond, or desorb on the growth surface. Finding the right conditions for optimized epitaxial growth is different for every combination of film and substrate. While physical models exist to help guide researchers, extensive experimental effort is needed to realize high-quality heteroepitaxial growth. Understanding the kinetics and behavior of the growth process combined with in-depth material characterization methods are key to pushing state-of-the-art epitaxial growth and related structures. For this reason, the statistical and thermodynamic interactions of adatoms and surface-film properties were reviewed in chapter 1 in hopes of aiding the reader in understanding how one

might control epitaxial film growth after learning the ways in which the MBE system can influence the growth environment.

Reflection high energy electron diffraction (RHEED)

One of the best tools at our disposal for optimizing and controlling high-quality epitaxial growth is the in-situ observation of reflection high-energy electron diffraction (RHEED) patterns produced by the growth surface in MBE. For our experiments, a 14 kV electron beam is directed at the growth surface at a glancing angle <10°. The diffracted pattern resulting from the growth surface is then observed as it impinges on a phosphor screen, where characteristics of the RHEED pattern and its evolution in time provide intimate detail of the crystal growth.

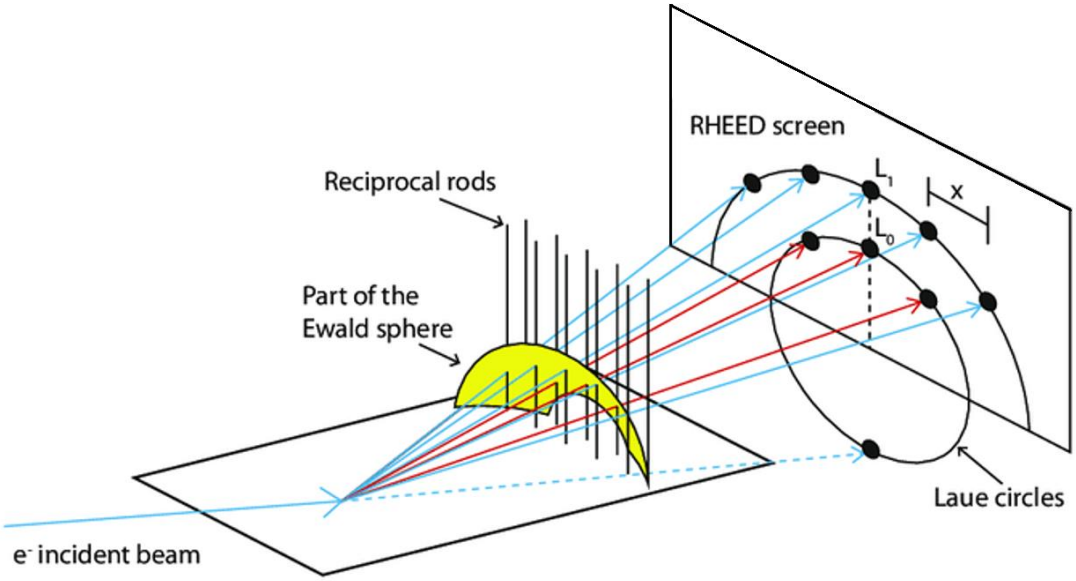

Figure 2.5 ***RHEED image formation:*** *schematic diagram of incident electron beam, beam-sample interaction, cross-section of reciprocal rods and Ewald's sphere, and diffraction pattern on phosphor observation screen.*

When the incident beam impinges on the growth surface, diffraction occurs, wherein an image can be observed and is described by the intersection of the reciprocal rods of the reciprocal lattice planes and the Ewald sphere as depicted in Figure 2.5. The Ewald sphere represents the image

condition, or the allowed diffraction conditions in which reciprocal rods that both intersect with it and satisfy Bragg's condition strongly diffract and can be observed. The magnitude of the Ewald sphere for a given RHEED set up is given by $1/\lambda$. The significance of this, is that the resulting RHEED pattern observed on the phosphor screen directly describes the surface conditions regarding surface atoms and adatom arrangement, revealing the presence of surface reconstruction, lattice distortion, orientation, and surface roughness. Monitoring the evolution of RHEED patterns during growth and comparing their characteristics across varying growth conditions allows for a direct feedback loop in which optimization of the crystal growth can be obtained.

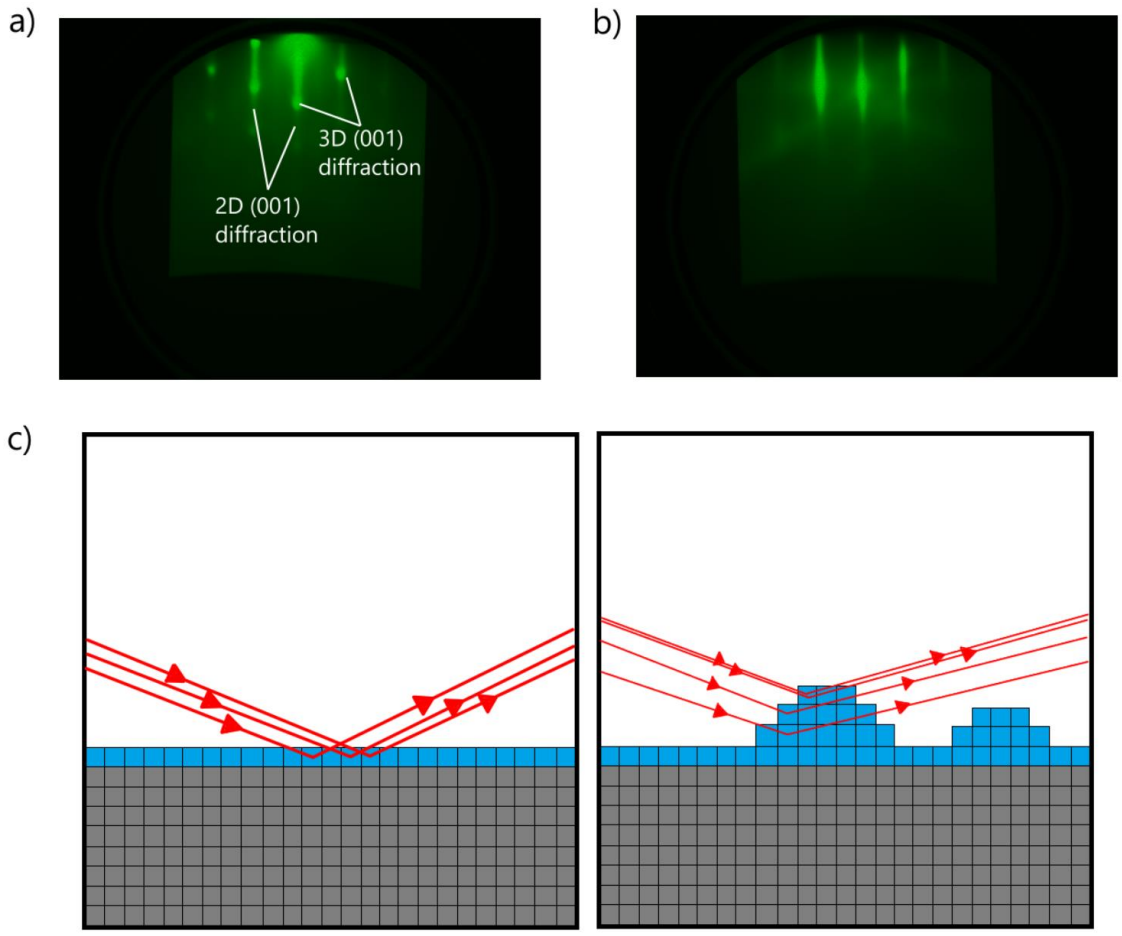

Figure 2.6 ***RHEED pattern interpretation from crystal surface:*** *a) Real RHEED pattern from PbSe nucleation surface, b) real RHEED pattern for bulk PbSe film growth, c) RHEED diagram of atomically smooth surface, and d) RHEED diagram of 3D island growth dominated surface.*

From the example RHEED images in Figure 2.6, the difference in the constructed image from the diffraction on the growth surface shows a stark contrast between Frank-Van der Merwe and Vollmer-Weber growth mode. Further, the transition point from 3D to 2D growth suggest a change in the balance of energies resulting in a Stranski-Krastanov growth mode. This means that initially, the nucleation of PbSe adatoms on the substrate surface were dominated by high Pb and Se binding energies, resulting in low surface diffusion on the substrate. As the growth continued, overgrowth of PbSe formed a new growth surface in which the surface energy begins to dominate, allowing for enhanced surface diffusion transitioning into 2D layer-by-layer growth.

III. MICROSCOPY

Introduction to Microscopy

Microscopy techniques such as electron microscopy and scanning probe microscopy are essential characterization tools allowing scientists to directly observe and analyze a film's morphology and characteristics. The value of these techniques extends into a wide range of qualitative and quantitative information gathering regarding film thickness, surface roughness, grain structure and orientation, interface characteristics, defect structure, and elemental composition. For electron microscopy, the ability to resolve high resolution images of the sample is owed to the nature of the emitted electron's waveform, which for even 10kV emission, can reach much smaller wavelengths than even ultraviolet optical microscopes. However, due to the inherent charge of an electron, coulombic effects need to be considered when imaging a sample. Besides the need for a more complex lensing column, utilizing magnetic lenses rather than optical lenses to shape the electron beam, consideration of the resolved surface is necessary to avoid charging

effects and coulombic repulsion of the incident electron beam. Further, electron microscopy must be performed in a high-vacuum environment in order to avoid charging effects between the environment and sample, resulting in an attractive force between unwanted impurities such as dust particles and the sample surface. All things considered, electron microscopy has shown itself to be an extremely powerful tool when utilized in the right conditions, producing direct visual images of a crystal's surface and bulk morphology down to even sub-nanometer scale.

In contrast, scanning probe microscopy techniques, such as atomic force microscopy, utilize a very different methodology for resolving a sample's surface features. Here, force measurements are taken by directly observing the force interactions between a physical probe and a sample's surface. By directly measuring the changes in the probe tip as it interacts with different areas of the sample's surface, a three-dimensional topographical map can be produced, providing a quantitative image of a sample's surface morphology, along with other information such as a sample's mechanical properties, and even spatially resolved electronic behavior. To achieve this, AFM measurements are performed in different modes of operation, depending on the desired quantitative features scientists wish to observe. In effect, AFM measurements are not beholden to the same restrictions as optical and electron microscopy techniques, which are both subject to aberration and diffraction of the photon/ electron's waveform, along with the need for vacuum conditions to provide a clear path for the incident beam in the case of electron microscopy.

Scanning Electron Microscopy

Scanning electron microscopy (SEM) is the most commonly used electron imaging technique, utilizing a high-energy focused electron beam to excite the sample surface as it scans over a defined area. This technique is regularly used to observe both surface and cross-sectional features, providing a visual image of the topography and morphological features of a sample, along

with orientation, defect identification, and even chemical composition. The image formed by SEM observations is the result of elastic and inelastic electron-sample interactions.

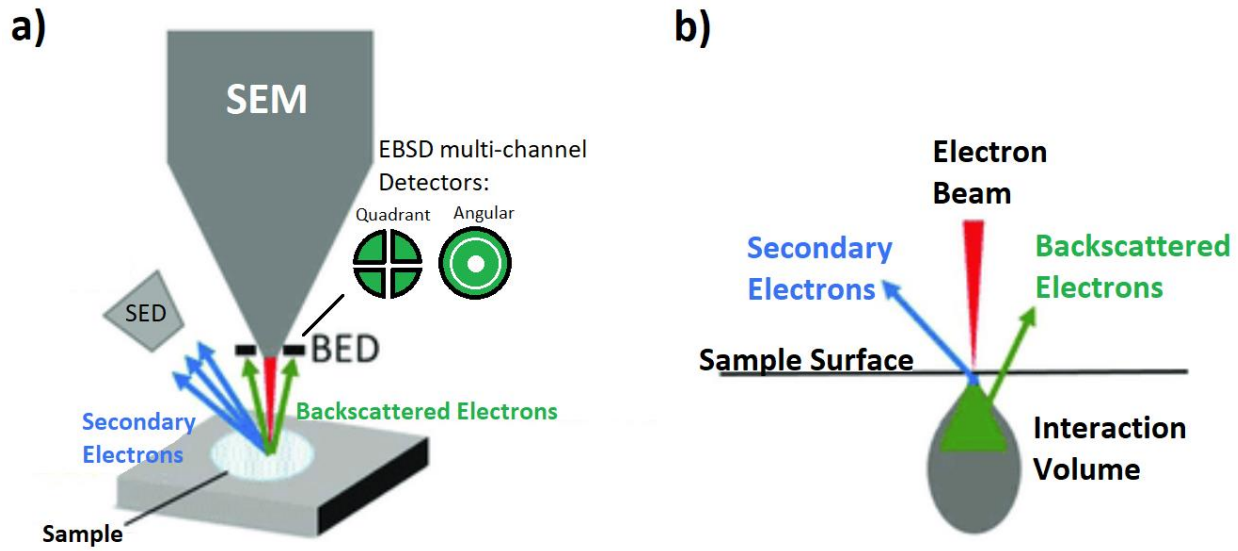

Figure 2.7 ***Schematic of scanning electron microscopy:*** *a) electron emission and detector geometries of secondary and backscattered electrons, and b) electron-sample interaction volume.*

For inelastic interactions, some of the energy from the high kinetic energy incident electrons are transferred to the sample, resulting in the emission of secondary electrons. These secondary electrons are ejected from the sample with much lower energies than the incident electrons, usually on the order of 30-70eV. A detector is then used close to the sample surface with a positively charged collector to attract these secondary electrons. The number of secondary electrons collected by this detector as the incident beam scans across the sample surface provides a direct relationship of "contrast" or "reflection" of the interaction site relative to the preceding and subsequent exposed areas. Over a defined area, the raster and collection of the incident electron beam and secondary electron emission respectively, builds an image for the observer on a scale much smaller than can be achieved by optical microscopy methods. Further, the time between electron-sample interaction

and secondary electron emission occurs on the order of only a few femtoseconds, while the dwell time at each site typically ranges from only a few nanoseconds to tens of microseconds. This means that these time-resolved SEM images can be produced relatively quickly, while maintaining extremely high resolutions. Besides secondary electrons, there also exist “reflection” or “backscattered” electrons, which are the result of elastic electron-sample interactions rather than inelastic. As a result, these backscattered electrons contain higher energies than secondary electrons, and the resulting images are less susceptible to charging effects on the imaged surface. Due to their high energies, backscattered electrons are not easily collected using the same Everhart–Thornley detectors for secondary electrons. Instead, a solid-state detector, often photovoltaic detectors, are placed in the emission path of these backscattered electrons to be collected directly. Further, the rate of emission for backscattered electrons is heavily influenced by the composition or atomic species of the sample for atomic numbers lower than 40. For this reason, backscattered electron images are great for producing high compositional contrast images, where areas of the sample with atoms of higher atomic number produce higher contrast. Secondary electron imaging is instead more commonly used for topological and morphological investigations. However, another distinction between these elastic and inelastic interactions is that the elastic interactions resulting in backscattered electron emission occurs at a much deeper penetration depth compared to inelastic secondary electrons, where secondary electrons are produced at a depth of only 5-10nm, and backscattered electrons are produced as deep as a few microns, as observed in Figure 2.7 (b). This results in a much longer path for backscattered electrons to travel inside the sample before emission, and results in a large number of scattering events reducing the resolution of the overall image. For similar beam energies, this often results in a resolution reduction of up to an order of magnitude compared with the secondary electron images. However, researchers have

found that by simply lowering the energy of the incident electron beam, down to even 1kV, backscattered images can still be observed, while also reducing the interaction volume inside the sample, resulting in higher resolution images comparable to secondary electron images.

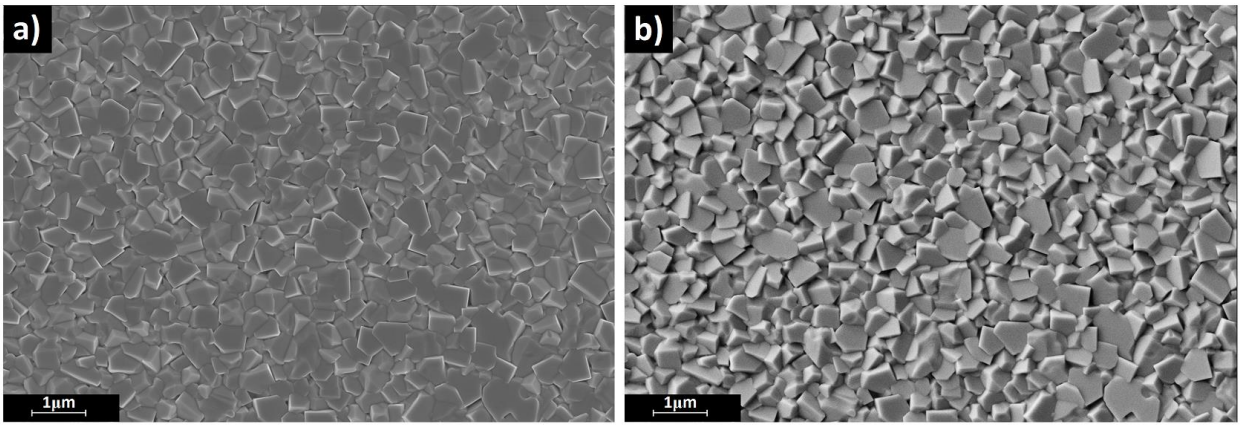

Figure 2.8 ***SEM image comparison:*** *a) polycrystalline PbSe film observed by secondary electrons, and b) by backscattered electrons.*

Another interesting result of these elastic interactions is that backscattered electrons collected by a detector with multiple segments can produce "stereoscopic" images relative to the sample tilt and topology versus detector position, resulting in shadows observed on the imaged area. This technique provides uniquely distinct images when compared to secondary electron images, which do not have the ability to form these stereoscopic shadow-cast features. This effect can be observed in Figure 2.8, where polycrystalline PbSe films that I deposited on SiO_2 substrates show varying number of misoriented grains composing the entirety of the film's surface. While Figure 2.8a provides a clear view of the grain boundaries, the stereoscopic view from the backscattered electrons in Figure 2.8b provides a much clearer view of the facets and grain orientation. The application of the backscattered electron detector here allows for easy identification of differing oriented grains, with easily observable contributions in Figure 2.8b from (001), (110), and (111) poly-PbSe grains.

Atomic Force Microscopy

Atomic force microscopy is a technique that falls under the family of scanning probe microscopy and is often used to provide detailed quantitative information regarding a crystal film's surface morphology along with electronic and mechanical properties. While still employing a raster or scanning of the sample's surface similar to SEM, AFM uses a physical cantilever placed either in direct contact (c-AFM) or <10nm from the sample surface (nc-AFM).

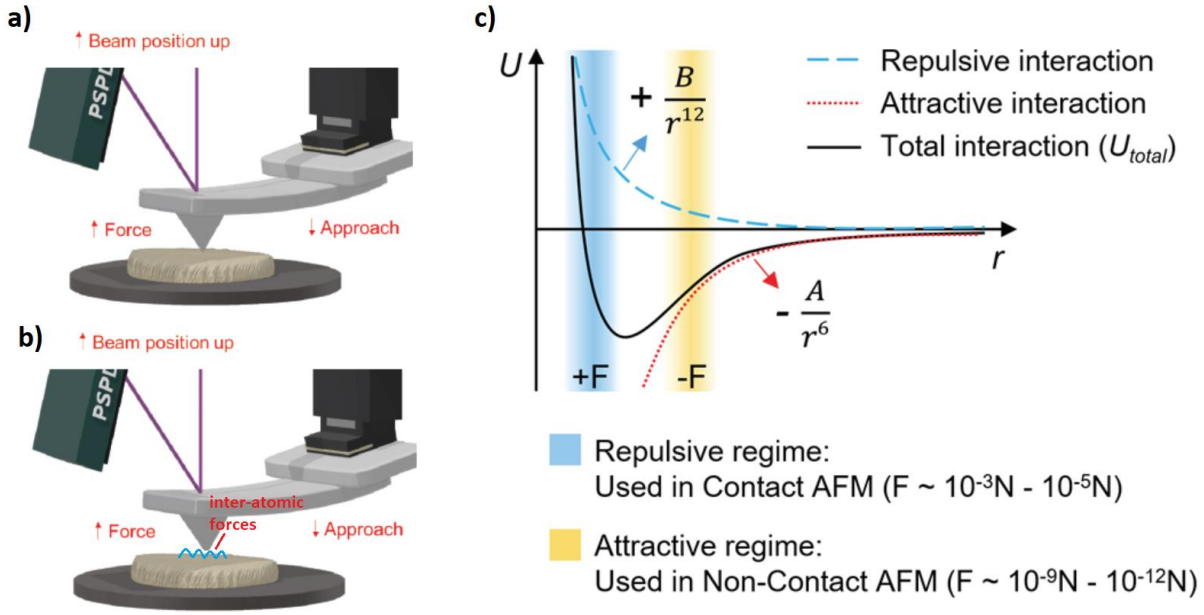

Figure 2.9 ***AFM Operating Modes:*** *a) contact mode AFM, b) non-contact mode AFM, and c) inter-atomic force regimes respective to sample-cantilever separation distance. [11]*

When operating in contact mode, the force between the sample and cantilever are held constant as it sweeps across a specified area. Where the sample may have peaks or valleys, the cantilever adjusts the height to maintain contact with the surface while maintaining a constant sample-cantilever force. By doing this, c-AFM measurements can obtain high resolution images of the

sample surface with quantitative information regarding a sample's surface roughness and morphology. When operating in nc-AFM mode, the cantilever is instead brought to just above the sample surface, ranging from only a couple angstroms to a few nanometers. In doing so, the cantilever tip is subject to attractive forces brought on by inter-atomic force interactions as visually represented in Figure 2.9. By utilizing a piezoelectric modulator to modulate the cantilever at its resonant frequency, usually somewhere between 100-300 kHz, a feedback loop is formed where a detector measures the dampening of the cantilever frequency due to inter-atomic forces from the sample's surface, and the cantilever is adjusted to maintain its frequency. This process produces extremely high-resolution height profiles of the sample's surface. In this work, AFM measurements will be taken in non-contact mode to ensure no deformation of the film surface is caused by the force between the cantilever tip on the film's surface when raster scanning over the imaged area.

IV. Etch Pit Density

Introduction to Etch Pit Density

For epitaxial crystal films, one of the most important pieces of information for researchers to uncover is the defect density of their material. Although there a many different ways to investigate a film's relative material quality, direct measurement of the defect density provides a quantitative marker in which to compare film quality between multiple samples and link their properties to both changes in growth parameters and device performance. Revealing of etch pits is one of the most common techniques employed for this reason. Here, epitaxial films are dipped into an etching solution to etch away the top layers of the film. However, the etch rate of defects versus

the bulk are dissimilar to each other, where defects are typically etched at a higher rate than the bulk. This allows researchers to expose these defects after finding the right etching solution recipe for their given material system. Once exposed, researchers can use either optical or electron microscopy to observe their film's surface and count the number of revealed etch pits or defects in a given area.

PbSe Etch Pit Reveal

Due to the lack of a lattice and thermal expansion coefficient matched substrates in which to grow high yield high-quality PbSe epitaxial films, etch pit density investigations have played an integral role in the feedback loop for researchers to uncover how changes in growth conditions may improve PbSe film quality.

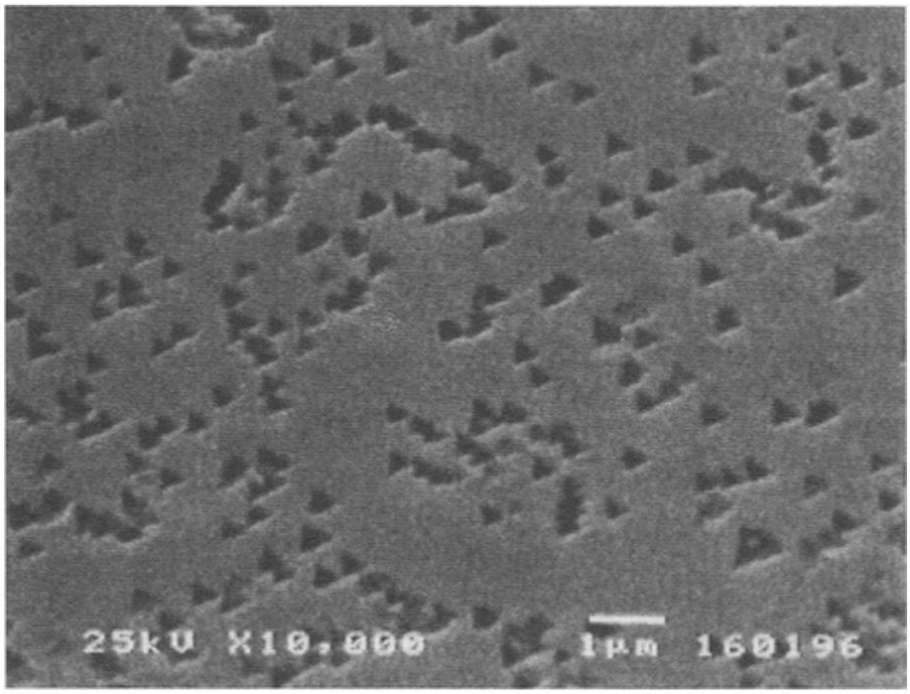

Figure 2.10 ***PbSe etch pit density reveal:*** *PbSe epitaxial film on Si substrate etched using an alkaline solution to expose dislocations via preferential etching of dislocation facets. [12]*

For researchers to expose dislocations in a film, they must first determine an etching solution which displays high preferential etching in their given material system. This is achieved by utilizing certain etchants that have large variations in their etching rate when encountering areas of a crystal with differing amounts of strain. For defects, such as dislocations, the facets surrounding them contain higher amount of strain, and their bonds are more easily broken, resulting in higher etching rates of these areas versus the bulk. Therefore, etch pits often have sharp geometric qualities when observed under microscopy resulting from their orientation and symmetry. For PbSe films grown on Si(111) substrates, these etch pits look like indented pyramids or triangles in the films surface resulting from the three-fold symmetry, as observed in Figure 2.10. Directly observing these etch pits allows for researchers to easily calculate their density. For example, in Figure 2.10, counting the number of observed etch pits over the imaged area gives an etch pit density of 5×10^{8} cm^{-2}. It is important to note that these etch pits are surface features of the film, and while they provide an excellent indication of a film's quality, their distribution may not be homogeneous with film thickness. This has been reported in films who's x-ray diffraction (XRD) full-width half maximum (FWHM) values change with incident angle, suggesting non-uniform scattering of defects with x-ray penetration depths. These tools in combination then provide a more accurate indication of overall film quality when used in conjunction.

V. X-Ray Diffraction

Introduction

X-ray diffraction is one of the most used tools in a researcher's arsenal. This is largely due to the minimal preparation needed for samples to be measured, and the wide variety of useful

information gained about a film's crystalline nature. Observing XRD of crystalline films provides a host of information including lattice parameter, orientation, crystallinity, stress/ strain, defect density, composition, and vicinal tilt. The main working principle of XRD measurements is the x-ray source, sample, and detector set-up. Formation of the incident beam is typically achieved by directing a high-power electron beam at a copper target, where the x-rays emitted are directed through a monochromator designed for a specific wavelength. The most commonly used wavelength for these measurements is the characteristic $Cu_{k\alpha}$ 1.54Å wavelength. This standard is for convenience of researchers so that diffraction peaks between experiments can be directly compared. The resulting x-ray beam is then directed to the sample's surface at differing angles depending on the film's crystallinity.

The mechanism of interest in XRD measurements results from the x-ray-sample interactions. In a crystalline film, the periodic arrangement of atoms in the lattice structure act as planes of reflection or potential mirrors when satisfying a condition known as Bragg's Law. In XRD measurements, as many variables are held constant as possible, leaving the x-ray beam, sample, and detector angle to be the main variable in which researchers control to find the condition in which Bragg's Law is met. For crystalline films with a large variety of planes, such as polycrystalline films, this results in a larger number of angles in which Bragg's Law is satisfied, resulting in a higher number of observed diffraction peaks at various angles. Analyzing these diffraction peaks based on their amplitude, symmetry, and angle, give direct insight into numerous different properties of the observed film.

Bragg's Law

As previously stated, Bragg's Law is the foundation in which XRD measurements are based upon. This condition determines the exact angle in which x-ray diffraction peaks will be observed for a given geometry of arranged atoms. For a given wavelength of x-ray photons directed at a plane of periodically arranged atoms, the angle in which these photons will be reflected can be accurately determined by the following equation,

$$2d \cdot sin(\theta) = n\lambda \ldots\ldots\ldots\ldots 2.1$$

Where d is the interplanar spacing, θ is the angle of incidence between the x-ray beam and the crystal planes, and nλ is an integer multiple of the x-ray wavelength (1.54Å). While the statement condition for Bragg's Law is relatively simple, in practice, there are a few more considerations that need to be understood to fully comprehend its utility in XRD measurements.

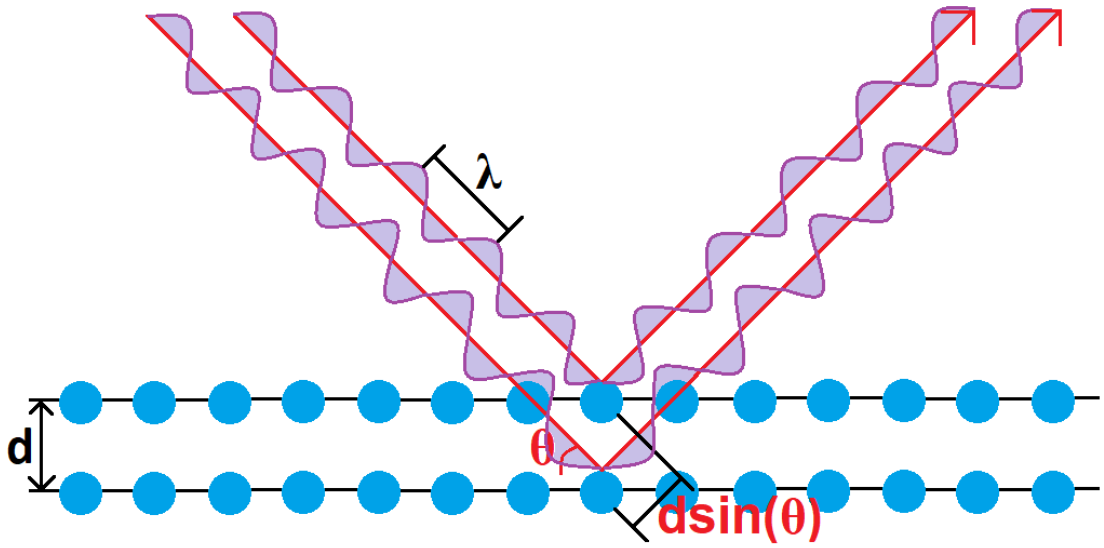

Figure 2.11 ***Bragg's Law for X-ray Photons incident on a crystalline film with interplane spacing of d.*** *Here, the surface atomic plane and second atomic plane of spacing d are shown to reflect the incident x-ray photons. The parallel reflection paths are a result of the parallel configuration of these atomic planes, and the extra path length of the x-ray photons reflecting*

from the second plane relative to the surface is given by 2d·sin(θ). For these reflected beams to interfere constructively, the extra path length must be an integer multiple of the x-ray photon's wavelength (i.e. 2d·sin(θ)=nλ).

As shown in Figure 2.11, bulk crystalline films are comprised of parallel crystalline planes, each of which contribute to reflection of incident x-ray photons. The result of this, is parallel beams of x-ray photons coming from the sample which must interfere constructively to produce high intensity diffraction peaks that can be collected by the scintillator or detector. The condition given by Bragg's Law is that the angle in which this constructive interference will occur for researchers to observe a signal from a material with interplane spacing d, is when the increased optical path length from each subsequent layer is some integer multiple of the x-ray photon wavelength. With this knowledge, one could expect that for a perfect crystal, the angle in which the Bragg condition is met would be infinitesimally small, and no observable diffraction would be observed. However, in real world application, this is impossible to achieve. There will always be some disturbance to this condition, due to the inability to perfectly form a single wavelength x-ray source, variation of the goniometer, variation of the x-ray photon beam spot, detector, and sample size, and imperfections in the crystalline structure of the sample being investigated. This last mechanism involving imperfections of the crystal are of the most importance to researchers. State-of-the-art XRD machines are able to mitigate the other effects, so that the dominating mechanism for broadening of the 2θ diffraction peaks results from imperfections is the crystal structure. Therefore, measurement of a film's XRD FWHM is widely considered to be one of the more useful tools for analyzing a film's material quality.

VI. Photolithography

Introduction to Photolithography

In the fabrication of semiconductor devices, a critical step between initial film growth and final device testing is the processing of the sample into a device structure. To achieve this, researchers employ photolithographic techniques to modify their films into a suitable device structure for precise measurement. These techniques allow for easy formation of pixels or mesas in a film, patterned deposition of insulators, passivators, and conductive contacts, and the ability to form complex patterned etching. The fundamental mechanism in photolithography is the application of a photosensitive polymer called photoresist, which when exposed to light, undergoes a chemical change that either strengthens its adhesion, or makes it easier to remove. By designing a mask to either block or allow light to pass through in a predefined pattern or area, researchers are able to coat their films with this photoresist and produce neatly defined patterns on the surface of their samples. The patterned resist is then typically used in two different ways, either to act as a protective layer patterned etching, or to be used in lift-off, where a subsequent material is deposited on the sample and is lifted off in areas where there is photoresist during the photoresist removal step. While the fundamental principle behind photolithography is relatively simple, researchers have discovered many ingenious ways to use this technique to create extremely effective device structures, from simple but effective device designs to complex state-of-the-art nanostructures.

Photoresist and Mask Design

As previously mentioned, different types of photoresists exist, where exposure to light either strengthens their bonds in the presence of a developer solution, or weakens them, making it easier

to be removed. This reversal in development of photoresist is referred to as either positive or negative photoresist.

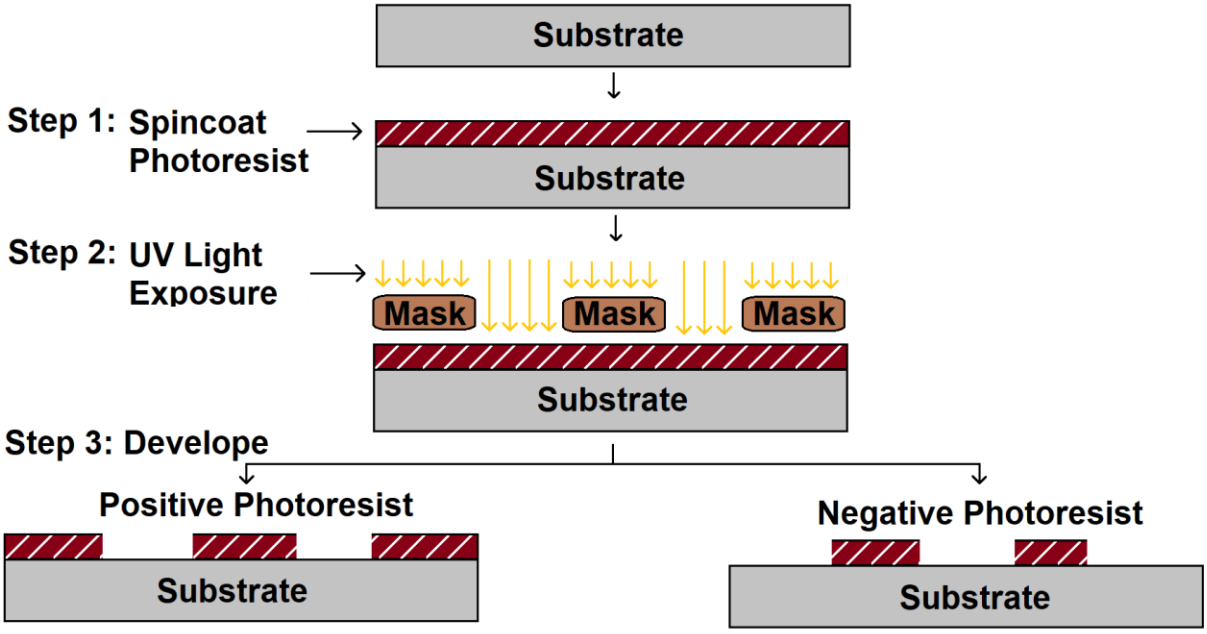

Figure 2.12 ***Process flow for photolithography:*** *After spin coating a layer of either positive or negative photoresist, the sample is selective exposed to UV light through a patterned mask. The sample is then dipped into a developer, where the UV exposed positive photoresist is removed, and the UV exposed negative photoresist remains.*

The immediate difference between these two photoresists is the resulting image produced from a mask as seen in Figure 2.12. For positive resist, the photoresist pattern on the sample will match that of the mask, where open areas of the mask allow for UV exposure of the positive resist, and these areas are removed during the development process. For negative resist, the photoresist pattern will instead be the inverted image of the mask, where the non-exposed areas of the photoresist will instead be removed during the development process. This distinction is important to understand because it is critical to ensure proper mask design when developing a pattern. However, one might ask, "Why not just use positive photoresist all the time for convenience?" The

reason behind this, is the difference in sidewall profile of these two different photolithography methods and their usefulness in different applications.

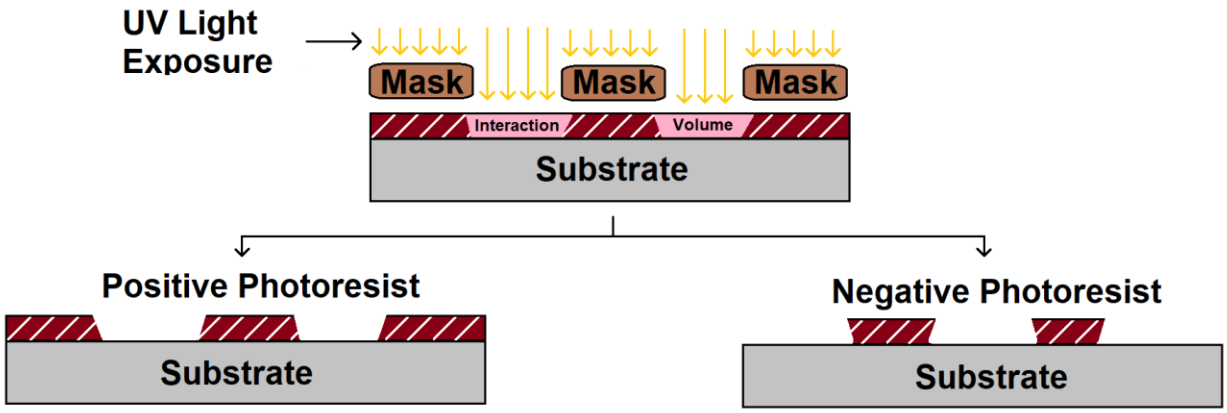

Figure 2.13 ***PR and NR sidewall formation:*** *The interaction volume during exposure of photoresist produces a sloped sidewall, where positive resist forms a wider profile with depth, and negative resist forms a narrower profile with depth.*

The sidewall formation from these two techniques provides unique advantages for different processes. For example, the negative photoresist observed in Figure 2.13 showcases its ability to form a shadow mask over the sample's surface due to the negative sidewall profile. This shadow cast sidewall is uniquely advantageous when depositing subsequent films for lift-off, since areas of the film deposited directly on the sample and those on the photoresist will be completely isolated, making the lift-off process much easier when compared to positive photoresist. If the same lift-off technique were used with positive photoresist, connected areas of the film on the sample and those on the photoresist would prove lift-off extremely difficult. In some cases, the film will act as an encapsulation layer, inhibiting the ability of the photoresist remover from accessing the photoresist. In other cases, the connection between the film on the sample's surface and photoresist will cause lift-off of the film in undesired areas. When designing a mask for a new device structure, every step of the process needs to be meticulously accounted for. Consideration of each process will determine the type of photoresist to be used, resulting in the nature in which the mask must be designed to produce the correct pattern after development. Further, multi-step

lithography processes often require precise alignment between each process to ensure proper device function. It is common for each pattern of the mask to contain alignment markers precisely sized and positioned identically in each step to ensure strict alignment. In this work, all device structures were fabricated using a custom mask design drawn in Layout Editor, and masks were fabricated in a Heidelberg uPG-101 Laser Lithography System.

VII. Radiometric Measurement

Introduction

To characterize the performance of various detector technologies and quantitatively link their performance to changes in growth parameters and device design, it is essential to understand the fundamental principles behind the optical measurement system and set-up. Firstly, as these are MWIR detectors, the first step in measuring their performance is finding a stable MWIR source to illuminate the detectors. Second, understanding of the MWIR source emission behavior and alignment of source and detector are essential to ensure accurate measurement and allow for direct comparison of detector behavior between multiple experiments. For this reason, the Detectivity figure of merit is often used to compare detector performance. Detectivity, also known as D*, compares the noise-equivalent power (NEP) of a detector system normalized to the detector area. By doing this, researchers can directly compare the D* of their detectors with others, no matter the detector size. In effect, the D* measurement eliminates the variable of detector size when comparing different detector technologies, allowing researchers to directly link relative performance levels to the growth environment, material system, processing, and overall device structure.

Radiometric Figures of Merit

As previously stated, the first step in characterizing a detector's behavior is to illuminate the sample with a light source. For this purpose, blackbody radiation sources have proven an effective tool due to their predictive nature and stable emission over time.

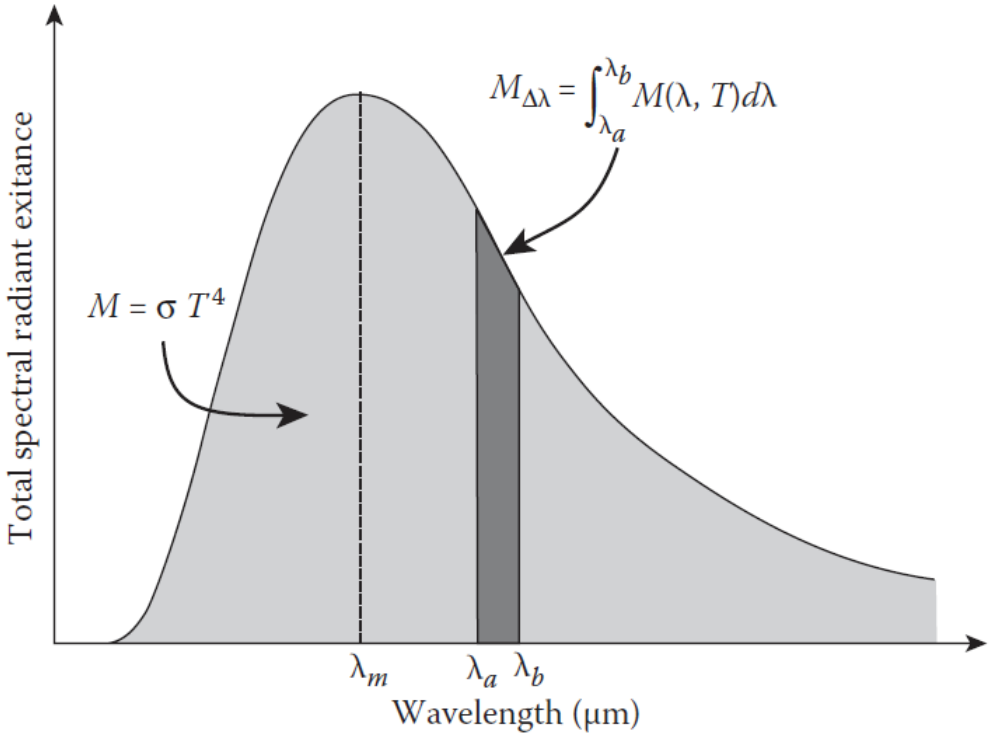

Figure 2.14 ***Blackbody Spectral Radiant Exitance:*** *The total radiant exitance from a blackbody at a given temperature is determined by Planck's Law and can be integrated over a wavelength regime for different applications.*

While all materials exhibit some form of electromagnetic emittance resulting from the vibrational energy of their atoms, a blackbody source is comprised of a material with an emissivity approaching 1. For all other materials with lower emissivity values, the term graybody is commonly used to denote the reduction in their radiant exitance by a constant factor defined by

their lower emissivity value. For research purposes, blackbody sources are used to illuminate detectors at a finely controlled operating temperature, producing well defined radiant exitance over a given wavelength regime for radiometric measurements as shown in Figure 2.14. With a well-defined illumination source and a known detector, researchers can begin to analyze detector behavior.

Responsivity is a fundamental figure of merit which is defined by the relationship between the electrical output signal of an illuminated detector versus the incident radiation power on the detector.

$$R_I(\lambda, f) = \frac{I_s}{\Phi_e(\lambda)\Delta\lambda} \quad \text{.....2.2}$$

Where R_I is the wavelength and frequency dependent responsivity value in A/W, I_s is the signal output of the detector in amperes, $\Phi_e(\lambda)\Delta\lambda$ is the total radiant flux on the detector area for the wavelength regime of interest. Another way to view the responsivity of a detector is through the lens of quantum efficiency. Here, the responsivity actually provides information of the quantum efficiency of the detector and relates it to the incident and output power. Knowing the blackbody emission source, we can easily determine the number of incident photons and collected electrons to calculate the quantum efficiency.

$$R = \eta \frac{q}{hf} \quad \text{.....2.3}$$

Here, η is the quantum efficiency of the detector, q is the charge of an electron, h is Planck's constant, and f is the frequency of the optical signal. Already, researchers can attribute differences in their detector technology to the measured responsivity of their detectors and begin to understand how their growth, processing, or device structure might have impacted their performance. Another

aspect to consider regarding the material system of a detector is the temperature dependent behavior. For example, PbSe is known to have an anomalous positive temperature coefficient, where the band gap decreases with lower temperature rather than increasing like most other material systems[13].

$$E_g(T) = 125 + \sqrt{400 + 0.25T^2} \quad \text{.....2.4}$$

Here, the temperature dependent bandgap of PbSe observes a decrease from 0.27eV at room temperature to 0.24eV at 230K. The significance of this regarding responsivity is that at lower temperatures, lead selenide's MWIR absorption is extended to slightly longer wavelengths, allowing for the collection of more incident photons resulting in more optically generated carriers. While this may not directly change the responsivity of the detector due to the simultaneous increase in both the signal and number of incident photons on the detector, it is still an important distinction. Further, lower operating temperatures often results in an increase in carrier mobility, enhancing the quantum efficiency and subsequent detector responsivity[14], [15]. Once the signal is observed, researchers are then curious about the nature of noise in their detector systems. While on the surface, high responsivity values may indicate stronger detector performance, noise contributions emerging from the detector can limit their potential success. These noise contributions can arise from a multitude of sources.

$$J_{Noise} = J_{Johnson} + J_{Shot} + J_{GR} \quad \text{.....2.5}$$

The dominating noise contributions typically result from Johnson-Nyquist noise (thermal) ($J_{Johnson}$), shot noise (J_{Shot}), and generation-recombination noise (J_{GR}). At temperatures above 200K, Johnson-noise and generation-recombination effects dominate over the shot noise contributions in PbSe detectors [16]. However, I will note that recent studies suggest a unified

mechanism responsible for both shot noise and Johnson-noise in photodetectors, which may help illuminate and reshape the way we characterize our devices[17]. As described earlier, however, lead selenide's anomalous temperature behavior observes a shrinking of the bandgap with lower operating temperatures. While this has a positive effect on the extension of its absorption window to longer wavelengths, this also produces an increase to thermal or Johnson-noise contribution. Researchers investigating PbSe are then interested in optimizing the generation-recombination mechanisms, as contributions from these noise sources typically keep these devices from performing under their Johnson-limited operation.

$$J_{GR} = J_{RA} + J_{Auger} + J_{SRH} \text{.....2.6}$$

Here, the generation-recombination current density is influenced by radiative recombination (J_{RA}), Auger recombination (J_{Auger}), and Shockley-Read-Hall (J_{SRH}). While the contributions from J_{SRH} can be reduced by lowering the defect densities in a material system through enhanced growth techniques or post-growth treatment processes, the radiative and auger recombination effects are often tied to the intrinsic properties of a material itself. Some of these properties can be tailored to reduce these effects, but others are intrinsic properties of the material itself. For example, both the radiative and auger recombination rates are closely tied to a material's bandgap and carrier concentration, with smaller bandgaps and higher carrier concentrations typically resulting in larger radiative and auger recombination rates[18].

$$J_{Auger} \propto R = c_n\left(n^2p - n_i^2n\right) + c_p(np^2 - n_i^2p) \text{ .....2.7}$$

The auger recombination rate R, is determined by a material's electron and hole auger coefficients c_n and c_p respectively, along with the excess carrier concentration. For this reason, researchers are often interested in material systems which exhibit low auger coefficients combined with methods for further reducing the auger rate such as lowering excess carrier

concentrations. The most common method for comparing the signal and noise contributions of a detector is then referred to as the noise equivalent power (NEP).

$$NEP = \frac{V_n}{R_v} = \frac{I_n}{R_i} \text{.....2.8}$$

Here, V_n and I_n are the noise measured in voltage and current respectively, and R_v and R_i are the responsivity values of the detector in voltage and current respectively. NEP is then defined as the signal level needed to produce a signal-to-noise ratio (SNR) of 1. This is an important figure of merit for researchers, as it defines the responsivity required, and therefore the number of incident photons required to produce a signal from the detector that exceeds the noise level. For this reason, researchers have named to the reciprocal of NEP as the *detectivity* (D) of a detector, as it defines the detection condition of a given detector system. As previously mentioned, since NEP and therefore D are functions of electrical bandwidth and detector area, a normalized D* value can be calculated, allowing for quantitative comparison of similar detector performances with various sized areas.

$$D^* = \frac{\sqrt{\Delta f \cdot A_d}}{NEP} = R\frac{\sqrt{\Delta f \cdot A_d}}{I_n} = \eta\frac{q\sqrt{\Delta f \cdot A_d}}{hf \cdot I_n} \text{.....2.9}$$

Here, the detectivity of the measured detector is described by the detector area A_d, the noise bandwidth Δf, and the NEP of the detector. This normalized detectivity is known as D*, with a unit of measurement commonly referred to as Jones and is given in $cm \cdot Hz^{1/2}/W$.

In this work, all radiometric measurements were performed using an Infrared Systems Development standard blackbody emission source operating above 500K in conjunction with a vacuum sealed detector dewar for temperature dependent detector measurements.

3. Growth Study of New Complex Oxide PbO_xSe_{1-x} Thin Films by Oxygen Plasma-Assisted Molecular Beam Epitaxy

I. Introduction

Complex oxides are attributed to an extraordinary wealth of electric, magnetic, optical, and mechanical properties. Applications of such material systems have found benefit in a wide range of technologies relating to energy harvesting, optical sensing, communication devices, nanoelectronics, and more[19]–[22]. Progress in the development of new complex oxide semiconductor material systems have also found great success in the advancement of state of the art technologies such as the growth of perovskite-type complex oxides, Indium Gallium Zinc Oxide (INGZO) material system for flexible thin-film transistors, and Bismuth Vanadate ($BiVO_4$) as a complex metal oxide photoelectrode[19], [23], [24]. To better understand the role oxygen atoms play in the formation and properties of complex oxides, it is imperative to develop controlled methods for fabrication and characterization of such materials. For instance, Lead Chalcogenides, especially Lead Selenide (PbSe), have for a long time been a focus of interest for scientists due to having a narrow optical bandgap perfectly suited for the development of optical sensors and emitters in the mid-infrared (IR) region. However, PbSe films used in such optoelectronic devices often acquire their photosensitivity from interaction with oxygen and other elements, typically through thermal treatment called the sensitization process[10], [25]. Previous studies also indicate that PbSe interaction with oxygen results in enhanced photoluminescent properties and defect passivation, along with the formation of a $PbSeO_3$ surface layer, as well as other possible PbSe

oxides[26]. However, explanations for the physical mechanisms in which PbSe interacts with oxygen to form this complex oxide semiconductor system and promote photosensitivity and enhanced photoluminescence has not yet been established without some ambiguity[27], [28]. Deeper investigations into the role oxygen atoms play in the sensitization of PbSe films require a more controlled introduction of oxygen atoms, and subsequent characterization of crystal formation and properties related to changes in PbSe-O_2 interaction. To our best knowledge, thin film growth of lead oxy-chalcogenides have never been explored or reported. For these combined reasons, in this work, we applied the molecular beam epitaxy (MBE) with the controlled inclusion of oxygen atoms via Radio Frequency Oxygen Plasma source to study the growth of lead-oxy-chalcogenide thin films systematically. Controlled substrate temperatures were used to promote high crystal quality as well as assist in PbSe-O_2 interaction. By utilizing this in-situ growth method, a more uniform distribution of oxygen atoms interacting with PbSe can be accomplished compared to conventional post-growth thermal oxygen treatment, which sees a large interaction rate at the surface, but sharply decreases deeper into the film due to the nature of oxygen diffusion process. Using this method, we fabricated a new complex oxide in the form of ternary compound PbO_xSe_{1-x}. This new ternary compound complex oxide could be crucial in the understanding and future design of high-performance lead-chalcogenide based complex oxide semiconductor optoelectronic devices.

II. Experimental Methods

Oxygen plasma-assisted MBE Growth

Epitaxial PbSe was deposited by MBE on a freshly cleaved BaF_2 (111) substrate at a background pressure of 1×10^{-6} Pa and was used as a reference sample for subsequent growths. BaF_2 substrates were utilized for their excellent long wave optical transmittance and electrical insulation, allowing for both optical and electrical characterization to be carried out. Furthermore, BaF_2 substrates share similar cubic crystal structure, lattice parameter, and coefficient of thermal expansion with PbSe, whose relevant material parameters are provided in Table 3.1.

Table 3.1 ***Room temperature properties of BaF_2, PbSe, and common Pb-oxides and PbSe-oxides.***

Material	**Crystal Structure**	**Lattice Constant (Å)**	**Thermal Expansion (K^{-1})**	**Band Gap (eV)**
BaF_2	Cubic (Fluorite)	6.196	1.84×10^{-5}	11
PbSe	Cubic (Rock-Salt)	6.124	1.94×10^{-5}	0.27 (direct)[29]
PbO	Tetragonal	a = 4.06 c = 5.51	$a_o = 5.2\times10^{-6}$ [13] $c_o = 8.3\times10^{-6}$	1.9 (indirect)[30]
	Orthorhombic	a = 5.8931 b = 5.4904 c = 4.7528	a_o & $c_o = 3.1\times10^{-6}$ [15] $b_o = 9.8\times10^{-6}$	2.7 (indirect)[31]
$PbSeO_3$	Monoclinic	a = 4.5437 b = 5.5137 c = 6.6340	-	3.17 (direct)[32]

$PbSeO_4$	Orthorhombic	a = 8.5800 b = 5.6300 c = 7.1200	-	3.17 (indirect)[33]

Subsequently, PbSe evaporation via effusion cell was performed on the freshly cleaved BaF_2 (111) substrates under various conditions utilizing a RF oxygen plasma atom source. An oxygen background pressure of 5×10^{-3} Pa and 9×10^{-3} Pa was achieved with an oxygen flow rate of 0.8 sccm and 1.4 sccm respectively. The incursive oxygen molecules were ionized under RF mode inductive coupled plasma process at 250 W. The resultant films were deposited at substrate temperatures of 350 ˚C and 420 ˚C for 1hr, resulting in 1µm thick thin-films which are listed in Table 3.2.

Table 3.2 ***Growth Parameters of PbO_xSe_{1-x} Thin Films***

Sample	Substrate Temperature (ºC)	Oxygen Flow Rate (sccm)	Ionization Power (W)
PbOSe-1	350	0.8	250
PbOSe-2	350	1.4	250
PbOSe-3	420	0.8	250
PbOSe-4	420	1.4	250

While Pb-oxides and PbSe-oxides have been previously characterized, oxygen plasma-assisted MBE growth of $PbSe(O_x)$ films have never been studied. In addition to providing a list of relevant material properties for BaF_2 and PbSe, Table 3.1 also includes information on some of the previously reported Pb-oxides and PbSe-oxides which may have been expected to form under the

stated growth conditions. However, subsequent characterization of deposited thin films utilizing the compound PbSe effusion cell and RF oxygen plasma source indicated the formation of a new ternary PbO_xSe_{1-x} complex oxide. Surface morphology of PbO_xSe_{1-x} films was investigated by Scanning Electron Microscopy (SEM), while a Bruker Fourier-Transform Infrared Spectroscopy (FTIR) apparatus operating in mid-infrared (mid-IR) spectral range was used to characterize their optical properties. Electrical properties of PbO_xSe_{1-x} films were studied by performing Hall Effect measurements at room temperature. High Resolution X-ray diffraction (XRD) analyses was performed using a Rigaku Ultima IV diffractometer. Cu-K-alpha radiation (40 kV, 44 mA) was used in Parallel Beam mode, and data analysis was completed using the MDI Jade2010 software with the ICDD (International Centre for Diffraction Data) PDF4+ database. Long wave LO and TO phonon modes were investigated with a Renishaw inVia Raman Microscope, illuminated by a 532 nm 500 mW green laser excitation source.

III. Results and Discussion

Film Morphology and Composition

SEM images of all PbO_xSe_{1-x} thin films reveal the formation of a polycrystalline structure with densely packed grains, as shown in Figure 3.1 and Figure 3.2. Observing the surface morphology of PbO_xSe_{1-x} thin films in Figure 3.1 reveals the presence of [100] and [111] orientated grains. Cross section SEM images in Figure 3.2 display polycrystalline nature of PbO_xSe_{1-x} thin films grown with high packing density, smooth surface, good adhesion to the substrate, and uniform thickness between growths. Figure 3.3 serves as an aid for visualizing the difference in surface morphology of [100] and [111] cubic lattice structures.

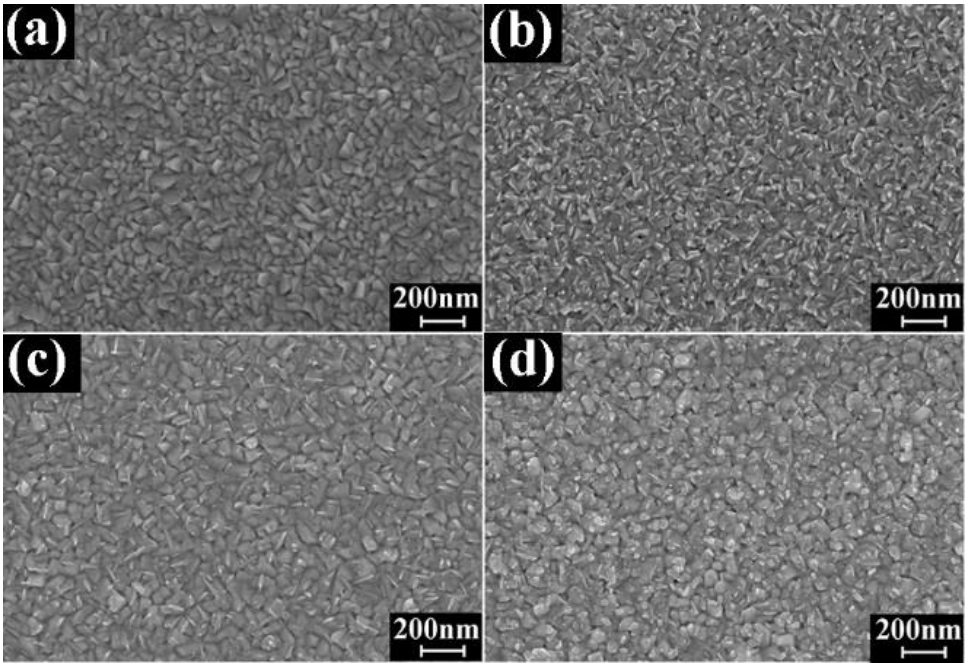

Figure 3.1 ***SEM surface images for:*** *(a) PbOSe-1 (b) PbOSe-2 (c) PbOSe-3 (d) and PbOSe-4 thin films.*

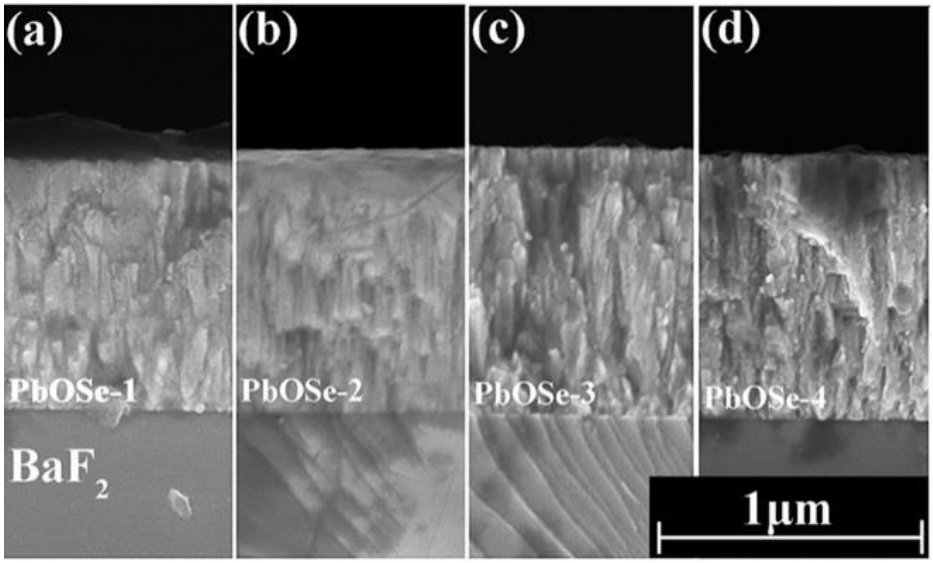

Figure 3.2 ***SEM cross section images of:*** *(a) PbOSe-1 (b) PbOSe-2 (c) PbOSe-3 (d) and PbOSe-4 thin films.*

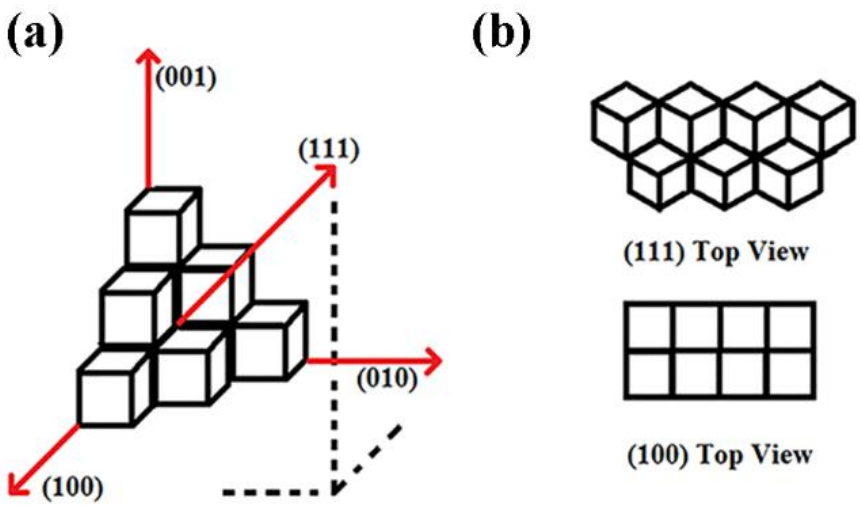

Figure 3.3 ***Visual Schematic for cubic crystal orientation:*** *a) about the point of origin given coordinates (x,y,z), and b) top view of cubic crystal structure.*

PbO_xSe_{1-x} films deposited at low oxygen flow rates (i.e. PbOSe-1 and PbOSe-3) contained mixed [111] and [100] orientated grains, while PbO_xSe_{1-x} films deposited at a higher oxygen flow rate showed preferred [100] orientated grains. The crystal growth for PbO_xSe_{1-x} films differed from the reference PbSe sample which grew [111] single crystal on the nearly lattice and thermal expansion matched BaF_2 (111) substrate. This result suggests that the growth mechanism for PbO_xSe_{1-x} thin films rely heavily on the influence of oxygen overpressure in the growth chamber. As per our reference sample, PbSe films deposited by MBE on BaF_2 (111) substrates typically grow epitaxial along the [111] direction. However, the presence of oxygen atoms on the growth surface, along with increased atomic scattering from the low vacuum environment during PbO_xSe_{1-x} deposition seems to have altered the nucleation process during crystal formation. As a result, this led to island growth with the presence of varying orientated grains. Although the formation of [111] orientated grains is typically preferred due to the closely lattice matched BaF_2 (111) substrate, competition for the [100] orientation now exists due to changes in surface and strain energy relations between

neighboring grains for the polycrystalline films. This phenomenon has been previously reported in Sun et al., where calculations of surface and strain energy densities for the physical deposition of polycrystalline PbSe films revealed a lower energy of formation for [100] orientated grains at substrate temperatures >250^{o}c[34]. Therefore, it is expected that polycrystalline growth of a PbSe-like rock salt structure, such as our PbO_xSe_{1-x} thin films, would result in the formation of [100] orientated grains at high substrate temperature deposition. In conjunction with SEM analysis, energy-dispersive X-ray spectroscopy (EDX) was employed in hopes of determining the oxygen "x" concentration of PbO_xSe_{1-x} thin films, resulting in "x" values ranging from $x = 0.2 - 0.35$. However, the resolving power of the EDX measurement did not allow for the distinction between contributions of elemental composition in crystal grains versus grain boundaries that exist in the polycrystalline PbO_xSe_{1-x} thin films. Due to the overpressure of oxygen in the growth chamber, as well as prolonged exposure to the atmosphere post-growth, large amounts of oxygen atoms may have diffused or imbedded themselves in the film via grain boundaries or defect centers. Similar phenomena have been reported previously, where lead rich n-type PbSe films converted to p-type after prolonged exposure to the atmosphere[35]. Researchers concluded that PbSe interaction with oxygen in the air resulted in the diffusion and incorporation of oxygen atoms into the film, producing the flip from n-type to p-type carrier concentration. These processes may have contributed to the overestimation "x" contained in the active PbO_xSe_{1-x} lattice structure by EDX measurements, due to oxygen interstitials and oxygen gas trapped in the grain boundaries during crystal formation and post-growth exposure to air. Therefore, EDX results could not be used to accurately determine oxygen composition. Further study using other techniques to determine the oxygen composition will be performed in future.

X-Ray Diffraction

Parallel Beam XRD analysis of PbO_xSe_{1-x} thin films, as shown in Figure 3.4, reveal a rock-salt crystal structure with preferred (200) peak contribution, along with possible (111) peaks masked by the BaF2(111) substrate peak. Investigation of XRD peak intensity and symmetry, along with full width half maximum (FWHM) of PbO_xSe_{1-x} (200) peaks, and slight lattice constant shifts, provide possible explanations of crystal formation and structure when compared with SEM images and reference PbSe films.

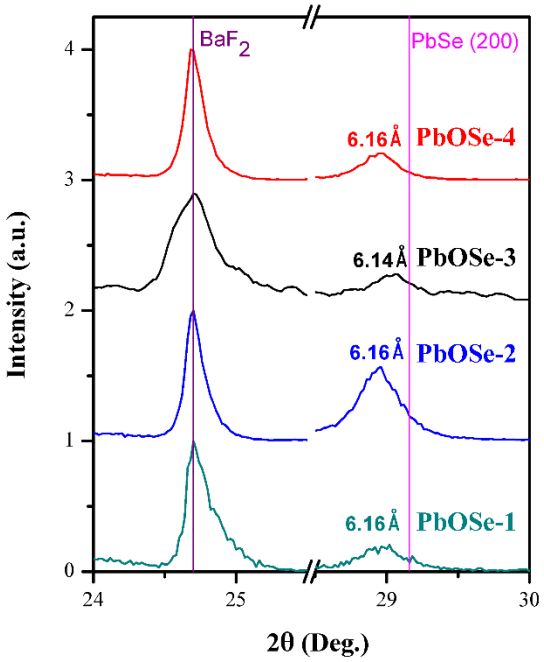

Figure 3.4 ***XRD spectra for PbO_xSe_{1-x} thin films.*** *The vertical lines denote the characteristic BaF_2 substrate peak position and the PbSe(200) reference peak position.*

No peak contributions from previously reported PbO, $PbSeO_3$, or $PbSeO_4$ were observed. However, a slight shift in the lattice parameter for deposited films was apparent given the offset in the PbO_xSe_{1-x} (200) peak positions relative to PbSe. Since the (200) peak belongs exclusively to the PbO_xSe_{1-x} film, measured 2θ shifts to lower angles from the reference PbSe (200) peak position signify an increase in lattice constant. While PbSe has a rock-salt structure with a lattice constant

of $a = 6.12$ Å, PbO_xSe_{1-x} films produced a slight lattice constant shift as shown in Table 3.3, ranging from $a = 6.14$Å - 6.16Å. While previous studies of Pb–O bonding report shortened bond lengths compared with Pb–Se bonds, XRD analysis suggest the ternary Pb–O–Se complex oxide forms an overall larger lattice constant compared with conventional PbSe films.

Table 3.3 ***Lattice parameter and FWHM of PbSe and PbO_xSe_{1-x} thin films.***

Film	**Lattice Constant (Å)**	**PbO_xSe_{1-x} (200) FWHM (arcsec)**
Reference Epitaxial PbSe	6.12	-
PbOSe-1	6.16	487.8
PbOSe-2	6.16	478.8
PbOSe-3	6.14	369.0
PbOSe-4	6.16	392.4

Since we observe shifting of the (200) peak position to lower 2θ angles, we should expect to see shifting of the (111) peak position to lower angles as well. However, this would make any PbO_xSe_{1-x} (111) peak contributions almost entirely overlapped with the BaF_2(111) substrate peak, making the PbO_xSe_{1-x} (111) film peak difficult to analyze. For this reason, we speculate that peak broadening and asymmetry of the BaF_2(111) substrate peak is possibly linked to an increase in the presence of a PbO_xSe_{1-x} (111) peak contribution. This effect is more pronounced in the low oxygen flow rate PbOSe-1 and PbOSe-3 samples, along with a reduction in the (200) peak intensity. In this case, XRD peak contributions coincide with observations made during SEM analysis, in which lower oxygen flow rates produced PbO_xSe_{1-x} crystal films with lower (200) vs (111) ratios. Table 3.3 also includes investigation of the full width half maximum (FWHM) of PbO_xSe_{1-x} (200) XRD

peaks. According to Scherrer's equation, the larger measured FWHM values found in PbOSe-1 and PbOSe-2 suggest the formation of smaller grain sizes compared to the high substrate temperature growths, which is also observed in top-down SEM images in Figure 3.1.

Raman Spectroscopy

Raman Spectra of the reference PbSe film reveals characteristic PbSe Longitudinal and Transverse Optical phonons, which have been previously reported in similar MBE grown PbSe films[36]. Figure 3.5 shows that for PbO_xSe_{1-x} films, a singular peak at the LO, 2LO and 2TO peak positions were present, while no individual phonon mode contribution from either PbSe or PbO were detected.

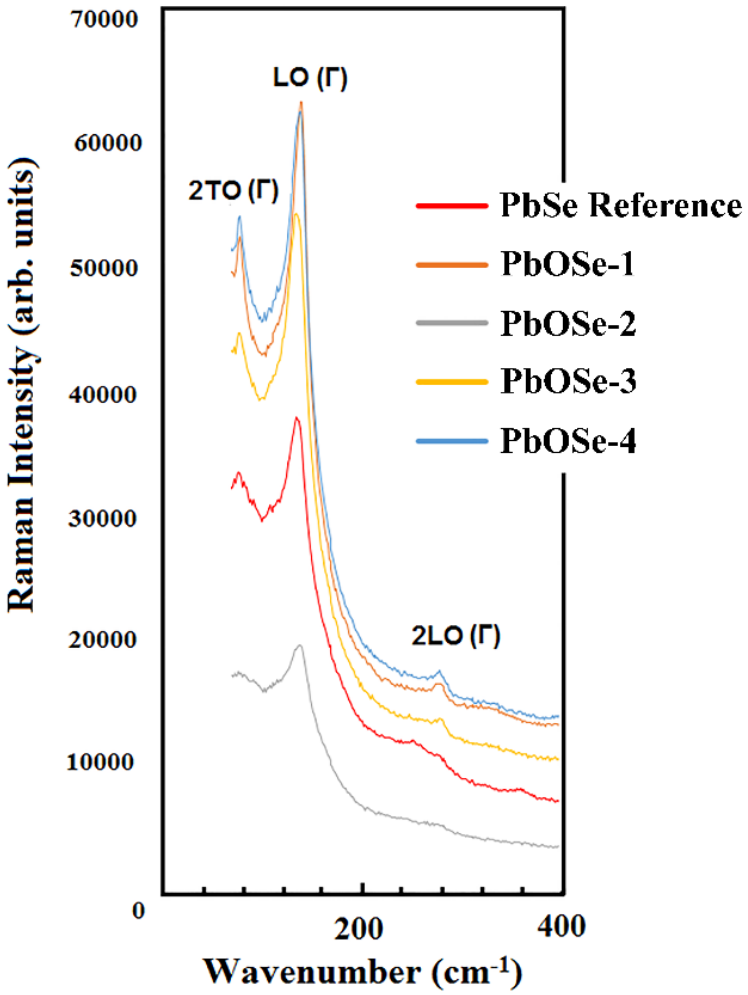

Figure 3.5 ***Raman spectra of PbO_xSe_{1-x} films.***

Table 3.4 ***Peak positions of 2TO, LO, and 2LO phonon modes in PbO_xSe_{1-x} films.***

Sample	2TO (cm^{-1})	LO (cm^{-1})	2LO(cm^{-1})
PbSe Reference	79	136	271
PbO Tetragonal	81	145.5	337
PbO Orthorhombic	71.5	143	289.5
PbOSe-1	80	141	280
PbOSe-2	80	142	283

PbOSe-3	79	137	273
PbOSe-4	80	138	278

This indicates that there is no separated PbSe or Pb-oxide phase present in the film, further supporting that a ternary PbO_xSe_{1-x} crystal structure has been formed. Subsequently, PbO_xSe_{1-x} films show similar PbSe like profiles, but with slight variations in LO, 2LO, and 2TO phonon peak positions. Raman shift of PbO_xSe_{1-x} films reveal a shifting of LO and 2LO phonon peak positions to higher wavenumbers compared with the reference PbSe film. The LO phonon mode contains the highest intensity for all deposited films, with increasing wavenumber for each subsequent PbO_xSe_{1-x} sample ranging from 0.7% up to a maximum of 4.4%. Comparing the previous investigations into Raman shift for PbO films listed in Table 3.4, our PbO_xSe_{1-x} thin films experienced a Raman shift in between that of PbSe and PbO. As a ternary compound, the PbO_xSe_{1-x} Raman shift is the result of a ratio between Lead-Selenium and Lead-Oxygen bonding, where Raman shift approaching that of characteristic PbO phonon modes is a result of increasing oxygen concentration, producing more Lead-Oxygen bonds. The largest difference in Raman shift was observed for the PbOSe-2 film deposited at the lower 350 ^oC substrate temperature and higher 1.4 sccm oxygen flow rate. Conversely, the PbOSe-3 film deposited at the higher 420 ^oC substrate temperature and lower 0.8 sccm oxygen flow rate resulted in the smallest difference from characteristic PbSe LO, 2LO and 2TO phonon peak positions. It has been previously reported that Raman shift $\Delta\omega$ varies depending on composition and temperature effects as they relate to bond length and energy, and may be represented by the following equation[37],

$$\Delta\omega \propto \frac{zE_b(z)^{\frac{1}{2}}}{d(z)} \ldots\ldots\ldots\ldots 3.1$$

Where z is the atomic coordination number, and $d(z)$ and $E_b(z)$ are the bond length and energy respectively. Comparison of crystal films measured at the same ambient temperature observe an increase in Raman Shift due to either a decrease in bonding length or an increase in bonding energy resulting from differences in composition. Although XRD measurements revealed a slight increase in bonding length of +0.02-0.04Å for PbO_xSe_{1-x} films compared with PbSe, the Raman shift observed an increase rather than a decrease in $\Delta\omega$. This is likely due to the reported energy difference of Pb–O bonds and Pb–Se bonds, where the Pb–Se bond (302.9±4 kJ mol−1) requires less energy to be broken than the Pb–O (382.0 ± 12.6 kJ mol−1) and Se–O (464.8 ± 21.3 kJ mol−1) bond[38]. The energy relation between these bonds suggests that the inclusion of oxygen atoms during crystal formation more readily break the Pb–Se bond to form higher energy Pb–O, and possibly Se–O and Pb–O–Se chain bonds.

Optical Properties

Figure 3.6 depicts the absorption spectra of PbO_xSe_{1-x} films measured by FTIR, which revealed a blue shift in the optical band gap compared with the reference PbSe sample. The band gap energies provided in Table 3.5 show that the optical absorption edge of PbO_xSe_{1-x} thin films resulted in a blue shift ranging from +48% to +89% relative to the reference PbSe film.

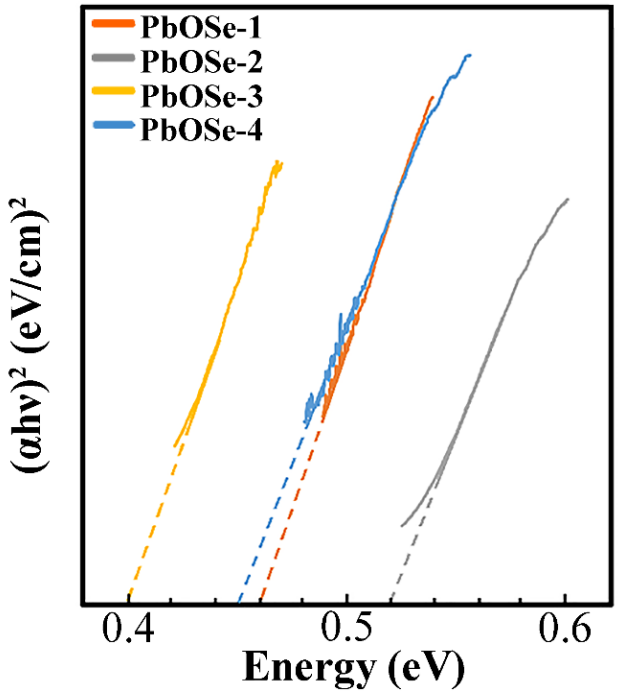

Figure 3.6 ***Band gap determination of PbO_xSe_{1-x} thin films.***

Table 3.5 ***Measured optical bandgap for PbSe and PbO_xSe_{1-x} films.***

Sample	Band Gap (Direct)
Epitaxial PbSe	0.27 eV
PbOSe-3	0.4 eV
PbOSe-4	0.45 eV
PbOSe-1	0.46 eV
PbOSe-2	0.51 eV

It is important to note that the PbOSe-2 thin film, which contained the largest difference in Raman shift, also resulted in the largest blue shift of the optical band gap compared to the reference PbSe film. Conversely, the PbOSe-3 film, which contained the smallest difference in Raman shift, also resulted in the smallest blue shift of the optical band gap. This suggests a trend, in which property

changes associated with enhanced oxygen atom incorporation during crystal formation result from both the lower 350 ^{o}C substrate temperature as well as an increased oxygen flow rate during deposition.

Electrical Properties

Electrical properties of PbO_xSe_{1-x} films grown under varying conditions are shown in Table 3.6.

Table 3.6 ***Electrical properties of PbO_xSe_{1-x} thin films.***

Sample	PbOSe-1	PbOSe-2	PbOSe-3	PbOSe-4
Carrier Concentration (cm^{-3})	1.79×10^{18}	1.26×10^{19}	3.13×10^{18}	9.82×10^{18}
Carrier Mobility ($cm^2/V\cdot s$)	53.19	0.42	11.95	3.95

Hall Effect measurements reveal that all PbO_xSe_{1-x} films are dominated by hole transport, with increasing p-type carrier concentration ranging from 1.79×10^{18} cm^{-3} to 1.26×10^{19} cm^{-3} observed for films grown with increasing oxygen flow rate. Conversely, carrier mobility decreases with increasing oxygen flow rate, pointing towards possible increases in impurity scattering, carrier scattering, alloy scattering, and grain boundary scattering. Comparing Hall measurements with SEM, XRD, and bandgap shift, the largest decrease in mobility observed in PbOSe-2 may be explained by contributions of all the above mechanisms. For example, the large FWHM of PbOSe-2 implies smaller crystal size, which is also observed in the SEM image in Figure 3.1, resulting in increased boundary scattering of carriers at grain-grain interfaces. Further, the carrier concentration of the PbOSe-2 film was the highest of all PbO_xSe_{1-x} thin films, almost a

magnitude higher than PbOSe-1, leading to the potential for heavy carrier scattering. PbOSe-2 also observed the largest bandgap shift from PbSe resulting from increased oxygen atom incorporation, potentially increasing alloy scattering and further reducing carrier mobility. Other PbO_xSe_{1-x} films may be similarly affected by these mechanisms, however, PbOSe-2 displays the largest decrease in mobility due to having the highest oxygen atom incorporation along with smaller relative grain size. Previous reports of ternary compounds such as $PbSr_xSe_{1-x}$ and $PbEu_xTe_{1-x}$ have been used to increase the bandgap energy for IV-VI Pb-salt based semiconductor opto-electronic devices to be used as electrical confinement layers[39], [40]. In doing so, the mobility decreased exponentially with Sr or Eu composition in comparison to PbSe. The p-type doping concentration in such ternary compounds is also limited, not being able to achieve high doping concentrations close to $1.0\times10^{19}\,cm^{-3}$. This new PbO_xSe_{1-x} ternary compound has succeeded in forming a larger bandgap, nearly the same lattice constant as PbSe, and high p-type doping concentration. This, plus the positive role of defect passivation, oxygen may make this new PbO_xSe_{1-x} complex oxide attractive for PbSe related opto-electronic devices. The band alignment between this new complex oxide and PbSe will need to be studied further to better our understanding of existing oxygen treated PbSe films, and may lead to the development of new MWIR PbSe-based technologies.

4. INTEGRATION OF EPITAXIAL IV-VI Pb-CHALCOGENIDE on GROUP IV VICINAL Ge SUBSTRATE TO FORM p-n HETEROGENEOUS STRUCTURES

I. Introduction

Germanium-based opto-electronic devices are a fascinating branch of emerging state-of-the-art technologies. While the germanium material system boasts decades of maturity and large industrial scalability, the limitations of its physical properties dictate the reach of its potential applications. For this reason, the development of new heterogeneous structures that combine the attractive attributes of germanium with the unique properties of other developed material systems may help push the boundaries of innovation in both science and commercial industries. Among these applications, low-cost MWIR sensing and imaging is of considerable interest, with widespread applications not currently being accessed by germanium-based opto-electronic devices. While germanium has proven its effectiveness in the short-wave infrared (SWIR) regime, here we create a novel heterogeneous material structure by depositing MWIR absorbing monocrystalline n-PbSe film on p-Ge substrate, forming a p-n heterojunction with room temperature MWIR photovoltaic detector capabilities. Traditionally, materials such as PbSe and Ge have been found difficult, if not unsuitable for fabricating heterogeneous structures due to their large difference in lattice constant and thermal expansion coefficient. These dissimilar properties often give rise to strain-induced defects, ruining interface and bulk phenomena that researchers may hope to exploit with their material system. While IV-VI materials such as PbSe show promise

in numerous MWIR optoelectronic and topological applications, the limitations of growing high-quality monocrystalline films on both low-cost and scalable substrates have been a major point of interest for researchers in recent years[41]–[45]. Due to both availability and scalability, IV-VI Pb-chalcogenide semiconductors such as PbSe are often grown on many dissimilar substrates inhibiting the formation of high-quality monocrystalline films. Further, while most of the substrates being used for epitaxial growth such as BaF_2, CaF_2, KCl, and $SrTiO_3$ may provide beneficial mechanical, thermal, and optical properties, they are also electrically passive insulators in the heterostructure acting only as a platform to grow epitaxial films. Direct Growth of PbSe on an electrically active substrate could combine the merits of two materials and offer new device structures to advance state-of-the-art performance while reducing cost and increasing scalability[46]. Combining high-quality monocrystalline PbSe with relevant Si, Ge, or III-V material systems would improve a host of device applications including MWIR lasers, detectors, thermoelectric devices, and topological crystal insulators. However, the direct growth of high-quality PbSe films on electrically active substrates is exceedingly difficult due to the challenges discussed above. For example, direct growth on Si substrate without a CaF_2 buffer layer tends to form cracks or has inferior material quality[47]. More recently, efforts have been made to expand the list of suitable substrates for epitaxial growth of PbSe to include III-V materials such as GaAs, GaSb, and InSb[7]–[9]. While there has been promising success on these substrates, each material system comes with its own design hurdles, such as small critical thickness, high defect densities, or electrically inactive use of the substrate/ film interface. Additionally, growth of IV-VI/III-V heterostructures face challenges regarding growth orientation due to the nature of defect slip planes. IV-VI rock salt structure materials like PbSe have a primary slip system along $\{001\}\langle 1\bar{1}0\rangle$ resulting in preferential dislocation gliding along the {001} plane. The result of

which is that the slip system for accumulated dislocations in PbSe films grown in the (100) orientation feel no resolved shear stress from in-plain strain, locking dislocations in place. This handicap for PbSe films grown in the (100) orientation is often avoided by using (111) orientated substrates. However, demonstration of high-quality monocrystal PbSe films grown in the (100) direction would allow for the utilization of the more industry standard (100) substrates, improving both production costs and scalability. For this reason, we chose to deposit PbSe films on Ge (100) substrates to take advantage of these attractive attributes. Conversely, epitaxial IV-VI films grown directly on CdTe substrates or composite CdTe/Si (211) substrates have been demonstrated, and mid-infrared detectors using PbTe/CdTe interface properties have also been reported[48]–[50]. However, there has been no report of devices that utilize the direct growth of thick monocrystalline PbSe film on electrically active substrates for device applications. Table 4.1 provides an extensive summary of PbSe growth's current progress on both similar and dissimilar substrates.

Table 4.1 ***List of relevant substrate electrical and optical properties compared with PbSe.***

Material System	**Substrate Treatment**	**Lattice Mismatch (Å)**	**Thermal Expansion Coef. Mismatch**	**Bandgap (eV)**	**Electron Affinity (eV)**	**Crystallinity**
PbSe/CaF2/ Si	-	12.1% (6.126/5.464/5.431)	1.5% (19.4/19.1)	0.27/12/1.17	4.6/1/4.05	Single
PbSe/BaF2 **[47]**	-	1.19% (6.126/6.2)	2% (19.4/19.8)	0.27/9.1	4.6/2.1	Single
PbSe(111)/ Si(111) **[47]**	-	12.7% (6.126/5.431)	746% (19.4/2.6)	0.276/ 1.17	4.6/4.05	Poly
PbSe/KCl **[51]**		2.63% (6.126/6.292)	46% (19.4/36)	0.27/ 8.4	4.6/0.5	Single
PbSe(100) /GaAs(100) **[52]**	Te	8.3% (5.653/5.431)	338% (19.4/5.73)	0.27/ 1.41	4.21/4.07	Single
PbSe (511)/ GaAs(211)B **[52]**	Te	4.1%	338% (19.4/5.73)	0.27/ 1.42	4.6/4.07	Single

PbSe(001)/ GaSb(001) **[53]**	-	0.5% (6.126/6.095)	250% (19.4/7.75)	0.276/ 0.726	4.6/4.06	Single
PbSe(001)/ InAs(001) **[53]**	PbSe	1.1% (6.126/6.058)	429% (19.4/4.52)	0.276/ 0.36	4.6/4.9	Single
PbSe(111)/ InAs(111)A **[54]**	PbSe	1.1% (6.126/6.058)	429% (19.4/4.52)	0.276/ 0.36	4.6/4.9	Single
PbSe/SrTiO 3**[55]**		56.8% (6.126/3.905)	202% (19.4/9.6)	0.276/ 3.2	4.6/3.57	Topological Crystal Insulator
PbSe/Ge	Se	8.2% (6.126/5.658)	328% (19.4/5.9)	0.276/ 0.67	4.21/4	single

In addition to the interface and material quality, the band alignment of the heterojunction is exceedingly important for device applications. Figure 4.1 shows reported values of electron affinity (EA) and energy bandgap for PbSe and its most common substrate materials.

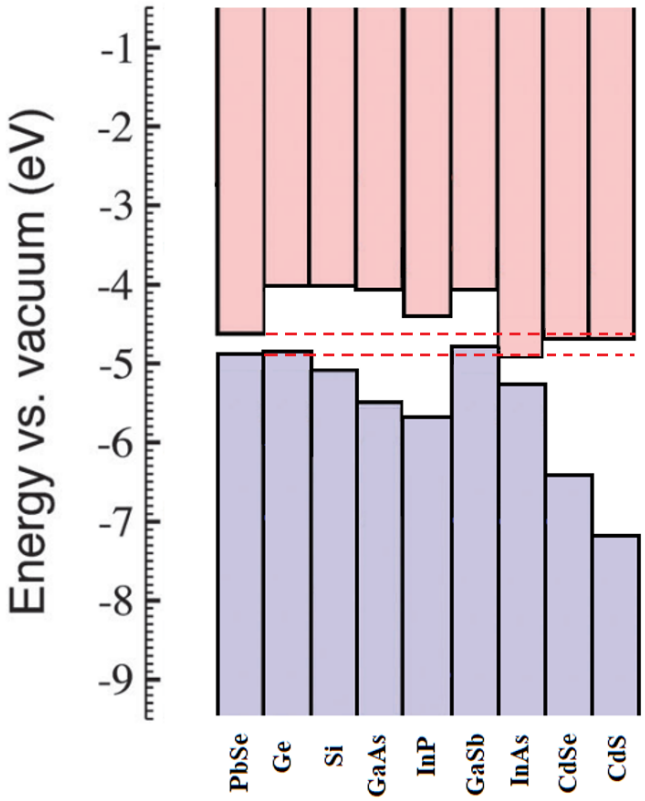

Figure 4.1 ***Conduction and valence band edge alignment for PbSe and other relevant material systems.***

Based on the EA values in Figure 4.1, PbSe forms a type-I band alignment with Si, GaAs, and InP, making them suitable for heterojunction light emitting devices, while the PbSe/InAs material system has a staggered type III band alignment. Among the listed substrate materials, Ge forms a type-II heterojunction with PbSe while adding its own host of attractive attributes, making it a suitable candidate for p-n heterojunction photovoltaic device structures. To date, low-cost PbSe MWIR photoconductors operating at uncooled or Thermoelectric (TE)-cooled temperatures remain the choice for many sensing and imaging applications[56]. Polycrystalline PbSe mid-wave infrared (MWIR) photoconductors have reported D* values at room temperature of 2.8×1010 cm·Hz1/2/W and 4.2×1010 cm·Hz1/2/W at ~3.8 μm, without and with antireflective coating[10], [27], [57]. Such high performance is attributed to its low Auger recombination rate at high temperatures. Auger coefficient in IV-VI semiconductors such as PbSe is roughly an order of magnitude lower than those in Sb-based type-II QWs, which are in turn significantly suppressed relative to other III-V and II-VI semiconductors such as MCT with the same energy gaps[58]–[64]. Although very promising performance has been demonstrated by polycrystalline PbSe photoconductor (PC) focal planar arrays (FPA), several problems are still associated with their design, including film inhomogeneity, large 1/f noise and limited FPA resolution due to contact configuration for PC detectors. Ideally, if one could develop PbSe photovoltaic detectors with the same performance as its PC counterpart, these problems could be solved. Previous efforts to make Pb1-xSnx Se PV detectors using epitaxial films on Si with Pb Schottky junction have made significant progress, but the performance is inferior to MCT detectors[54]. One key performance limiting factor is the difficulty to make a p-n junction detector that can outperform its Schottky counterpart. The problem is due to impurity diffusion at the p-n junction interface. To solve these problems and further improve the performance, heterojunction CdS/epi-PbSe on Si substrate and

CdSe/PbSe detectors directly grown on conductive oxide/metal for monolithic integration with Si readout integrated circuit (ROIC) have been made[3], [15], [28]. However, the conduction band of CdS and CdSe seems somewhat higher than that of PbSe which could block some of the photo-generated carriers. For IV-VI MWIR/LWIR semiconductors with bandgap energies of interest in the range of 0.1-0.3 eV, it is very challenging to find proper materials to form heterojunction structures for photovoltaic detectors. The n-PbSe/p-Ge heterojunction has several unique advantages over the previous approaches. First, Ge serves not only as a substrate, but also as part of the heterojunction being a SWIR absorber and hole transport layer. Therefore, PbSe/Ge heterojunction monolithically integrates Ge and PbSe, naturally forming a dual-band MWIR/SWIR or PV detector. Second, the heterojunction could significantly reduce the dark current. Third, since Ge on Si substrate is commercially available, large-format PbSe/Ge/Si heterojunction detectors can be fabricated, as well as monolithically integrated PbSe /Ge/Si FPA on Si ROIC. Figure 4.2 shows a schematic drawing of band alignment of PbSe and Ge, and carrier transport of PbSe/Ge heterojunction.

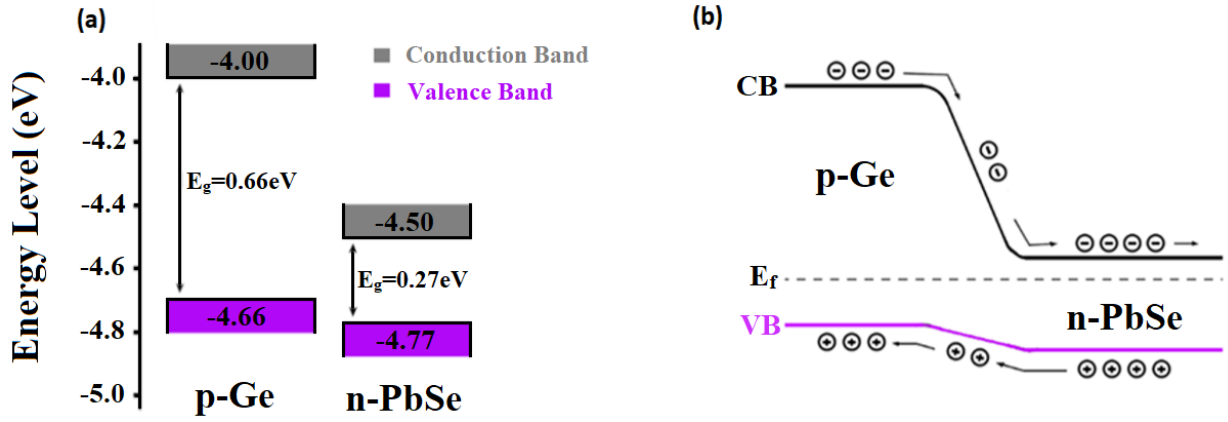

Figure 4.2 ***Schematic drawing of:*** *(a) n-PbSe/p-Ge band alignment and (b)carrier transport in n-PbSe/p-Ge heterojunction structure.*

In this work, we demonstrate a method for growing monocrystalline n-type PbSe on a p-type Ge substrate without the use of a thick buffer layer. The result of our efforts showcases both the ability to grow a thick monocrystalline film on a dissimilar substrate along with the formation of high-quality p-n heterojunction. The growth of monocrystalline PbSe on Ge has not been previously demonstrated, and the techniques employed here may allow for the introduction of other new combinations of materials to be explored.

II. Experimental Details

Material Growth and Characterization

The n-PbSe/p-Ge heterojunction was formed in a custom MBE system by direct evaporation of 99.9999% pure Se-rich PbSe in combination with a 99.999% pure Bi_2Se_3 as the n-type dopant. PbSe deposition was performed on a clean vicinal p-Ge substrate with carrier concentration of $1\times10^{17}cm^{-3}$ and surface orientation <100> with a 6^{o} miscut towards <111> at a substrate temperature of 375˚C. A Bi_2Se_3 beam flux was maintained at 0.01% of the PbSe beam flux to achieve n-PbSe films with carrier concentrations of $8\times10^{17}cm^{-3}$. Before PbSe deposition, Ge substrates were cleaned by chemical method then loaded into the MBE for thermal cleaning to encourage desorption of the surface oxide layer. Surface treatment of the germanium substrate was performed at 400^{o}C using a 99.999% Selenium before depositing PbSe films. In-situ RHEED analysis was performed using the KSA 400 data acquisition and analysis software. Cross-section and surface morphology were observed by scanning electron microscopy (SEM) and atomic force microscopy (AFM) operating in non-contact mode (NCM). High-resolution XRD analyses were performed using a Rigaku Ultima IV diffractometer. Cu Kα radiation (40 kV, 44 mA) was used in

parallel beam mode, and data analysis was completed using the MDI Jade2010 software with the ICDD (International Centre for Diffraction Data) PDF4+ database. Photoluminescence measurements were conducted in CW mode using a Bruker Fourier transform infrared spectroscopy (FTIR) apparatus. Current-voltage analysis was performed using a Keithley 2400 Standard Series Source Measure Unit.

III. Results and Discussion

In-Situ RHEED Analysis

In-situ RHEED measurements were performed before, during and after PbSe growth on germanium substrates. RHEED pattern changes were observed for both the Se surface treatment period as well as the nucleation stage and bulk growth portion of PbSe films. Transformation of the characteristic Ge RHEED lines were observed during the Se treatment period, with the disappearance of Ge reconstruction lines along with the formation of dots, indicating the presence of a new surface. This RHEED transformation could be caused by Ge-Se bonding that results in Se terminated surface, or formation of a very thin compound material such as GeSe, or $GeSe_2$. However, there is no noticeable change in the diffraction pattern and line spacing, indicating the surface layer maintains the same crystal structure and orientation as the germanium substrate. Immediately after opening the PbSe shutter, the RHEED pattern quickly changes back to lines while decreasing in line spacing until stabilizing for the duration of the growth. Figure 4.3 shows the evolution of the RHEED pattern as the growth process develops.

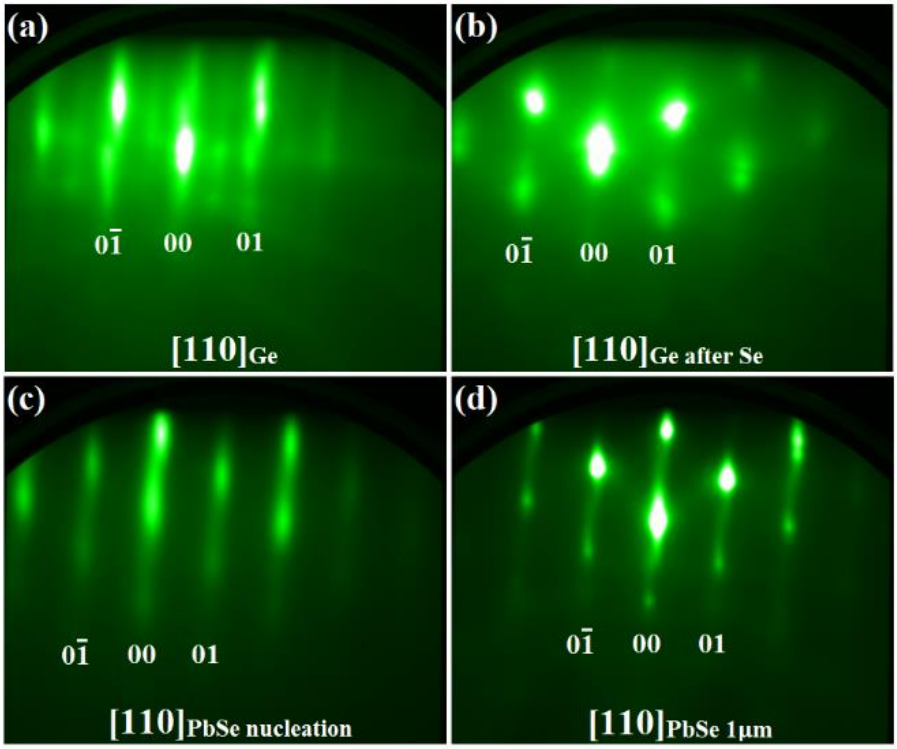

Figure 4.3 ***RHEED images of the:*** *(a) cleaned vicinal germanium substrate with reconstruction, (b) substrate surface after Se treatment, (c) film surface during the first monolayers of PbSe growth (d) and the final 1µm thick PbSe film surface.*

The initial RHEED pattern of the PbSe nucleation stage and thin bulk growth begins with a relatively diffuse line profile. As PbSe thickness increases, line intensity continues to increase along with decreasing line spacing and diffusivity. After roughly 11nm of PbSe deposition, RHEED line spacing stabilizes and remains unchanged for the duration of the growth. This phenomenon indicates the presence of a compressive lattice strain during the initial stages of PbSe growth, gradually relaxing with increasing film thickness until it reaches roughly 11nm. Further, the vicinal nature of the substrate can be observed in the RHEED line profile with the presence of a slight tilt and separation in the RHEED lines. Rotating the substrate 180˚ results in the same observed RHEED pattern but tilted in the opposite direction. Post growth RHEED analysis reveals a strong monocrystalline PbSe (001) orientated surface with no signs of polycrystalline grains.

Microscopy

Scanning electron microscopy and atomic force microscopy were used to both visually observe and investigate cross-section and surface morphology for the n-PbSe/p-Ge crystal structure. The SEM cross-section observed in Figure 4.4 reveals the epitaxial nature of PbSe deposited on vicinal germanium substrate.

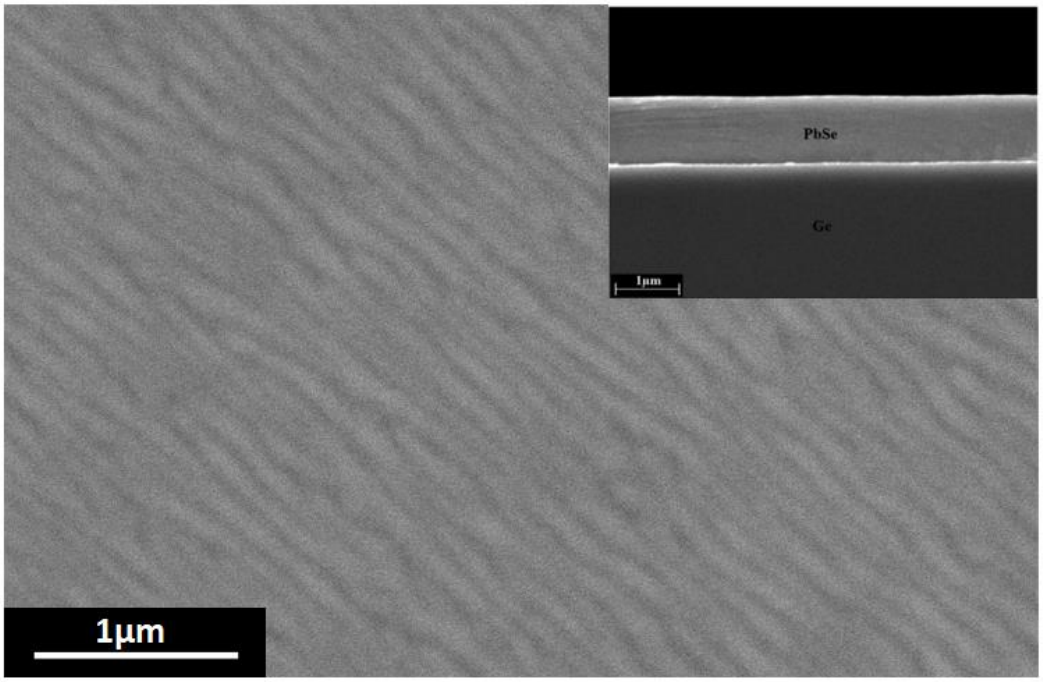

Figure 4.4 ***SEM image of PbSe on Ge:*** *Surface image indicates a meandering growth mode of epitaxial PbSe films with no observable cracks over a large area, with the in-set cross-sectional image corroborating the RHEED observations of a bulk single crystalline PbSe film.*

Within the resolution of the SEM, no indication of a sufficiently thick interface layer is present at the PbSe/Ge interface despite the Se surface treatment of the Ge substrate and resulting RHEED transformation. Glancing angle XRD, XPS, and Raman have been employed to further investigate on the Se treated germanium substrates without deposition of PbSe films, but there is no indication of any new surface material. Future work aimed at investigating the presence of a possible interface layer between PbSe and germanium will involve cross-section transmission electron

microscopy (TEM) in attempt to directly observe the bonding nature of this novel heterojunction interface.

PbSe surface morphology observed by AFM surface profile indicates a slight surface roughening due to the apparent step-meandering nature of the PbSe growth, along with observation of long-range order parallel peaks and valleys as seen in Figure 4.5[65].

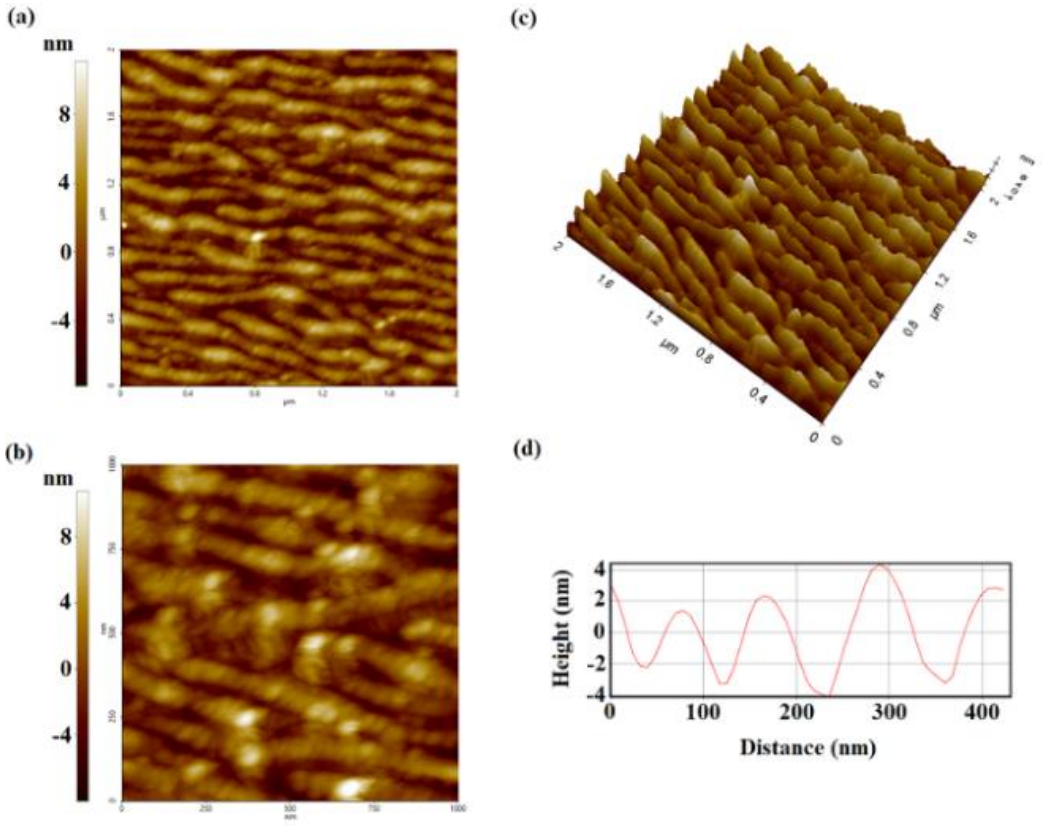

Figure 4.5 ***AFM image of step-meandering growth observed in PbSe films:*** *(a) 2µm x 2µm NCM surface profile scan, (b) 1µm x 1µm NCM surface profile scan, (c) 3D surface view, and (d) height profile measurement.*

The AFM surface profile in Figure 4.5 reveals a surface morphology dominated by parallel growth peaks, separated by thin valleys of shallow depth. With most of the surface area dominated by the atomically smooth growth peaks, the average surface roughness of 1.8nm is mostly due to the thin

valleys with an average depth of 5nm. However, with an average depth of only 5nm, coalescence of these growth areas is likely to occur in the bulk film resulting in a uniform monocrystalline bulk PbSe layer as observed in cross-sectional SEM. While the influence of growth temperature and deposition rate has been previously reported for films grown on vicinal substrates, for materials with dissimilar lattice constant and thermal expansion coefficient, the effectiveness of these parameters on enhancing epitaxial growth becomes drastically reduced.[66] In our case, the Se treatment period of the Ge substrate seems to play a critical role in lowering the interface energy of Pb adatoms on the growth surface, allowing for sufficient surface diffusion contributing to enhanced nucleation and subsequent layer-by-layer growth. Without this procedure, Pb and Se adatom interactions dominate over the Ge surface inducing three-dimensional adatom clusters, resulting in Volmer-Weber growth, leading to the formation of polycrystalline grains. Observation of this effect can be found in the supplemental materials sections using top-view SEM on a PbSe film surface deposited on a bare germanium substrate.

Photoluminescence and X-Ray Diffraction

XRD was used to identify characteristic PbSe peaks and verify the in-situ RHEED measurements which indicate the successful growth of monocrystalline PbSe on germanium. First, a wide-angle scan was performed to identify all possible contributing peaks, followed by rocking-curve XRD to investigate PbSe full-width half maximum (FWHM), as seen in Figure 4.6.

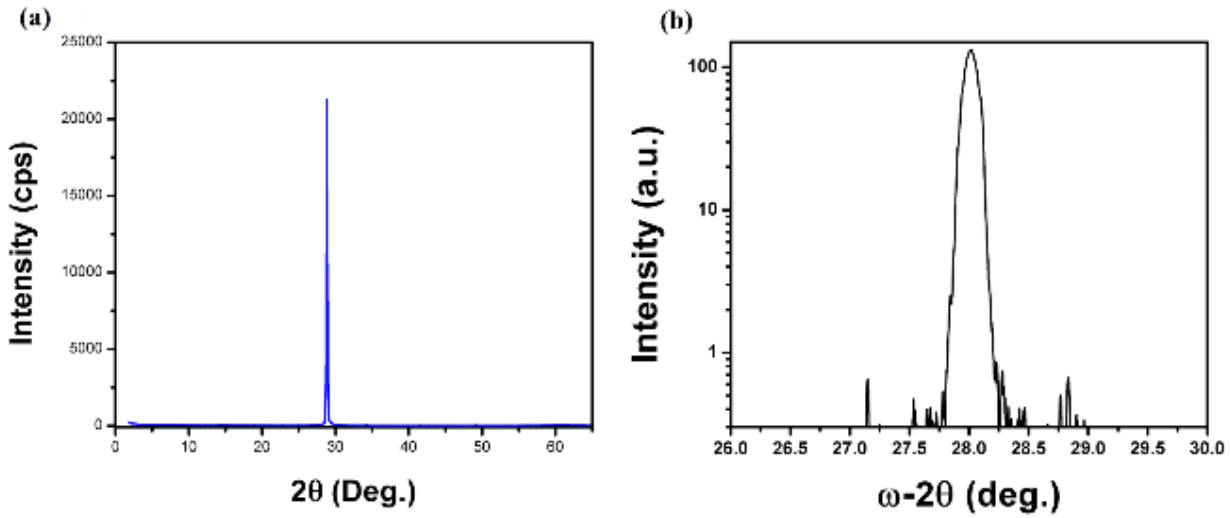

Figure 4.6 ***XRD pattern for the n-PbSe surface deposited on vicinal germanium substrate:*** *(a) wide-angle scan and (b) rocking curve.*

The only major identifiable peak belongs to PbSe (002), with minimal contribution from the equivalent (004) PbSe peak. High-resolution rocking curves taken along the (002) axis reveal a FWHM of 248arcsec for the dominating PbSe peak. Table 4.2 provides a comparison of the measured FWHM value for PbSe deposited on Ge (100) with PbSe films deposited on other dissimilar substrates with the potential for type-II band alignment, along with FWHM values reported for PbSe grown on nearly lattice matched and thermal expansion coefficient matched insulating BaF_2 (111) and CaF_2/Si (111) substrate respectively.

Table 4.2 ***Comparison of measured and reported XRD FWHM values for PbSe films on foreign substrates.***

Structure	Orientation	Thickness (nm)	FWHM (arcsec)
PbSe/Ge	(100)	1,000	248
PbSe/GaSb[53]	(100)	15ML	---
PbSe/InAs[53]	(100)	310	181
PbSe/InAs[54]	(111)	2,000	1700
PbSe/BaF_2[67]	(111)	1,000	90-275
PbSe/CaF_2/Si**[68]**	(111)	1,000	140-300

Compared to PbSe films deposited on other dissimilar substrates, the PbSe on Ge shows a markedly improved FWHM value, indicating strong crystalline material quality. The low measured FWHM value for PbSe on InAs (100) was only achievable for the optimized 310nm film thickness. Thinner PbSe films on InAs (100) were found to have a larger FWHM of 444 arcsec, while thicker PbSe films formed cracks and increased dislocation densities due to the buildup of stress.[53] Further, while the PbSe film on lattice matched BaF_2 substrates often obtain the lowest FWHM values, the PbSe film on Ge has a measured FWHM falling neatly within the typical range expected for PbSe films deposited on the nearly lattice matched and thermal expansion coefficient matched BaF_2 and CaF_2/Si substrates. Photoluminescence measurements were also employed to investigate material quality. Figure 4.7 compares room-temperature continuous wave (CW) PL intensity values for the n-PbSe/p-Ge crystal structure with PbSe films deposited BaF_2 substrate.

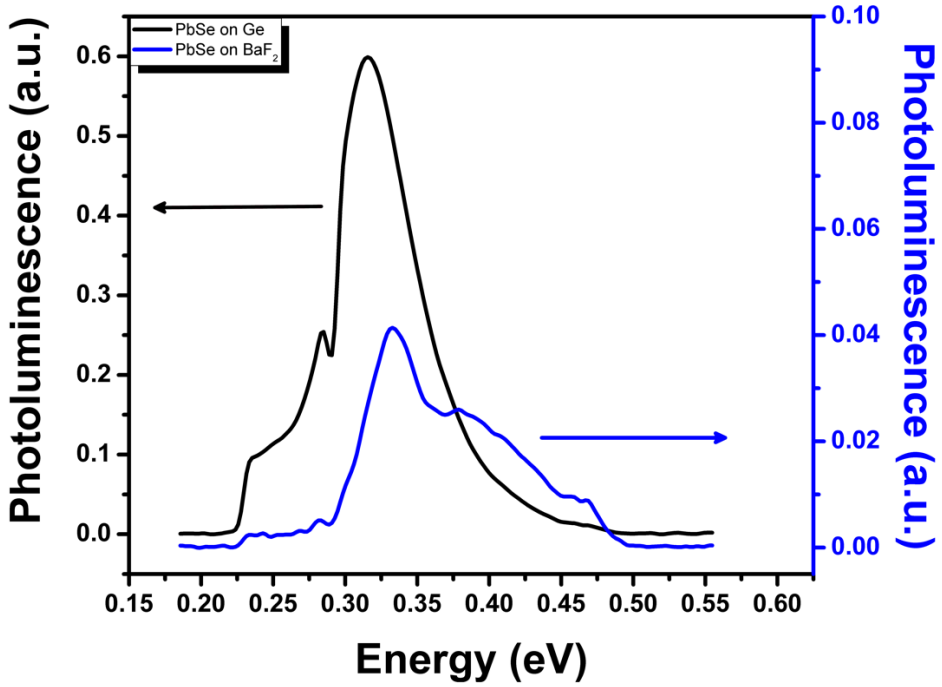

Figure 4.7 ***Room-Temperature CW PL spectra of PbSe films deposited on Ge and BaF_2.***

Significant blue shift of the PbSe PL peak was observed for both PbSe on Ge and BaF_2 substrates. This is attributed to the heating effects associated with CW pumping of the samples, where the low thermal conductivity of germanium (60.2 $Wm^{-1}K^{-1}$) and BaF_2 (11.72 $Wm^{-1}K^{-1}$) result in a higher PbSe lattice temperature than the heat sink temperature.[69] In comparison, PbSe on Ge shows promising CW PL properties with more than a magnitude higher PL intensity compared with monocrystalline PbSe on lattice matched BaF_2 substrate, indicating strong crystalline material quality. With such promising PL recorded for PbSe on electrically active Ge substrates, this novel heterostructure may also find use in MWIR light emitting device applications.

Current-Voltage Statistics

Current-voltage (I-V) measurements were taken on the 270µm x 270µm pixel contacts, ranging from -0.5V to 0.5V. Strong p-n junction behavior was observed at room temperature, with consistently large rectifying factor and low reverse bias current densities for all pixels as seen in Figure 4.8. Current density (J) calculations used only the pixel area covered by the Au contact fingers to avoid overestimation of J-V performance. The low series resistivity measured for the n-PbSe/p-Ge material structure indicates the formation of an ohmic contact, ensuring direct characterization of the heterojunction behavior absent any influence from poor contact formation. Table 4.3 provides a list of both measured and calculated values of interest indicating strong p-n junction behavior suitable for room temperature MWIR detector applications.

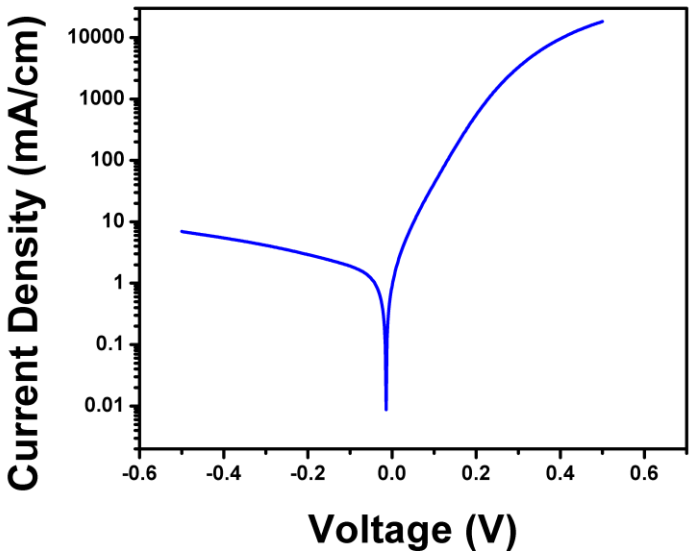

Figure 4.8 ***Room Temperature J-V statistics.***

Table 4.3 ***Measured and calculated values of interest.***

Structure	Contact Dimension	Shunt Resistivity (Ω cm)	Series Resistivity (Ω cm)	Rectifying Factor for 0.5V to -0.5V	Current Density at -0.1V (mA/cm^2)
n-PbSe/ p-Ge	270µm × 270µm	4.03×10^3	0.766	2,609	1.9

J-V analysis of the n-PbSe/p-Ge heterostructure reveals a high resistance reverse bias p-n junction formation with a low reverse bias current density of only 1.9mA cm-2 under -100mV reverse bias. Such strong p-n heterojunction behavior utilizing the MWIR PbSe absorber with SWIR Ge absorber could find great success in MWIR and SWIR photodetector applications, with easy integration into two-color detector systems[16]. While the current J-V statistics is attributed to the n-PbSe/p-Ge heterojunction, further investigations will be performed to determine the possible influence the Se treated interface has on the overall carrier flow behavior. Future work will include more in-depth analysis on the properties and role the interface has on the resulting heterogeneous

structure, and may help illuminate underlying mechanisms at play, aiding in the optimization and control of this n-PbSe/p-Ge heterostructure for device applications.

5. Enhancement of PbSe Epitaxial Thin-Films on Silicon Substrates

I. Introduction

Integration of MWIR absorbing PbSe films on the silicon platform has been a longstanding goal of researchers seeking to push the MWIR optoelectronic application opportunities to higher yields suitable for commercial industries. Over the years, researchers have explored many different techniques for improving lead selenide film quality on silicon substrates, exploring the application of various buffer layers, multi-stage growths, and post-growth treatment conditions[47], [70]–[73]. However, researchers have yet to reduce the defect density of epitaxial lead selenide films on silicon low enough to be competitive with other state-of-the-art MWIR material systems such as MCT. Currently, the best method for producing high-quality single crystalline lead selenide films on silicon is to use a calcium fluoride buffer layer combined with a post-growth annealing process to reduce the intrinsic defect level through diffusion and annihilation of defects via lead selenide's native defect slip system. The $9x10^5$ cm^{-2} EPD, the lowest reported value, was achieved by our group here at the University of Oklahoma by growing PbSe on a patterned Si substrate[74], [75]. However, these methods still fall short of other competitive MWIR material systems such as MCT, with a defect density roughly an order of magnitude larger, resulting in a Shockley-Read-Hall (SRH) limited device performance. Further, the current growth methodology of epitaxial lead selenide films on silicon shows obvious signs of inefficiencies regarding favorable growth mechanisms, with the presence of observable growth pits and anti-phase defects present on the film's as-grown surface. These disruptions to the otherwise atomically smooth PbSe surface are

often used to identify the efficacy of a system's growth conditions and environment for producing high-quality films. For the case of epitaxial PbSe films grown on silicon substrates, surface features such as growth pits and anti-phase defects can range on the order of 10^3-10^5 cm^{-2} depending on the quality of the growth[76], [77]. Analysis of these surface defects combined with etch pit revealing, gives researchers direct insight into the quality of their deposited films, where PbSe still finds its struggles when grown epitaxially on silicon for commercial MWIR optoelectronic applications.

Discussed here are the initial results of our efforts in expanding upon the current state-of-the-art growth methodology for MBE grown epitaxial PbSe films on Si(111) substrates. By introducing a periodic stepped growth surface during the nucleation of PbSe adatoms deposited on vicinal Si(111) 6° (100) substrates, we observe a drastic reduction in as-grown surface defects, along with reduced etch pit densities, making this technique a promising method for producing high-quality epitaxial PbSe films on silicon substrates not limited by Shockley-Read-Hall effects. Such films would find numerous applications in MWIR optoelectronic devices, with the ability to fabricate high performance and high-yield throughput PbSe-based platforms directly integrated onto silicon.

II. Experimental Details

Growth of Lead selenide thin films were performed in a custom multi-growth chamber molecular beam epitaxy system. Lead selenide films were deposited on 3-inch Si (111) 6° (100) substrates using a 99.9999%-pure Se-rich compound PbSe effusion source with a separate 99.9999%-pure Se effusion source. The PbSe:Se beam flux ratio was held at 10:1 to discourage selenium desorption from the film. Double-side polished vicinal Si wafers were cleaned using a modified Shiraki cleaning recipe followed by a thermal cleaning process at 850°C inside the MBE

fluoride growth chamber. After thermal cleaning, the substrate temperature was reduced to 780°C, and a 99.999% pure calcium fluoride effusion source was used to grow a 2nm thick buffer layer at a deposition rate of 0.1Å/s. After depositing the CaF_2 buffer layer, the sample was transferred in vacuum to the lead selenide growth chamber, where a 1.2μm thick PbSe film was subsequently grown at a substrate temperature of 380°C. In-situ reflection high-energy electron diffraction (RHEED) analysis was performed using the KSA 400 data acquisition and analysis software. Surface morphology was observed by scanning electron microscopy (SEM) and etch pit revealing was performed with a custom alkaline etching solution to expose PbSe defects.

III. Vicinal Surface and Nucleation

Periodic stepped surface conditions resulting from the large vicinal tilt of the Si (111) substrate surface orientation with a 6° tilt towards the (100) plane was purposefully introduced to encourage a modification of the Pb and Se adatom surface kinetics during nucleation. Recent studies have found that the impact of adatom surface diffusion and arrangement are heavily impacted by the presence of a high-density of atomic step edges, and have shown promise in improving heteroepitaxy film quality where large mismatches are observed[78]–[80]. While the current growth models for heteroepitaxy on nominal surfaces predict the nature of adatom-surface interactions and subsequent bulk growth quite well, the same equations which describe their dynamics in a given growth environment do not work well for films grown on a vicinal surface with greater than >1° of vicinal tilt. However, experimental evidence has shown a potentially favorable impact resulting from this modified growth surface, with the ability to form misfit accommodations steps resulting from the periodic step edges. Further, orientation preferred nucleation often results from the anisotropic surface energy influenced by the orientation dependent direction of the vicinal tilt, reducing the number of mismatched orientated grains which

may contribute to the formation of defects and anti-phase boundaries as overgrowth occurs and islands begin to coalesce.

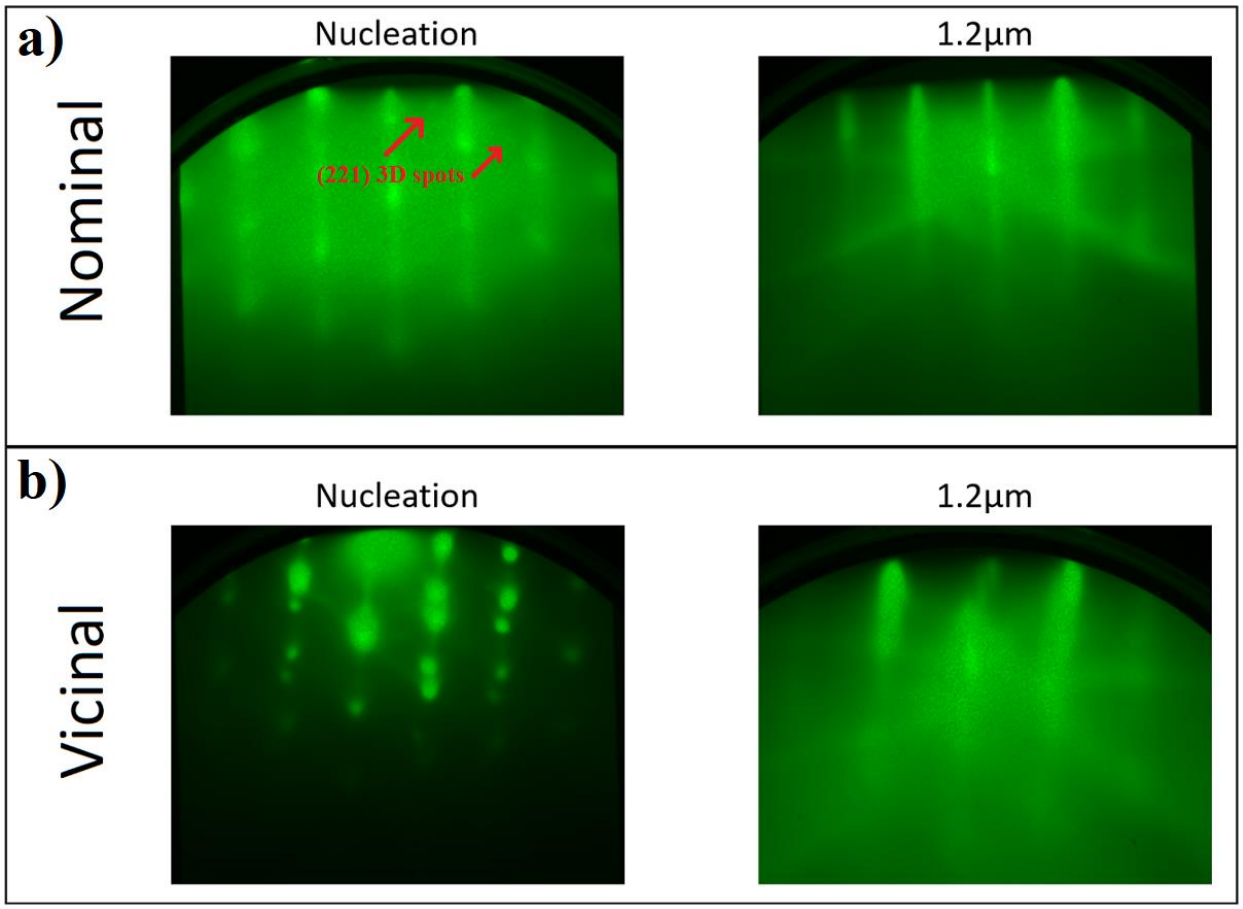

Figure 5.1 ***(110) RHEED of PbSe nucleation and 1.2µm bulk growth on CaF_2 buffer layer on silicon:*** *a) PbSe deposited on nominal Si(111) substrate with off-orientation RHEED spots, and b) PbSe deposited on vicinal Si(111) 6° (100).*

Figure 5.1 shows the in-situ RHEED observations of the nucleation and bulk 1.2µm thick epitaxial PbSe thin films on CaF_2 buffer layer on Si substrates. Immediately, one can observe by eye the vicinal nature present in RHEED images by way of the off-angle tilt of the RHEED pattern compared to growth on nominal silicon substrates. During the nucleation stage of the PbSe growth, an initial 3D island Vollmer-Weber growth mode dominates. As overgrowth continues, these 3D island either coalesce or become imbedded underneath a layer-by-layer Frank-Van der Merwe

growth of bulk PbSe, indicating a Stranki-Kranstanov growth mode, transitioning from 3D to 2D growth. While the RHEED evolution seems to proceed similarly for both the PbSe on nominal and PbSe on vicinal Si substrates, some critical information can be uncovered when observing the PbSe nucleation stage of growth. During this stage, PbSe proceeds in a 3D growth mode, with the presence of well orientated 3D growth sites. However, the PbSe films grown on nominal silicon substrates observe a small contribution of off-orientation islands, contributing to RHEED spots occurring at slightly different positions from the characteristic (110) PbSe RHEED pattern. Meanwhile, the PbSe nucleation on vicinal silicon did not see the same level of off-orientation island contribution. The nature of this observation implies that in both cases, where 3D island formation dominates during nucleation, the PbSe islands on vicinal silicon formed a higher degree of preferential orientation influenced by the seed crystal when compared to the growth on the nominal silicon substrate.

IV. Surface Morphology and Etch Pit Density

Scanning electron microscopy was used to characterize the as-grown surface features for PbSe films grown on vicinal silicon substrates versus those on nominal silicon. While the surface defects discussed previously are of particular interest, another aspect of the film's bulk surface morphology can help elucidate the growth environment's impact on lead selenide's developing growth mode. In previous experiments, where lead selenide films were grown on vicinal germanium substrates, an interesting effect on the film's surface morphology was the presence of a meandering ripple pattern on the film's surface parallel to the vicinal step edge direction[78]. This unique surface morphology indicated a step-meandering growth mode for PbSe films which

is common to observe when growing on such high miscut angles. However, for vicinal growth, the step-flow growth mode produces the highest quality films and is marked similarly to layer-by-layer growth on nominal substrates with an atomically smooth bulk surface, absent any rippling effects or Hillock 3D growth sites.

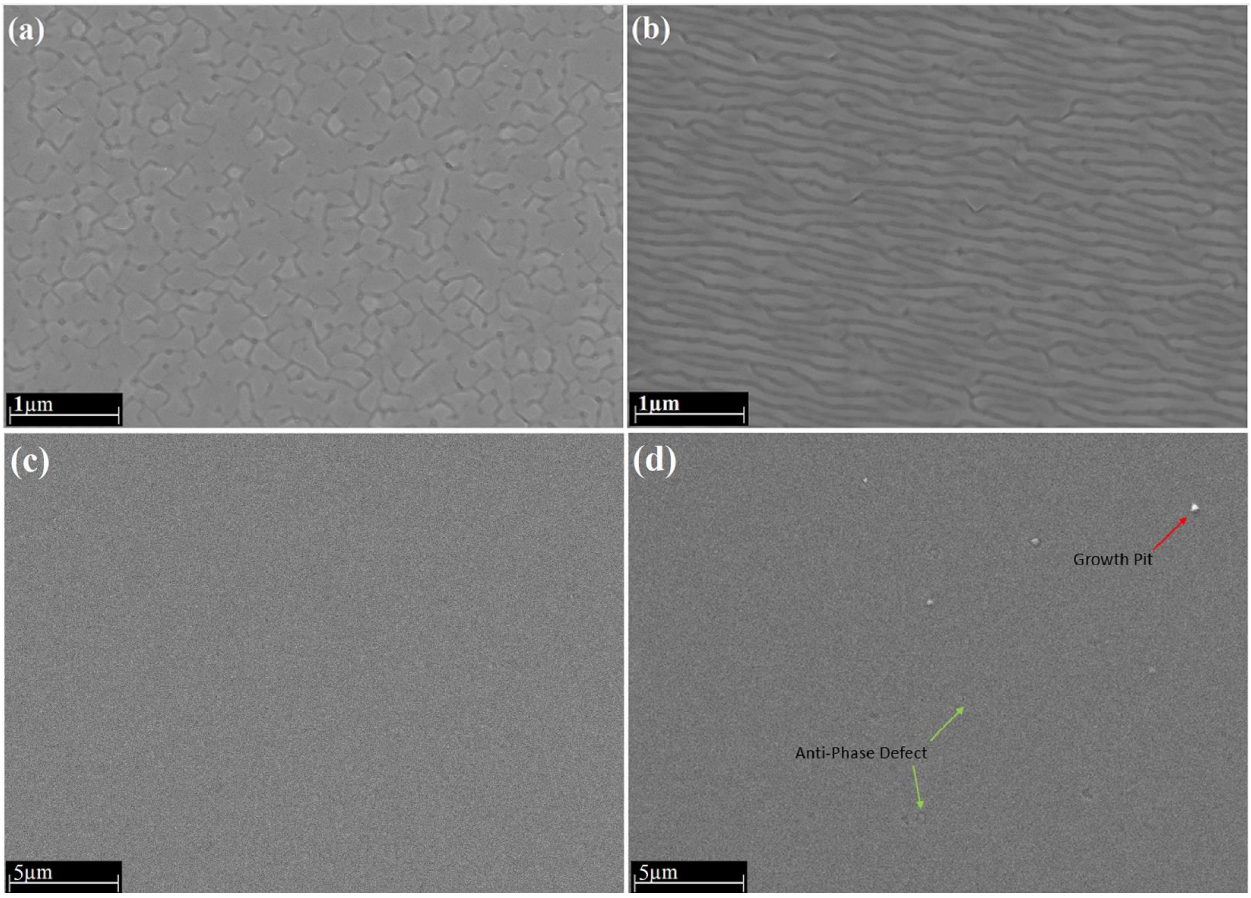

Figure 5.2 ***Top-down SEM images of PbSe films grown on:*** *(a) vicinal germanium substrate in Hillock's growth mode, (b) vicinal germanium substrate in step-meandering growth mode, (c) vicinal silicon substrate in step-flow growth mode, and (d) nominal silicon substrate in layer-by-layer growth mode.[78]*

In Figure 5.2(a-c), different growth modes can be observed for PbSe films grown on vicinal substrates as indicated by their surface morphology. In Figure 5.2(a), PbSe films grown on vicinal germanium substrates with insufficient surface treatment proceeded in a strained Hillock's growth mode. These films contain a high density of boundaries and imbedded grains within the bulk single crystalline PbSe film, resulting in poor material quality. Figure 5.2(b) presents the step-meandering

growth of PbSe films on vicinal germanium substrates as indicated by the meandering ripple pattern observed on the film's surface. In this case, sufficient changes to the surface kinetics from the substrate surface treatment process allow for higher adatom diffusion on the growth surface compared to previous Hillock's growth, resulting in layer-by-layer terrace growth, which can meander across multiple steps to form the ripple effect observed. While this growth mode produces higher quality epitaxial films than the Hillock's growth mode, the density of surface defects and anti-phase boundaries are elevated along the meandering step edges. In contrast, the work here on PbSe films grown on CaF_2 on Si(111) 6° (100) substrates, the PbSe films proceed under a step-flow growth mode. This is well indicated by the atomically smooth surface morphology observed in Figure 5.2(c), showing no signs of 3D Hillock growth sites or meandering atomic step edges or terraces. Further, when compared to the traditional growth of PbSe thin films on CaF_2 on nominal Si substrates, the PbSe surface morphology for the vicinal growth proceed entirely uninterrupted over large areas. In Figure 5.2(d), the atomically smooth PbSe film surface is disrupted by the protrusion of pyramidal growth pits and anti-phase boundaries. These surface disruptions have been well documented for PbSe thin films on CaF_2 on Si, and are an indication of an unoptimized growth environment, likely due to the mismatched strain allowing for the formation of a high density of mis-orientated grains and AB bonding pairs[67], [75]. The surface SEM image provided in Figure 5.2(c) is therefore a novel accomplishment in the heteroepitaxy of PbSe films, showcasing the lowest density of surface defect disruptions for epitaxial PbSe films grown on silicon. It is important to note that the pristine surface observed in Figure 5.2(c) is not limited to this singular imaged area, but is in fact the normal observed surface imaged across the majority of the 3-inch wafer, bringing the density of growth pits and anti-phase defects down to below 10 per cm^{-2}.

After observing the step-flow growth surface and lack of surface defect disruption in as-grown films, PbSe thin films grown on vicinal and nominal Si substrates were dipped in an etching solution to expose etch pit defect centers.

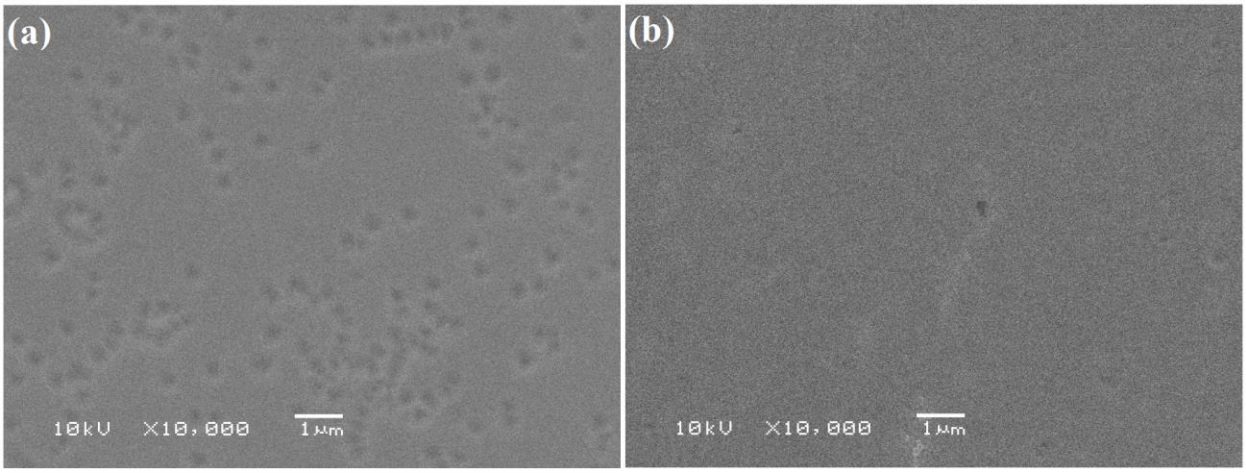

Figure 5.3 ***Top-down SEM images of etched PbSe films for:*** *(a) PbSe thin films grown on CaF_2 on nominal Si substrate, and (b) PbSe thin films grown on CaF_2 on vicinal Si substrate.*

Etch pit density revealing of the PbSe thin films on nominal and vicinal Si substrates shows an immediate contrast in defect density. For the growth of PbSe on the nominal Si substrate with a CaF_2 buffer layer, the calculated defect density observed in Figure 5.3(a) is roughly 5×10^7 cm^{-2}. This order of defect density is typical for as-grown epitaxial PbSe films grown on Si with the use of a CaF_2 buffer layer and is often required to undergo a post-growth thermal anneal to further reduce the defect density by up to an order of magnitude to approach state-of-the-art PbSe material quality on Si. However, the calculated as-grown defect density for the new PbSe deposition on vicinal Si substrates observed in Figure 5.3(b) showcases a record-breaking density of only 1.5×10^5 cm^{-2}. This drastic reduction in etch pit density, along with the removal of as-grown surface disruptions resulting from growth pits and anti-phase boundaries indicates a more favorable growth condition for mitigating the mismatch strain effects associated with the heteroepitaxy of PbSe thin films on Si than previously reported. The low etch pit density observed for the PbSe

films on vicinal Si have now approached the level of state-of-the-art MCT and T2SL Sb-based material systems, making this technology a potential candidate for high-performance MWIR optoelectronic device applications.

6. n-CdSe thin films on IV-VI PbSe for MWIR Photovoltaic Detector Applications

I. Introduction

Lead selenide has a long history in MWIR optoelectronic development, with more recent attention focused on the fabrication of MWIR detectors pushing beyond the cryogenic barrier. A major reason for the resurgence in popularity of PbSe-based MWIR detectors was the recent demonstration of a record-breaking room temperature MWIR detectivity (D*) of 4.2×10^{10} Jones by Prof. Shi's group at the University of Oklahoma[57]. The detector technology used in this groundbreaking demonstration was based on the photosensitized PbSe-based photoconductor detector technology. However, limitations in the fundamental design of this PbSe-based photoconductor detector impeded its usefulness in commercial applications due to the 1/f noise and inhomogeneous nature of its film properties and therefore its pixel-pixel performance. Since then, attention has shifted towards developing a PbSe-based photovoltaic detector structure which could overcome the challenges faced by its photoconductor counterpart while maintaining high D* performance. The attraction of the photovoltaic detector technology is its ability to suppress dark current and encourage optically generated carrier collection due to its built-in potential. Using the built-in potential, the photovoltaic detectors would not have to undergo the same post-growth sensitization process used in the PbSe-based photoconductor films, which rely on porous or high surface area polycrystalline films to allow for the photosensitization process to take hold, contributing to their high degree of inhomogeneity. The result of this effectively means that researchers can use more advanced deposition techniques such as molecular beam epitaxy (MBE)

to deposit films with atomically smooth surfaces and interfaces, and extremely homogenous electrical and optical properties, providing higher pixel-pixel performance ratios for fabrication of large-format focal plane arrays. In addition, 1/f noise in PbSe photovoltaic detector is significantly lower than its PC counterpart. Recently, II-VI/IV-VI heterostructures have been proposed as a viable candidate for MWIR photovoltaic detector applications. Initial demonstrations of thermally evaporated polycrystalline CdS thin films on PbSe were fabricated to produce the photovoltaic structure for MWIR detection. While the initial results from these experiments have shown great promise, issues with photogenerated carrier blocking and band alignment issues at lower operating temperatures have stunted their progress[3]. Here, we investigate the different routes in which a PV detector structure may be fabricated using II-VI n-CdSe films and IV-VI p-PbSe films. First, we demonstrate the fabrication of a polycrystalline n-CdSe on epitaxial p-PbSe PV detector structure and investigate its device behavior. Through our efforts, we subsequently find a new method for fabricating an all-epitaxial single-phase (cubic) n-CdSe/p-PbSe heterostructure and link its changes in detector behavior to its predecessors. The growth of a single phase (cubic-zincblende) epitaxial CdSe thin-film on single crystalline PbSe has never been previously reported, and its demonstration here showcases its potential for future design of enhanced MWIR PbSe-based photovoltaic detectors.

II. Experimental Methods

Formation of Polycrystalline CdSe on PbSe

Polycrystalline n-CdSe films were deposited by thermal evaporation using a 99.99% pure CdSe source material at a background pressure of 2×10^{-6} Torr and a substrate temperature of 200°C. the

n-CdSe films were deposited at a growth rate of 10nm per minute to a total desired thickness of 300nm. The p-PbSe deposition was carried out by molecular beam epitaxy on a double polished high resistant Si wafer which was cleaned using a modified Shiraki cleaning method followed by an in-situ thermal cleaning process at 850°C. Subsequently, a 2nm thick CaF_2 buffer layer was deposited at a substrate temperature of 800°C. The 1.2μm thick PbSe films were then grown at a lower substrate temperature of 390°C with an additional Se flux to control the p-type carrier concentration.

Epitaxial Heterojunction Growth

The epitaxial n-CdSe/p-PbSe heterostructure was deposited by MBE on freshly cleaved BaF_2 (111) substrates with a background pressure of 1×10^{-8} Torr. BaF_2 substrates were used for their excellent long-wave optical transmittance and similar crystal structure with PbSe, enabling epitaxial growth and subsequent back-side illumination detector design for device testing. PbSe thin films were deposited by direct evaporation of a 99.9999% pure 0.1% Se-rich compound PbSe effusion source in combination with a 99.999% pure elemental Se effusion source to achieve a p-type carrier concentration of $2\times10^{17}cm^{-3}$. Epitaxial CdSe thin films were then deposited using a 99.999% CdSe compound effusion source in combination with a 99.999% pure Bi_2Se_3 effusion source to encourage n-type doping.

Polycrystalline n-CdSe/p-PbSe Measurement and Device Testing

The room temperature dark current density versus voltage (J–V) characteristic of the heterojunction device was performed by using Keithley 2400 source meter in the bias range from −1 to 1 V. The detector performance was then evaluated by a homemade detectivity measurement system. In this system, a calibrated 800 K blackbody from Infrared System Development was used

as the standard infrared light source. A Thorlabs MC1F10 mechanical chopper was integrated to provide a frequency modulated heat source. The heterojunction diode was operated in photovoltaic mode with zero applied bias during the measurement. Without connecting to any preamplifier, signal and noise currents from the device were directly collected by a Stanford Research System SR830 lock-in amplifier.

Epitaxial n-CdSe/p-PbSe Measurement and Device Testing

In-situ RHEED monitoring of the growth evolution was captured and analyzed using the KSA 400 data acquisition and analysis software tool. Scanning electron microscopy (SEM) combined with x-ray diffraction (XRD) were used to corroborate the RHEED observations and examine the surface morphology and crystallography of the epitaxial CdSe thin-films on PbSe. A backside illumination detector structure was fabricated by lithographic process involving etching of CdSe mesa using a 3:1:1 mixture of 35% HCl acid, 85% phosphoric acid, and DI water for 20sec. Se washing was necessary immediately following the CdSe etching to remove the deposited selenium residue from the sample surface. This process consists of 98 wt% H_2SO_4 + 30 wt% H_2O_2 in a 3:1 volume to volume ratio.

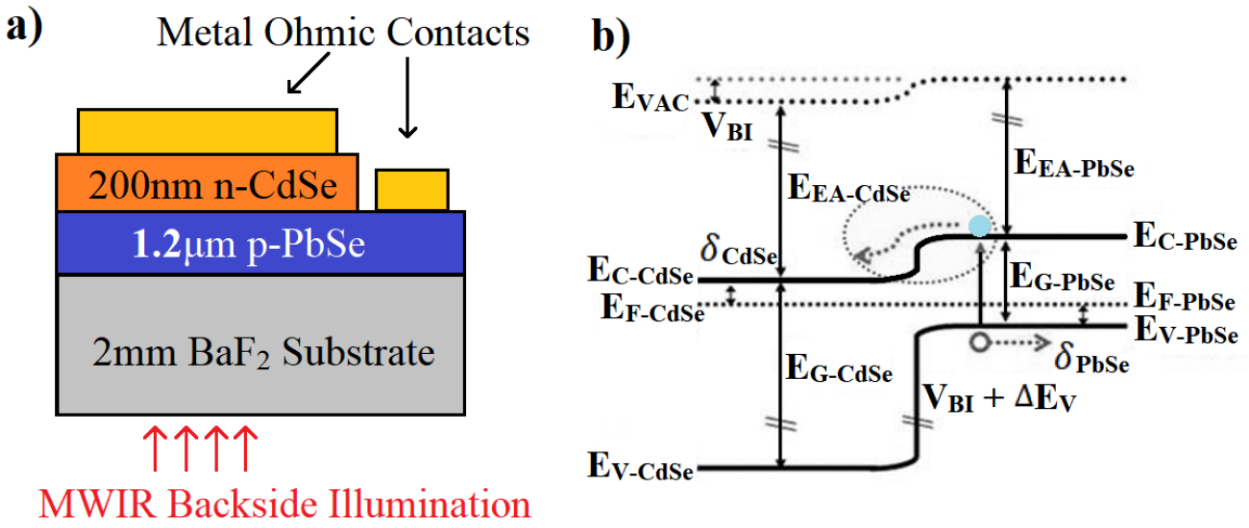

Figure 6.1 ***a) Configuration schematic of the n-CdSe/p-PbSe heterojunction mid-IR photodiode, and b) suggested energy band diagram of the n-CdSe/p-PbSe heterostructure.***

After forming the mesa structure, thermal deposition and lift-off of gold contacts were performed, and the sample was wire bonded for current-voltage analysis and radiometric measurements. The proposed band structure diagram in Figure 6.1(b) predicts a type-II heterojunction formation between an n-doped CdSe epitaxial thin film with a p-PbSe layer. Current-voltage measurements were performed using a Keithley 2400 source meter instrument with GPIB interface combined with the IV KickStart analysis software tool.

III. Results and Discussion

Polycrystalline n-CdSe/p-PbSe PV Heterostructure Route

Initial investigations of cadmium selenide films on PbSe were explored by thermal evaporation of n-CdSe films on epitaxial p-PbSe thin-films. Similar to the studies our group performed on CdS/PbSe heterostructures, the successful formation of a type-II band alignment between CdSe and PbSe resulted in strong rectifying behavior and subsequently demonstrated promising MWIR PV detector performance. Deposition of poly-CdSe films were performed on both as-grown epitaxial PbSe films and epitaxial PbSe films treated by a new high-temperature chloride passivation (HTCP) treatment method in effort to showcase enhanced device performance through the passivation of defect centers in the PbSe film.

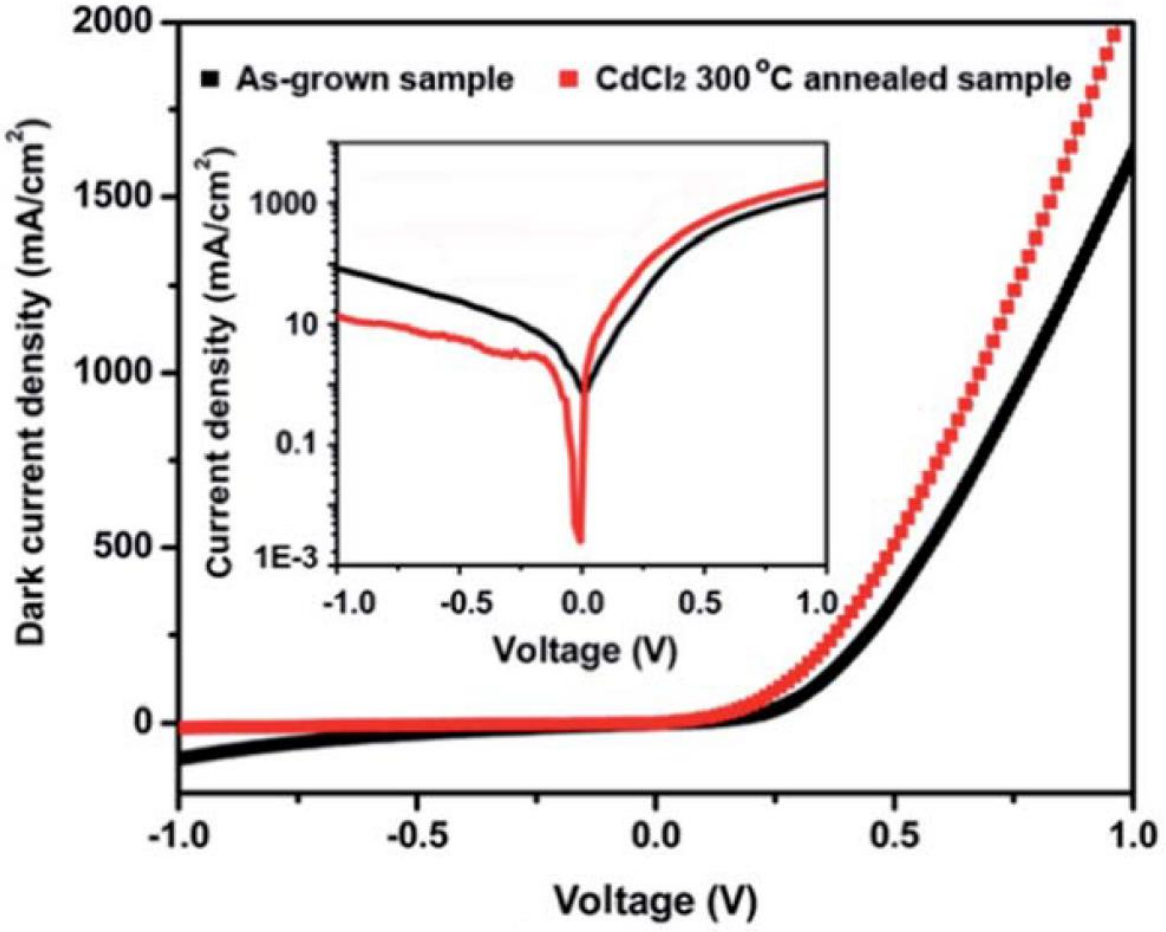

Figure 6.2 ***Room-temperature dark current density-voltage (J-V) characteristics of poly-CdSe/PbSe PV detectors with and without HTCP treatment.***

Figure 6.2 showcases the successful formation of a rectifying p-n heterojunction structure between poly-CdSe/PbSe, with a noticeable reduction in the reverse bias current density for the HTCP treated PbSe films. The room-temperature current density at 100mV reverse bias for the poly-CdSe/PbSe p-n heterojunction structure was 11.2mA/cm^2 and 3.5mA/cm^2 for the as-grown and HTCP PV detectors respectively. Further, improvement of the rectifying factor for the HTCP treated PV detector structure can be observed in Figure 6.2, with an increase from 16.2 to 306 rectifying factor when comparing the current density at 1V and -1V for the as-grown and HTCP treated samples respectively.

Subsequently, radiometric measurements were performed on both the HTCP and as-grown CdSe/PbSe material systems, observing promising room temperature PV detector performance.

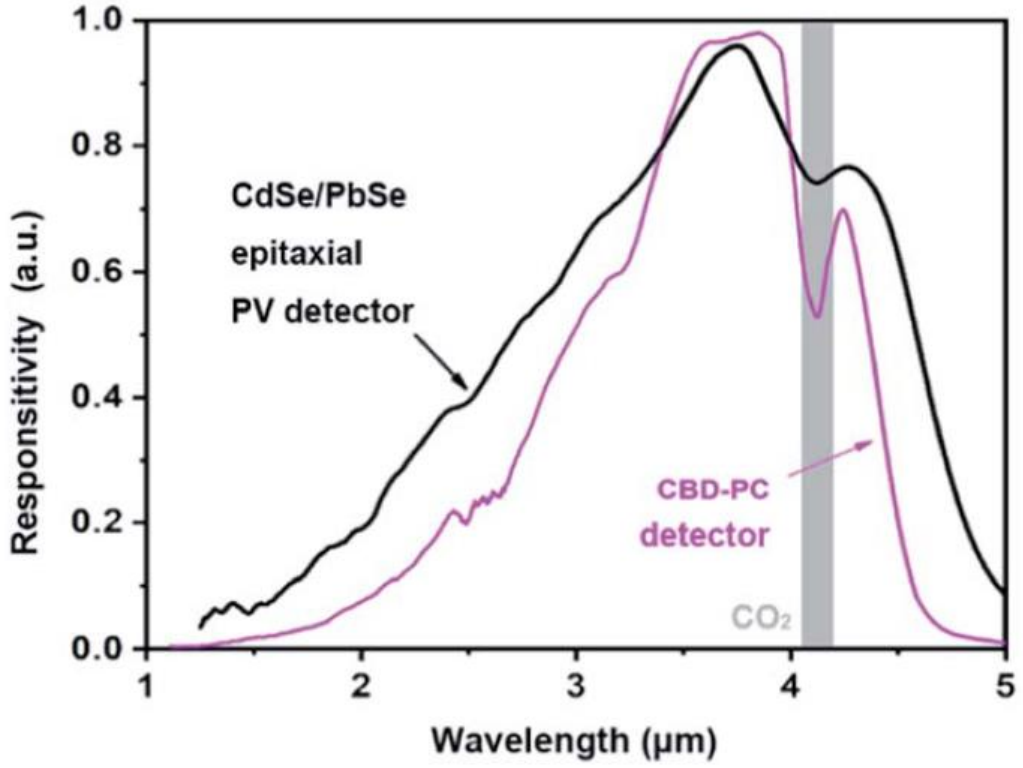

Figure 6.3 ***Comparison of the room-temperature spectral responsivity curves of the poly-CdSe/PbSe PV detector structure and the CBD-PbSe photoconductive detectors.***

The relative response curve of the poly-CdSe/PbSe PV detector ranges from 1-5μm, with peak responsivity around 3.8μm and a cut-off wavelength of 4.6μm. This structure showcases an extended cut-off compared to the CBD-PbSe photoconductors, which typically observes a cut-off wavelength around 4.4μm. Detectivity measurements for this structure resulted in promising room-temperature performances, with a measured D* of 2.5×10^{8} cm $Hz^{1/2}$ W^{-1} and 8.5×10^{8} cm $Hz^{1/2}$ W^{-1} for the as-grown and HTCP treated CdSe/PbSe PV detectors respectively. Further, our group also investigated the integration of this technology with a new MWIR transparent contact layer formed by a CdSe:In film. The application of this CdSe:In MWIR transparent conductive

layer produced a more efficient detector design, resulting in higher external quantum efficiencies and a further enhanced room-temperature D* of 1.02×10^{9} cm $Hz^{1/2}$ W^{-1} [81]. However, investigations by our group into the temperature dependent performance of these devices again showed abnormal behavior at lower temperatures similar to the CdS/PbSe PV detectors. Below 250K, the responsivity of the detector begins to plateau, limiting detector performance at TE-cooled temperatures. This phenomenon has been hypothesized to occur due to the positive temperature coefficient of PbSe, where the PbSe bandgap decreases with decreasing temperature rather than increasing as most other materials. This effect could potentially introduce a barrier below a certain temperature when the PbSe conduction band falls below the conduction band of CdSe. However, another mechanism which could contribute to this phenomenon is the presence of multi-phase CdSe grains in the polycrystalline film. In the presented work, the presence of both cubic-CdSe grains and hexagonal-CdSe grains contribute to the overall composition of the polycrystalline CdSe films on PbSe. This has been well documented by our group and other researchers by XRD measurements of CdSe/PbSe heterostructures [81], [82]. The introduction of wider bandgap hexagonal-CdSe grains can potentially increase the chance of forming a type-I band alignment with PbSe, especially at lower temperatures, resulting in the blocking of optically generated carriers. For this reason, our group decided to investigate new methods for fabricating an all-epitaxial single-phase (cubic) CdSe/PbSe heterojunction to promote a higher quality interface and remove potential barriers resulting from the hexagonal-CdSe grains.

Crystallography and Surface Morphology of Epitaxial CdSe films on PbSe

In-situ RHEED measurements were performed during the MBE deposition of lead selenide and cadmium selenide epitaxial films on barium fluoride substrates. Special interest was focused on

the nucleation and growth evolution of CdSe thin films on PbSe, since the single phase (cubic) epitaxial growth of CdSe on the IV-VI rocksalt crystal structure has never been reported.

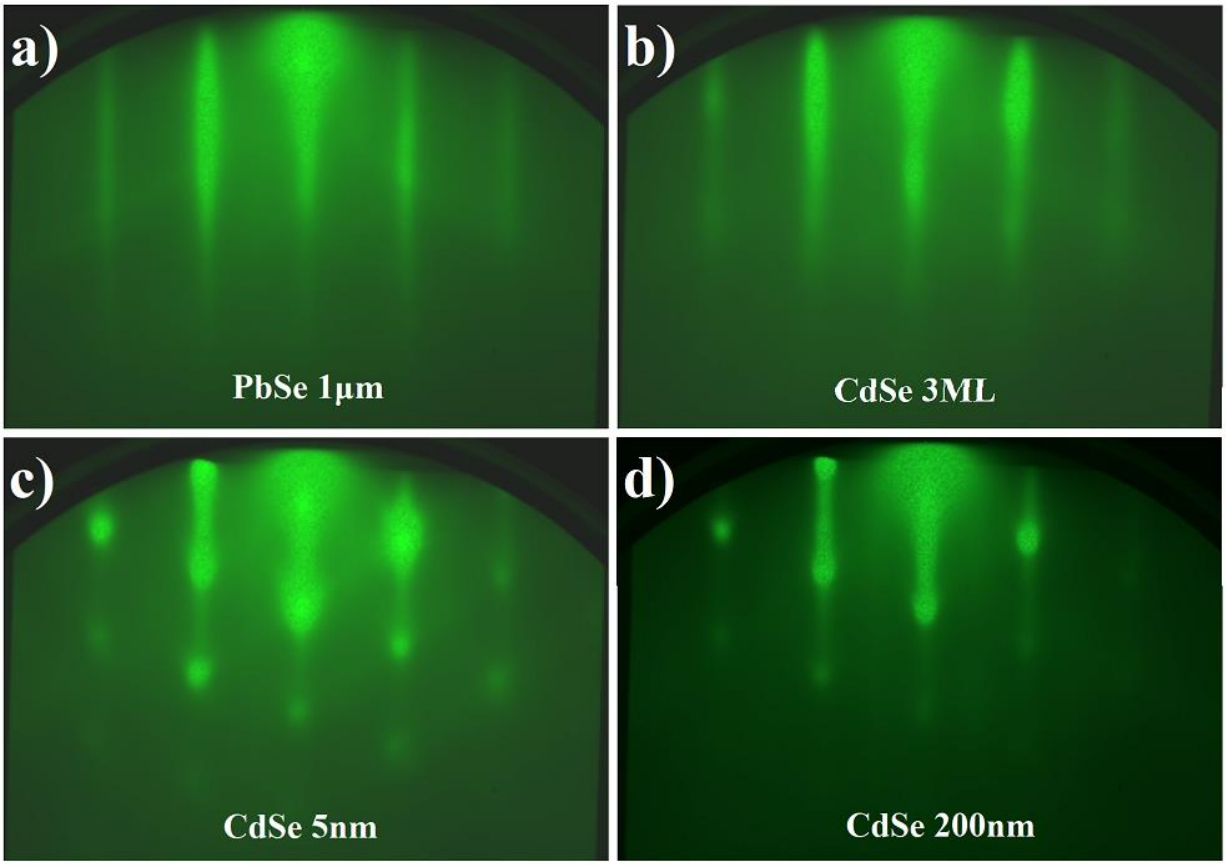

Figure 6.4 ***In-Situ RHEED measurements of the characteristic [110] orientation for:*** *a) 1µm thick PbSe film on BaF_2, b) 3ML nucleation of CdSe on PbSe, c) 5nm of CdSe, and final 200nm bulk CdSe thin film.*

Observing Figure 6.4 the nucleation of CdSe shows a strong correlation with the growth surface, matching the structure and orientation of the PbSe seed layer while proceeding in a layer-by-layer growth mode. After the initial deposition accumulation exceeds 5nm, RHEED observations begin to show signs of roughening, with the formation of 3D spots along the [110] direction. The rest of the bulk 200nm thick CdSe growth proceeds virtually unchanged, with no noticeable contributions from varying CdSe crystallites, such as off-orientation cubic CdSe grains or formation of a secondary phase of wurtzite CdSe. Interestingly, line profile analysis of the CdSe RHEED images

shows an identical diffraction spacing between the [110] CdSe and the [110] PbSe fringes. This indicates that epitaxial growth of CdSe maintained roughly the same lattice parameter as PbSe during the bulk of the 200nm thin film growth. Only during the last few nanometers of thickness did the line spacing begin to increase, indicating a decrease in the lattice parameter. While PbSe has a relaxed lattice constant of 6.12Å, literature indicates an expected lattice constant of 6.08Å for cubic CdSe. However, here we observe a slightly larger lattice parameter for the bulk CdSe film deposition closer to the 6.12Å of PbSe. This phenomenon is further investigated in the following XRD measurement and analysis of the as-grown heterostructure.

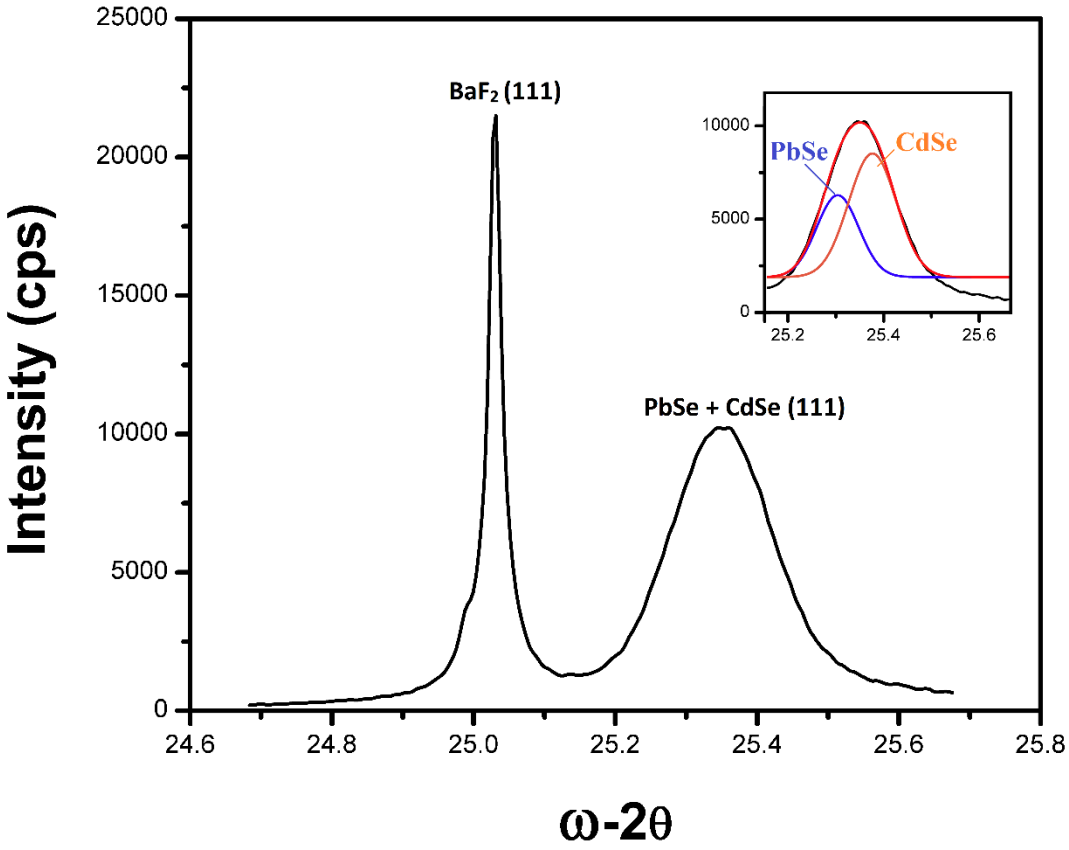

Figure 6.5 ***XRD measurement of the epitaxial n-CdSe/p-PbSe heterostructure on BaF_2 (111) substrate.***

High resolution x-ray diffraction measurements were taken of the as-grown CdSe/PbSe heterostructure on BaF_2. XRD scans of the main (111) substrate and layer peaks for PbSe and CdSe show a striking overlap of their diffraction peak contributions, as was expected from the RHEED investigation. The inset image in Figure 6.5 shows the deconvoluted peak contributions from the PbSe and CdSe layers, with a PbSe (111) peak position of 25.30° and a CdSe peak position of 25.38°. No off-orientation peak contributions were observed for either PbSe or CdSe, and neither were there any contributions from wurtzite CdSe, with characteristic peak positions at 23.4°, 24.8°, 26.5°, and 38.4°. The observations here corroborate the in-situ RHEED measurements observed during the growth of CdSe on PbSe, indicating unambiguously the successful formation of a single phase (cubic) bulk epitaxial CdSe thin film deposited directly on PbSe.

Current-Voltage and Radiometric Measurements

Processing of a 30μm × 30μm pixel for I-V measurement was performed to investigate the potential p-n junction behavior between the epitaxial n-CdSe and p-PbSe films.

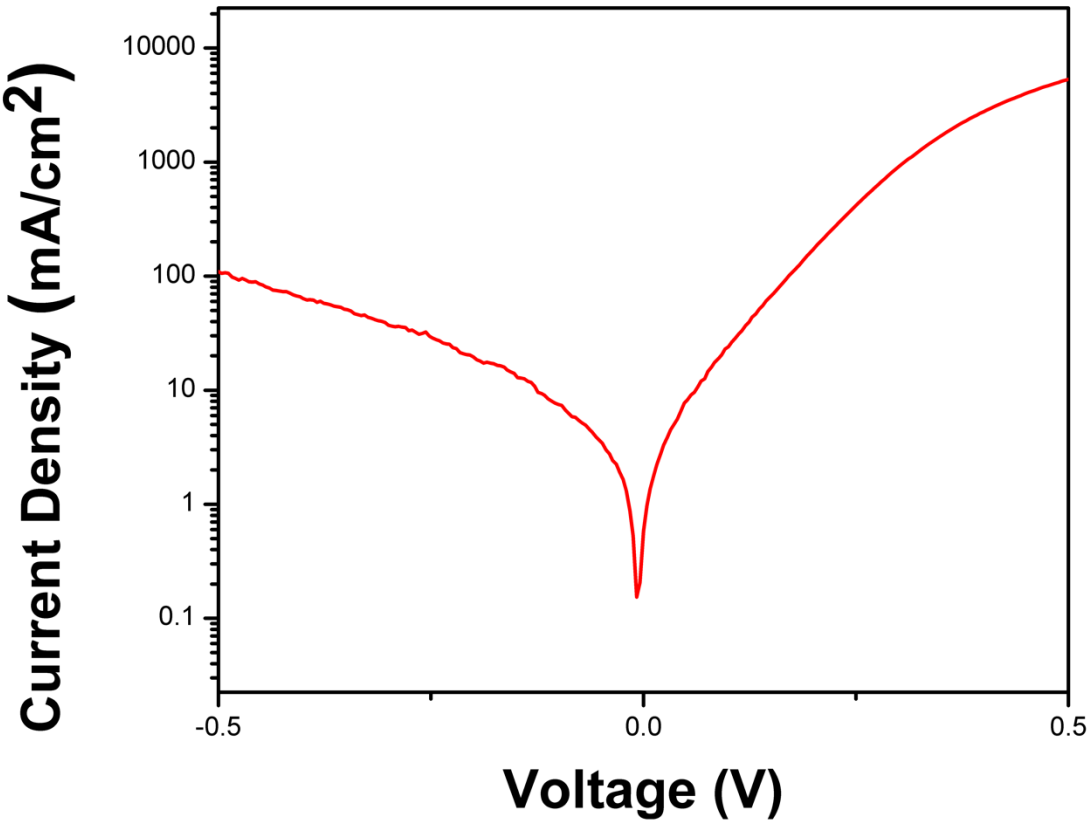

Figure 6.6 ***Room-temperature J-V characteristic of the epitaxial n-CdSe/p-PbSe heterojunction structure.***

Figure 6.6 shows the J-V statistics for the as-grown n-CdSe/p-PbSe heterojunction structure, demonstrating strong room-temperature p-n junction behavior similar to previous investigations on poly-CdSe/PbSe devices. Notably, a strong rectifying factor is observed indicating the formation of a barrier for the reverse bias current, with a rectifying factor of 50 when comparing the current density at 0.5V forward bias and reverse bias respectively. Subsequently, the reverse bias current density at -100mV is only 7.5mA/cm^2. While reports of similar levels of dark current density have been observed before in PbSe-based PV structures, the report here distinguishes itself

in that the low leakage current was observed for the as-grown material structure without any post-growth passivation treatments.

Temperature dependent radiometric measurements were performed from room temperature down to 230K to investigate the signal dampening phenomenon observed in our previous CdSe/PbSe efforts. The as-grown n-CdSe/p-PbSe structure displays a temperature dependent signal increase at lower temperatures while maintaining similar noise levels resulting in higher detectivities.

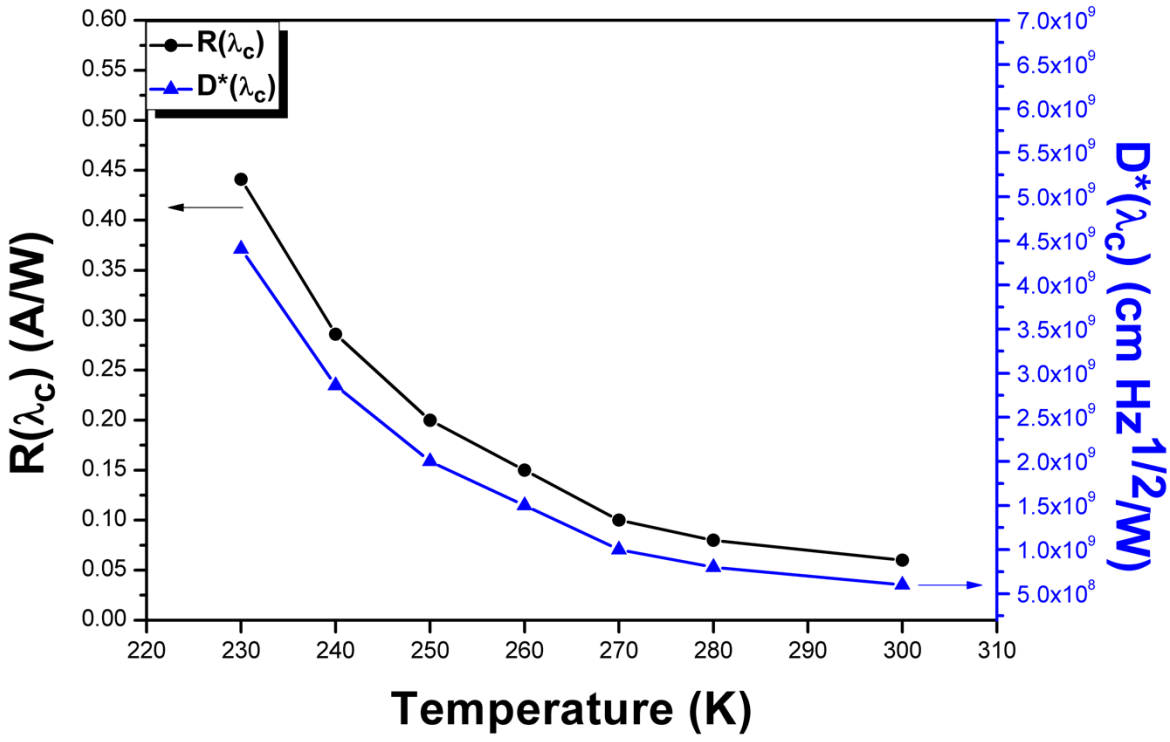

Figure 6.7 ***Temperature dependent peak Responsivity and D* measurements from 300K down to 230K under zero bias photovoltaic mode.***

Using a 500°C blackbody infrared source with a 750Hz chopping frequency, the room temperature 30μm × 30μm pixel achieved a peak responsivity of 0.06A/W and a D* of 6.5×10^{8}cm $Hz^{1/2}$ W^{-1} under zero bias photovoltaic operation. With decreasing temperature, the optical signal increased

by almost an order of magnitude as it approached 230K while maintaining a similar level of noise, achieving a responsivity of 0.441A/W and a D* of 4.4×10^{9}cm $Hz^{1/2}$ W^{-1} at 230K. The temperature dependent behavior observed in this new single phase epitaxial n-CdSe/p-PbSe heterojunction device sheds light on the inverted temperature dependent behavior phenomenon observed by the previous explorations of similar CdSe/PbSe PV detector structures. Here, this new epitaxial interface between cubic PbSe and CdSe films without any contributions from hexagonal-CdSe grains demonstrates the first example of the CdSe/PbSe PV detector structure continued increase in signal and detector performance all the way down to TE-cooled operating temperatures. Further, the as-grown detector performance of this new technology demonstrates an almost 3x D* increase at room temperature compared to the as-grown poly-CdSe/PbSe PV detector structure. Combined with the previous studies on device enhancement using post-growth treatment techniques and enhanced device structure design, this new epitaxial p-n heterojunction structure demonstrates a promising advancement in the fabrication of enhanced II-VI/IV-VI interfaces and heterojunctions, with the potential for developing new state-of-the-art MWIR photodetectors operating above cryogenic cooling temperatures.

7. Post-Growth Treatment of Oxygen Deficient Cadmium Oxide Thin-Films for MWIR Transparent Conductive Contacts

I. Introduction

The development of MWIR transparent conductive oxides (TCOs) is an attractive research effort due to their ability to enhance device performance of optoelectronic devices. This research is influenced by the high electrical conductivity and optical transparency exhibited by metal oxides such as Cadmium Oxide (CdO) [83]–[88], Indium Tin Oxide (ITO), Zinc Oxide (ZnO), and Fluorine doped Tin Oxide (FTO) [89]–[91]. Although research around the visible light spectrum has seen major progress in recent years, infrared regions extending beyond near infrared (NIR) have yet to experience comparable growth in the development of suitable TCO films. The successful fabrication of a low-cost transparent conductive material operating in the MWIR region would find numerous applications in devices such as thermal photovoltaics[92], hot carrier solar cells [93], photodetectors [94], and transparent electrodes [95]. More recently, research on metal nanowire networks [96], carbon nanotube and graphene-based films [97], were reported as promising candidates for MWIR TCMs. However, these approaches involve either discontinued nanostructures as a conducting medium resulting in air holes, or fragile films that are difficult and expensive to fabricate. BaCuSF [98], was reported as a promising p-type MWIR TCM, however, its conductivity still needs further improvement. The most exciting advancement recently was the demonstration of CdSe:In thin films as a MWIR transparent conductive electrode on a MWIR PbSe/CdSe photovoltaic detector structure by molecular beam epitaxy [81]. Among other material

systems, previous research efforts have indicated the potential for using CdO as a low-cost n-type TCO. The fabrication of CdO films is achievable through various deposition techniques, such as molecular beam epitaxy [88], spray pyrolysis [99], DC Magnetron sputtering [100], solution growth techniques [101], and activated reactive evaporation [102]. However, most of these studies have not focused on the optical properties extending to the MWIR region. In this paper, we demonstrate a slight variation to the traditional reactive magnetron sputtering techniques used to fabricate CdO films. Instead of using an oxygen partial pressure during growth to control oxygen vacancy levels in CdO films, our CdO films were deposited absent any oxygen partial pressure, creating purposefully oxygen deficient CdO films, but with more stable levels of oxygen vacancies between growths. Subsequently, various post growth annealing conditions of oxygen deficient CdO films were investigated, providing more enhanced control of Oxygen atom inclusion in CdO films needed for tailoring CdO optical and electrical properties. Investigation of optical transmittance was performed by FTIR, while Hall measurement, SEM, and x-ray diffraction were employed for optimizing and characterizing electrical and structural properties of CdO films.

II. Experimental Details

CdO films were deposited by a custom built 3-target DC magnetron sputtering system using a single two-inch CdO hot pressed disk target (Ceramic, 99.999%). The magnetron sputter system employed by our experiments utilizes a tilted target configuration with respect to the sample holder plane. For this reason, a large separation distance of 25cm from target to holder was needed to ensure homogeneous growth on the substrate. The growth chamber was initially pumped down to $1.0x10^{-6}$ mbar, with the inclusion of Argon sputtering gas, raising the pressure to 0.025mbar. The sputtering pressure throughout the growth process was maintained at 0.03 mbar for two hours at

100mA and 500V, giving a total power of 50W. This method differs from traditional sputtering techniques, which typically involve an oxygen supply to the growth chamber. Previous studies include the use of either a pure Cd target, or compound CdO target, in combination with an optimized oxygen partial pressure during deposition [22]–[26]. Reactive sputtering of CdO films typically report oxygen partial pressures of 0.001-0.005mbar [25], [26], with variation in partial pressure being used to control oxygen vacancy levels. However, this technique does not provide adequate control of oxygen vacancy levels needed for operation as a MWIR TCO. In this paper, we report the use of a single CdO target for depositing CdO films in vacuum to achieve more consistent oxygen vacancy levels between growths. In vacuum, the hot-pressed target of compound CdO will maintain stoichiometry with little change in oxygen deficiency levels during the sputtering process. Optimized post growth annealing conditions are then used to further enhance TCO properties through the filling of Oxygen vacancies. Our experiments found that post growth annealing of oxygen deficient CdO films provide a wider range of control of oxygen vacancy levels when compared to the reactive sputtering technique. Substrate selection for CdO films involved consideration of post growth characterization, which required accurate measurements of both electrical and optical properties. For this reason, CdO films were deposited on insulating Calcium Fluoride (CaF2) substrates, cleaved and polished along (111) orientation. Insulating CaF2 provides the ability to perform accurate Hall Effect measurements while also providing excellent optical transparency for wavelengths extending beyond NIR. This permits investigation of the full optical spectrum of CdO films. Some relevant material parameters of CdO films and the CaF2 substrate are listed in

Table 7.1.

Table 7.1 ***Material Properties of Cadmium Oxide and Calcium Fluoride***

Material	Lattice Constant (Å)	Refractive Index	Thermal Expansion Coefficient (K^{-1})	Crystal Structure
Cadmium Oxide	4.695	2.50	14.0×10^{-6}	Cubic
Calcium Fluoride	5.462	1.4338	17.0×10^{-6}	Cubic

The deposited CdO films were grown to a thickness of 500nm. CdO films from the same growth run were cut into 1x1cm samples to perform a wide variety post growth treatment and characterization.

III. Results and Discussion

SEM and X-Ray Analysis

Figure 7.1 provides the SEM surface and cross-sectional images of CdO films before and after annealing in oxygen. The cross-sectional SEM images reveal the highly directional polycrystalline nature of the CdO films, with grain widths ranging from 80-100nm. Comparing the top-down SEM images in Figure 7.1, grain size is observed to be relatively unchanged between as-grown CdO films and those annealed in oxygen. The vertical directionality of crystallites in the CdO film suggest the possibility for higher electron mobility along the vertical direction compared to the high number of boundary domains along the lateral direction.

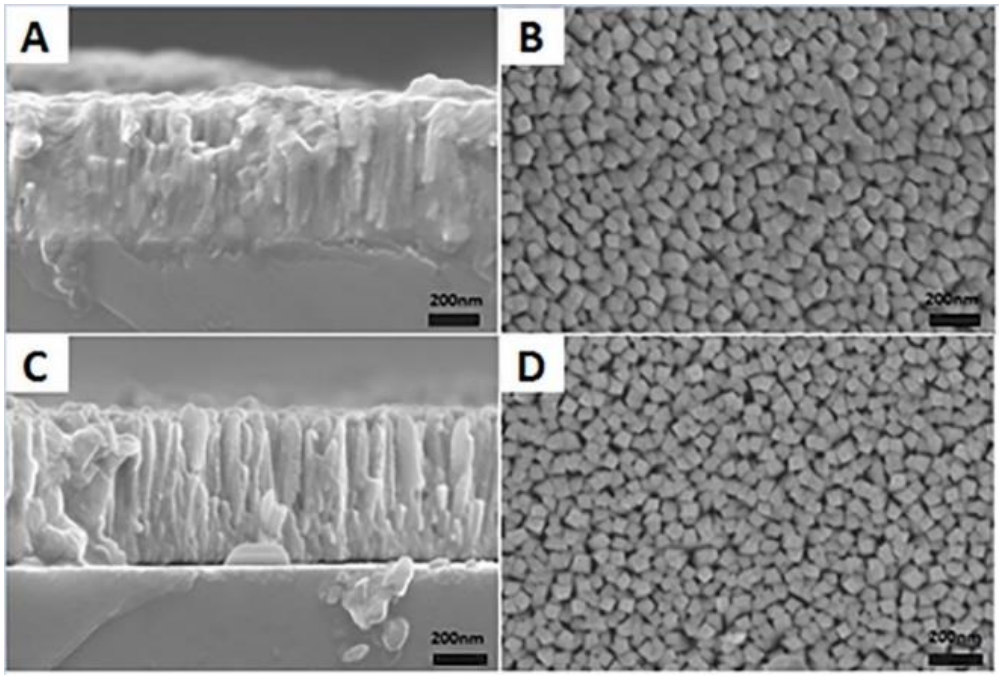

Figure 7.1 ***SEM images of CdO films for:*** *(a) Cross-sectional view of as-grown, (b) top view of as-grown, (c) cross-sectional view annealed film in oxygen, and (d) top view annealed film in oxygen.*

Energy dispersive x-ray (EDX) measurements were performed on both the as-grown and annealed CdO samples in effort to determine oxygen atom level incorporation. However, EDX measurements resulted in varying degrees of oxygen atom percentages between CdO films non-representative of expected oxygen atom to cadmium atom ratios. This is likely due to the high level of oxygen atom interstitials found in CdO films, resulting in values not correlative to oxygen vacancy levels responsible for changes in optoelectrical properties. Therefore, the relative difference in the filling of oxygen vacancies between CdO samples are inferred from measured optical and electrical changes from the as-grown film.

Powder X-ray diffraction (XRD) analyses were performed using a Rigaku Ultima IV diffractometer. Cu-K-alpha radiation (40 kV, 44 mA) was used in Bragg-Brentano mode with theta-compensating slits, curved graphite monochromator, and scintillation detector. Data analysis

was completed using MDI Jade2010 with the ICDD (International Centre for Diffraction Data) PDF4+ database[103].

In Figure 7.2, XRD measurements of both as-grown CdO films and oxygen annealed samples show the presence of a singular dominating (200) CdO diffraction peak, with a slight contribution from the (111) orientation, coinciding with the highly direction columnar structure observed in cross-sectional SEM. Although there have been previous reports of (200) oriented CdO films deposited at higher temperatures [86], [104], these reports indicate that typical room temperature CdO prefers (111) orientation. Compared with (111) oriented CdO films, previous studies reveal that CdO grains grown along the (200) plane exhibit lower surface energy due to higher planar density, resulting in better quality CdO films with higher electrical conductivity [104]. The ability to grow (200) CdO films at room temperature could be attributed to the different growth method used in our experiment and may also contribute to the promising TCO properties found in our CdO films after annealing.

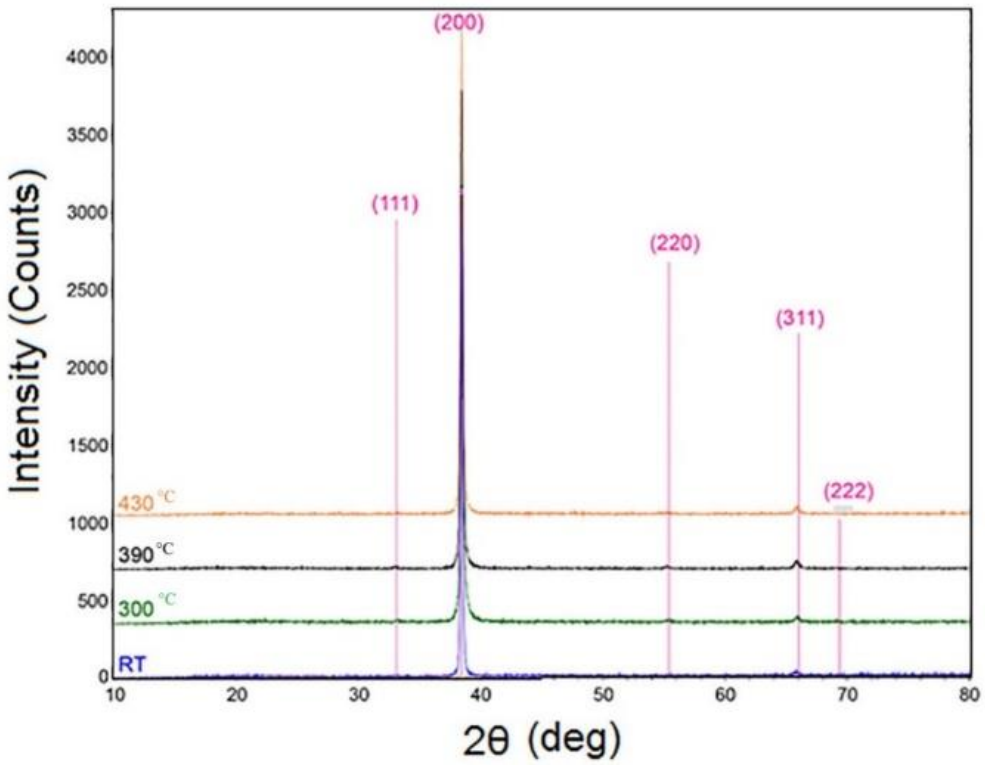

Figure 7.2 ***Stacked overlay of XRD patterns:*** *Expected peak positions for CdO are denoted by vertical lines.*

Electrical and Optical Properties

The importance of electron concentration arises from its relationship to the material's plasma frequency, which limits the optical transparency of incident light for longer wavelengths. The equation relating plasma frequency to carrier concentration is provided in SI units by the following.

$$\omega_{pe} = \sqrt{\frac{n_e e^2}{m^* \varepsilon_0}} \ldots\ldots\ldots 7.1$$

Where n_e is the carrier concentration, e is the charge of the carriers, m* is the effective mass of the carriers, and ε_o is the permittivity of free space. Equation (1) reveals that higher carrier concentrations will result in higher plasma frequencies. Therefore, to extend the optical transparency of CdO films into longer wavelength regimes, CdO films should exhibit the lowest

possible carrier concentration for optimum transparency while still maintaining a high level of conductivity through enhanced mobility. Previous studies have shown that carrier concentration in CdO films is dominated by oxygen vacancies in the CdO lattice structure [83]. However, the presence of oxygen vacancies in CdO films not only reduce cutoff wavelengths for optical transmission, but also contribute to low carrier mobility through vacancy defects in the CdO lattice structure. Rather than controlling the oxygen vacancy levels during growth, we demonstrate the viability of performing post growth annealing in a pure oxygen environment to promote the diffusion of oxygen atoms into the material system. In this process, competition between oxygen atoms diffusing into the CdO film, versus those escaping, results in either a net increase or decrease of oxygen vacancies. For this reason, optimization is needed to determine a suitable temperature range for post growth annealing. In our experiments, CdO films from the same sputtering run were cut into multiple 1x1cm samples and annealed in oxygen for various amounts of time and temperatures. These conditions ranged from 30 minutes to 2 hours, and 200°C to 430°C. After numerous trials, we found an annealing time of 45min was sufficient to produce noticeable changes in CdO film electrical and optical properties. Further, annealing temperatures below 300° resulted in little change, while above 400°C resulted in a reversal of change from the desired regime of interest. Table 7.2 shows the measured changes in electrical and optical properties of CdO films annealed in oxygen for 45min compared to the as-grown film.

Table 7.2 ***Cadmium Oxide Electrical and Optical Properties for Different Post-Growth Annealing Temperatures***

Annealing Temperature (^{o}c)	**Electron Concentration (cm^{-3})**	**Sheet Resistance (Ω/sq)**	**Optical Transmission @5 μm (%)**
As-Grown	8.1×10^{19}	50	0
300	5.9×10^{19}	70	22
370	4.5×10^{19}	54	30

390	3.3×10^{19}	44	51
410	5.2×10^{19}	45	35

Room temperature Hall Effect measurements were performed using the HEM-2000 Hall Effect Measurement System by EGK, which revealed interesting changes in electrical properties between as-grown and annealed samples. As-grown CdO films showed a Hall mobility of 30 $cm^2V^{-1}s^{-1}$, and an electron concentration of $8.1x10^{19}cm^{-3}$. The best sample produced by our experiments was annealed for 45 minutes at 390°C in oxygen, resulting in an enhanced Hall mobility of 84 $cm^2V^{-1}s^{-1}$ and a reduced electron concentration of 3.3x10^19 cm^{-3}. The electrical properties of this annealed sample are comparable to commercial ITO and FTO films, while FTIR measurements show an extension of the optical transparency well into the MWIR region as seen in Figure 7.3. The electrical and optical properties provided in Table 7.3 give insight into the comparison of commercial ITO and FTO films with our CdO sample.

Table 7.3 ***Comparison of MWIR TCO Tailored Cadmium Oxide's Electrical and Optical Properties with Commercial ITO and FTO.***

Material	Mobility (cm^2/Vs)	Sheet Resistance (Ω/sq)	Optical Transmission Cut-Off below 50% (μm)
CdO	84	43	5
FTO	40	15	1.5
ITO	40	10	1.5

Optical transmission of CdO films were measured using a Bruker Instrument Fourier Transform Infrared (FTIR) Spectroscopy, covering the full spectral range from absorption edge to plasma cutoff. For the visible range, a Si detector element was used, while DTGS was used for

measurements extending into the infrared region. Figure 7.3 shows the combination of these two measurements forming the full optical transmission spectrum for the CdO film treated at 390°C. Although there have been previous investigations into the optical properties of CdO films [86], [104], [105], these reports do not extend beyond NIR to include the full optical spectrum. The full transmission window of the CdO film annealed at 390°c is presented in Figure 7.3a, along with a comparison of MWIR transmittance for as-grown and annealed samples in Figure 7.3b.

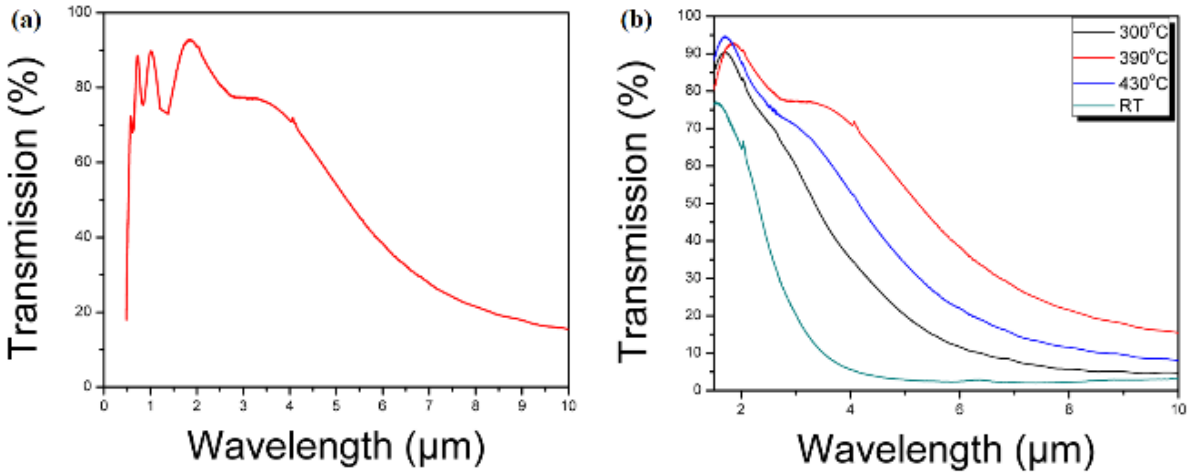

Figure 7.3 ***(a) Full optical transmission curve of CdO annealed at 390°c in oxygen, and (b) MWIR transmission of as-grown and annealed samples.***

Figure 7.3b highlights the effect post-growth treatment has on CdO optical properties. Compared to the as-grown CdO film deposited at room temperature, the samples annealed in oxygen showed a major increase in the cut-off wavelength extending into the MWIR regime. Beyond 400°c, the cut-off wavelength starts to blue shift again to lower wavelengths, indicating a turning point in which the filling of oxygen vacancies is becoming less efficient, likely due to the high thermal energy encouraging oxygen desorption away from the film. Further, the extension of the optical transmittance window to longer wavelengths is dominated by the change in slope of the cut-off edge as seen in Figure 7.3b. This implies a non-uniform plasma frequency in the annealed CdO

films, which translates to a non-uniform, or depth dependent carrier concentration. This may be attributed to the nature in which oxygen atoms are introduced to the CdO films, where the diffusion process during annealing results in a graded profile for filling of oxygen vacancies. This effect results in a difference in number of filled vacancies with varying depth, where layers closer to the film surface experience higher oxygen atom interaction versus layers deeper in the film. The expected profile here would be a CdO film with lower carrier concentration near the film surface, and an increasing concentration approaching to the as-grown bulk near the substrate/film interface. While Hall Effect measurements observed a decrease in carrier concentration for the annealed CdO films, the magnitude of this decrease only relates the average concentration of the bulk CdO films. It may be that the difference in carrier concentration is even larger than measured when comparing shallow depth CdO layers of annealed samples versus the as-grown film.

The optical bandgap of CdO is determined by the following equation [106],

$$\alpha_{direct} = \frac{A}{(h\nu)^{1/2}}(h\nu - E_g)^{1/2} \ldots\ldots\ldots\ldots 7.2$$

Where α_{direct} is the absorption coefficient, A is a constant, $h\nu$ is the photon energy, and E_g is the band gap energy. Observing the relationship between E_g and α_{direct} in equation 2, and plotting the linear relationship of α^2 versus photon energy, the band gap energy E_g can be found when $\alpha^2 = 0$. Figure 7.4 depicts this relationship, and shows that our CdO film results in an optical bandgap of $E_g = 2.29\ eV$, which falls within reported ranges of CdO bandgap [107].

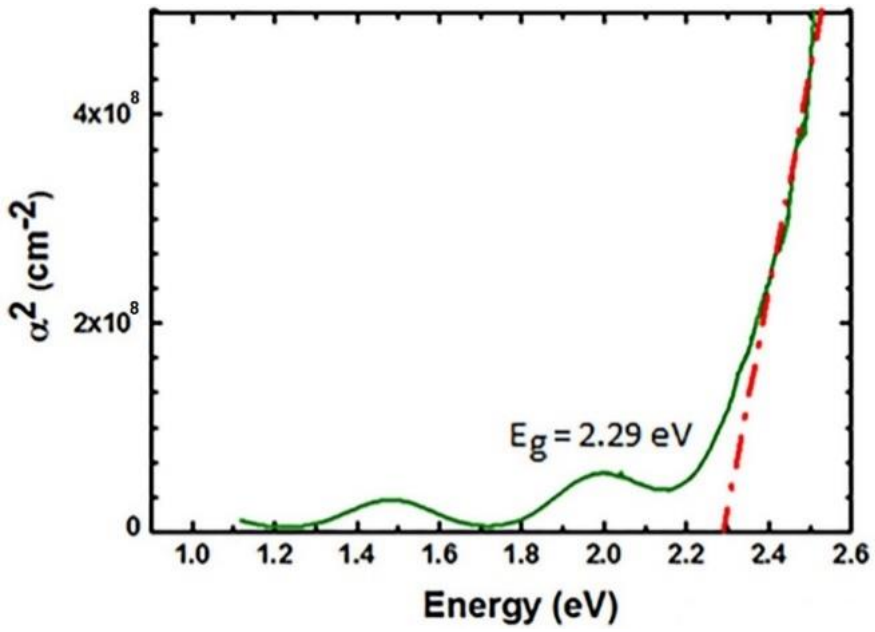

Figure 7.4 ***α^2 vs. Photon Energy for the CdO film treated at 390°C.***

Comparing the experimental optical transmittance results with simulation, we further investigate the optical properties of CdO films by the transfer-matrix method. For the investigated region of 1-9μm, the Drude model was used to describe the wavelength dependent refractive index of CdO. The contribution of impurity atoms on the refractive index of CdO was not considered due to the high purity target used during growth. For CaF_2, wavelength dependent refractive indices reported in reference [108] were used. For CdO, there are several parameters used in the Drude model, namely, the conductivity (σ), carrier concentration (n_e), charge mobility (μ), sheet resistance (R_s) and the complex refractive index ($\tilde{n}$). Where [109],

$\tilde{n} = n + i\,k = \sqrt{\tilde{\epsilon}}$ *7.3*

$\tilde{\epsilon}$ is the complex dielectric function for CdO which can be found using the free electron Drude model [83], [110], [111].

$\tilde{\epsilon} = \tilde{n}^2 = \epsilon_\infty - \frac{{\omega_p}^2}{\omega(\omega + i\,\gamma)}$ *7.4*

Here, ϵ_∞ is the high frequency dielectric constant (≈ 5.3 [2]or 5.5 [3] $for\ CdO$), ω_p is the plasma frequency, and γ is the damping factor describing the scattering and ohmic losses [86], [110].

$$\omega_p = \frac{n_e e^2}{m^* \epsilon_\infty \epsilon_0} \ldots\ldots\ldots\ 7.5$$

$$\gamma = \frac{e}{\mu m^*} \ldots\ldots\ldots 7.6$$

Where ϵ_0 and m^* are the permittivity of the free space and the electron's effective mass respectively. For our calculation, $m^* = 0.21\ m_e$ is used for CdO [85], [110].

Then, the reflectivity R of the CdO layer in terms of the dielectric constant with incident light perpendicular to the surface can be expressed as [83]:

$$R = \frac{|\sqrt{\epsilon}-1|^2}{|\sqrt{\epsilon}+1|^2} \ldots\ldots\ldots\ldots\ldots 7.7$$

Knowing reflectivity R and some of the above-mentioned parameters such as the sheet resistance R_s, and conductivityσ, the transmittance T can be calculated using the following formula [83],

$$\frac{\sigma}{\alpha} = [R_s\, ln(T+R)]^{-1} \ldots\ldots\ldots\ldots 7.8$$

Where α is the frequency dependent absorption coefficient, which is directly proportional to the extinction coefficient k [83]:

$$\alpha = \frac{4\pi k}{\lambda} = \frac{2k}{c}\omega \ldots\ldots\ldots\ldots 7.9$$

The resultant simulation utilizing these equations gives a peak optical transmittance of 88.6%, which is slightly higher than our experimental result of 87.3%. This small difference may be attributed to scattering losses, or other loss mechanisms. Simulation of the optical transmission of CdO films using recorded parameters from Hall Effect measurement data and reported values of ϵ_∞ = 5.3, and $m*$ = 0.21 m_e, results in the following Figure 7.5a. Table 7.4 provides the experimental and fitting parameters used in Figure 7.5.

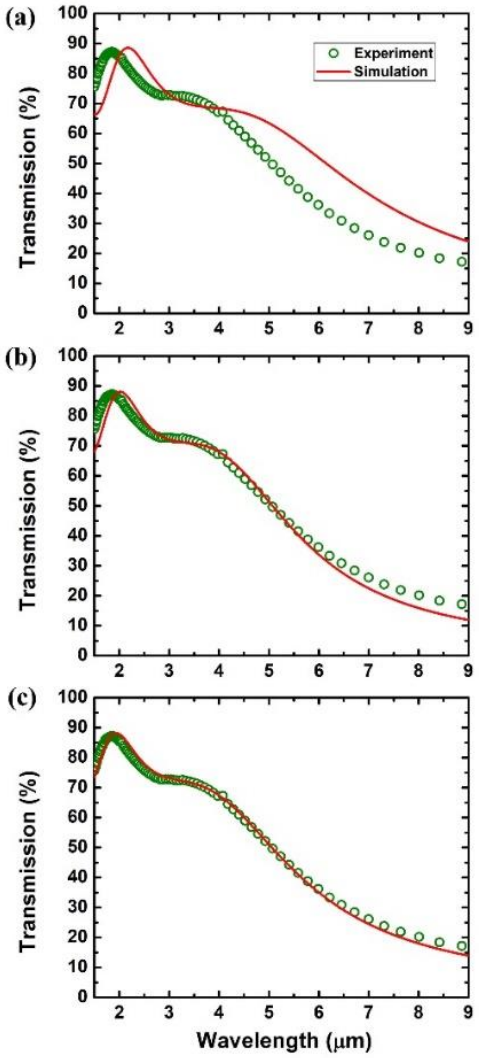

Figure 7.5 ***Comparison of experimental vs. simulated optical transmission curves:*** *(a) without fitting parameters, (b) fitting carrier concentration and mobility, and (c) fitting carrier concentration, mobility, and high frequency dielectric constant for the 390°c treated sample.*

Table 7.4 ***Fitting parameters for CdO simulation curves.***

Simulated Transmission Curve	Carrier Concentration $10^{19}(cm^{-3})$	Mobility (cm^2/Vs)	ϵ_∞
Figure 7.5a	3.3	84.2	5.3
Figure 7.5b	5.0	107.4	5.3
Figure 7.5c	4.9	87.3	4.8

Observing the difference in peak position for the experimental and simulated curves in Figure 7.5a indicates that one or more material parameters used in the simulation differed from that of the CdO film. To investigate this difference, multiple possibilities were considered. One possible explanation involves an error in Hall Effect measurements due to the polycrystalline nature of CdO films, in which boundary domain scattering leads to lower measured mobility. Therefore, mobility and carrier concentration were allowed to vary during the subsequent simulation, fitting that of the experimental optical transmission curve. Figure 7.5b shows the new simulation produced from implementing the method described above. Although there is noticeable improvement in the simulated transmission curve compared to Figure 7.5a, a slight difference in peak position still indicates a difference in one or more CdO material parameters. Another source of error considered in our material system is the effective value of the high frequency dielectric constant ϵ_∞, compared to that of reported values. Due to the high number of boundary domains resulting from small grain size in our CdO films, non-uniform CdO density at the boundary domains of the crystallites may produce a lower average ϵ_∞. Considering a different value of $\epsilon\infty$ for our CdO films, a best fit simulation was performed in Figure 7.5c. With an average high frequency dielectric constant ϵ_∞ = 4.8, the comparison observed in Figure 7.5c reveals a 10% decrease from reported values of ϵ_∞ for cadmium oxide films.

8. SUMMARY

I. Results and Discussion

Lead selenide is a narrow bandgap semiconductor with decades of maturity dating back almost a century, with lead-chalcogenides being used in the very first applications of MWIR detectors. Despite its age, lead selenide still has a large amount of untapped potential regarding its current state of performance. Prior to this body of work, no published research had been performed on the growth of PbSe thin-films on vicinal surfaces and substrates to promote higher quality and high-yield epitaxial thin-films for enhanced device performance and throughput. Further, little research has been published on the integration of heteroepitaxial p-n junction structures using PbSe with demonstratable MWIR detectivities near room temperature operation. Here, I've explored techniques for expanding the list of suitable substrate materials for epitaxial PbSe growth through the introduction of periodic stepped surfaces using vicinal substrates, along with demonstrated detector performance at room temperature operation from an all-epitaxial p-PbSe/n-CdSe heterostructure. I have also demonstrated a method for developing MWIR transparent contacts for improved device design by optimizing a post-growth treatment process on oxygen deficient CdO films grown by DC magnetron sputtering of a compound CdO source in an oxygen-free environment. Throughout my journey as a graduate research assistant, I've had the good fortune of working hands on in a wide variety of roles, from theoretical study of semiconductor properties and device behavior to deposition and synthesis using physical and chemical growth methods, along with implementation of state-of-the-art material characterization techniques, device processing and structure design, and device testing and analysis. During this time, I explored new techniques and heterogeneous material structures, one of which led to the growth of a completely

new complex oxide thin-film, PbO_xSe_{1-x}, the results of which were published in the journal of *Crystal Growth & Design.* My efforts on the growth of epitaxial PbSe thin-films deposited directly on vicinal germanium to create a heterogenous two-color detector structure with demonstratable p-n junction behavior between severely mismatched lead selenide and germanium was also published, along with the development of a patent on this new technology. The findings from this work were also presented at the SPIE Defense & Commercial Sensing conference in Florida, and reignited interest in the IV-VI family for future MWIR sensing applications. Extending from this work, I have also demonstrated the positive impact a vicinal growth surface can have for epitaxial PbSe thin films grown on CaF_2 buffer layers on silicon substrates. The uninterrupted atomically smooth PbSe surfaces resulting from this study has produced record low growth pit and anti-phase defect densities, along with record low etch pit densities using the standard PbSe etching conditions.

II. Future Work

n-CdSe/p-PbSe Photovoltaic MWIR Detectors

The demonstration of a successful deposition of single phase (cubic) epitaxial CdSe thin-films on a single crystalline IV-VI PbSe thin-film for the first time has opened doors for a new viable material structure for near room-temperature operation MWIR photovoltaic detectors. In the work presented here, this new epitaxial heterostructure demonstrated strong p-n junction behavior and room temperature detector performance along with enhanced temperature-dependent behavior at TE-cooled operating conditions compared to previous investigations of poly-CdSe/PbSe PV detectors. However, the performance measured here was only for the

preliminary as-grown test structure for this new all epitaxial CdSe/PbSe heterostructure. For this reason, future work on optimizing the growth conditions and structure for MWIR detector applications will be extremely interesting. Optimizing the film thicknesses and doping concentrations for enhanced MWIR absorption and carrier collection should provide a positive boost to the observed detector performance. Further, implementing well developed PbSe post-growth treatment techniques such as high-temperature chloride passivation (HTCP), temperature cycling to reduce defect density, and the inclusion of an oxygen, iodine, or combination treatment conditions would find a significant improvement to the already promising device performance. Lastly, fabrication of this novel epitaxial heterostructure on commercially available material systems like silicon or germanium along with the integration of a transparent conductive contact such as CdSe:In would find a significant boost to its attractiveness for immediate applications in industry.

Exploration of Vicinal Growth

The work presented here showcased two new growth methodologies for depositing high quality epitaxial PbSe films on mismatched germanium and silicon substrates. The motivation for pursuing this initially came from other recent experimental studies of thin-film growth on vicinal surfaces, which showcased enhanced material properties on mismatched foreign substrates. However, the fundamental mechanisms which dictate the exact behavior of adatom interaction on these surfaces and their effects on the resulting bulk film are not fully understood when compared to growth models on nominal substrates. Beyond the lead selenide material system, I believe the impact of vicinal surfaces on adatom interactions and layer formation should be studied further to uncover the fundamental principles that guide their behavior. Monte-

Carlo simulations of different miscut surfaces and precursors would be a good first step in uncovering some of its behaviors. In fact, our group has initiated some effort in this area, working with the chemistry department here at the University of Oklahoma to help develop some of these models using PbSe and Ge as a first step. Further, a systematic study of different materials grown on varying degrees of miscut substrates ranging from <1° to >10° would hopefully shine light on the impact of this newly modified growth surface. Interface studies such as STM, cross-sectional TEM, strain-mapping, and defect analysis among others are all important investigation techniques that would be helpful for improving our current growth models. Since lead selenide in particular has suffered largely due to its lack of a suitable substrate selection for high-yield high quality epitaxial films, I predict that future work in this area would find immediate applications in the MWIR sensing and imaging community.

Funding

Throughout the dissertation period, this dissertation work was supported by the US army research office (ARO) under Grant No. W911NF-14-1-0312, and W911NF-18-1-0418, Oklahoma Center for the Advancement of Science and Technology (OCAST) under Grant No. AR14-035, AR132-003, and by the US DARPA WIRED program through Northrop Grumman.

References

[1] G. Lucovsky and R. M. White, “Effects of Resonance Bonding on the Properties of Crystalline and Amorphous Semiconductors,” *Phys. Rev. B*, vol. 8, no. 2, pp. 660–667, Jul. 1973, doi: 10.1103/PhysRevB.8.660.

[2] P. K. Cheo, Ed., *Handbook of solid-state lasers*. New York: M. Dekker, 1989.

[3] B. Weng, J. Qiu, L. Zhao, C. Chang, and Z. Shi, “CdS/PbSe heterojunction for high temperature mid-infrared photovoltaic detector applications,” *Appl. Phys. Lett.*, vol. 104, no. 12, Art. no. 12, Mar. 2014, doi: 10.1063/1.4869752.

[4] J. Venables, *Introduction to surface and thin film processes*. Cambrige, UK ; New York: Cambridge University Press, 2000.

[5] R. Dalven, “Electronic Structure of PbS, PbSe, and PbTe,” in *Solid State Physics*, vol. 28, Elsevier, 1974, pp. 179–224. doi: 10.1016/S0081-1947(08)60203-9.

[6] A. Y. Ueta, G. Springholz, F. Schinagl, G. Marschner, and G. Bauer, “Doping studies for molecular beam epitaxy of PbTe and Pb1 − xEuxTe,” *Thin Solid Films*, vol. 306, no. 2, pp. 320–325, Sep. 1997, doi: 10.1016/S0040-6090(97)00239-3.

[7] X. J. Wang *et al.*, “Heteroepitaxy of PbSe on GaAs(100) and GaAs(211)B by molecular beam epitaxy,” *Journal of Crystal Growth*, vol. 311, no. 8, pp. 2359–2362, Apr. 2009, doi: 10.1016/j.jcrysgro.2009.01.140.

[8] B. B. Haidet, E. T. Hughes, and K. Mukherjee, “Nucleation control and interface structure of rocksalt PbSe on (001) zincblende III-V surfaces,” *Phys. Rev. Materials*, vol. 4, no. 3, p. 033402, Mar. 2020, doi: 10.1103/PhysRevMaterials.4.033402.

[9] B. B. Haidet *et al.*, “Interface structure and luminescence properties of epitaxial PbSe films on InAs(111)A,” *Journal of Vacuum Science & Technology A*, vol. 39, no. 2, p. 023404, Mar. 2021, doi: 10.1116/6.0000774.

[10] J. Qiu, B. Weng, Z. Yuan, and Z. Shi, “Study of sensitization process on mid-infrared uncooled PbSe photoconductive detectors leads to high detectivity,” *Journal of Applied Physics*, vol. 113, no. 10, Art. no. 10, Mar. 2013, doi: 10.1063/1.4794492.

[11] “Park Systems AFM.” https://parksystems.com/cn/AFM_gallery/AFM_gallery_view.php?id=91&word=Nano

[12] A. Fach, J. John, P. Müller, C. Paglino, and H. Zogg, “Material properties of Pb1-xSnxSe epilayers on Si and their correlation with the performance of infrared photodiodes,” *Journal of Elec Materi*, vol. 26, no. 7, pp. 873–877, Jul. 1997, doi: 10.1007/s11664-997-0266-6.

[13] H. Preier, “Recent advances in lead-chalcogenide diode lasers,” *Appl. Phys.*, vol. 20, no. 3, pp. 189–206, Nov. 1979, doi: 10.1007/BF00886018.

[14] E. Pedrueza, A. Segura, R. Abargues, J. B. Bailach, J. C. Chervin, and J. P. Martínez-Pastor, “The effect of quantum size confinement on the optical properties of PbSe nanocrystals as a function of temperature and hydrostatic pressure,” *Nanotechnology*, vol. 24, no. 20, p. 205701, May 2013, doi: 10.1088/0957-4484/24/20/205701.

[15] J. Qiu, B. Weng, L. L. McDowell, and Z. Shi, “Low-cost uncooled MWIR PbSe quantum dots photodiodes,” *RSC Adv.*, vol. 9, no. 72, Art. no. 72, 2019, doi: 10.1039/C9RA07664F.

[16] X. Shi *et al.*, “Study on the Theoretical Limitation of the Mid-Infrared PbSe N⁺-P Junction Detectors at High Operating Temperature,” *Detection*, vol. 06, no. 01, Art. no. 01, 2018, doi: 10.4236/detection.2018.61001.

[17] R. Q. Yang, “Shot and Johnson noises in interband cascade infrared photodetectors,” *Appl. Phys. Lett.*, vol. 121, no. 5, p. 051105, Aug. 2022, doi: 10.1063/5.0103661.

[18] Jö. Hader, J. V. Moloney, and S. W. Koch, “Temperature Dependence of Radiative and Auger Losses in Quantum Wells,” *IEEE J. Quantum Electron.*, vol. 44, no. 2, pp. 185–191, Feb. 2008, doi: 10.1109/JQE.2007.910938.
[19] A. J. E. Rettie *et al.*, “Combined Charge Carrier Transport and Photoelectrochemical Characterization of $BiVO_4$ Single Crystals: Intrinsic Behavior of a Complex Metal Oxide,” *J. Am. Chem. Soc.*, vol. 135, no. 30, pp. 11389–11396, Jul. 2013, doi: 10.1021/ja405550k.
[20] J. Lee, H. Zhu, G. G. Yadav, J. Caruthers, and Y. Wu, “Porous ternary complex metal oxide nanoparticles converted from core/shell nanoparticles,” *Nano Res.*, vol. 9, no. 4, pp. 996–1004, Apr. 2016, doi: 10.1007/s12274-016-0987-z.
[21] L. Zhang *et al.*, “Correlated metals as transparent conductors,” *Nature Mater*, vol. 15, no. 2, pp. 204–210, Feb. 2016, doi: 10.1038/nmat4493.
[22] Q. X. Jia *et al.*, “Polymer-assisted deposition of metal-oxide films,” *Nature Mater*, vol. 3, no. 8, pp. 529–532, Aug. 2004, doi: 10.1038/nmat1163.
[23] H.-U. Habermeier, “Thin films of perovskite-type complex oxides,” *Materials Today*, vol. 10, no. 10, pp. 34–43, Oct. 2007, doi: 10.1016/S1369-7021(07)70243-2.
[24] K. Nomura, H. Ohta, A. Takagi, T. Kamiya, M. Hirano, and H. Hosono, “Room-temperature fabrication of transparent flexible thin-film transistors using amorphous oxide semiconductors,” *Nature*, vol. 432, no. 7016, pp. 488–492, Nov. 2004, doi: 10.1038/nature03090.
[25] A. Muñoz *et al.*, “PbSe photodetector arrays for IR sensors,” *Thin Solid Films*, vol. 317, no. 1–2, pp. 425–428, Apr. 1998, doi: 10.1016/S0040-6090(97)00576-2.
[26] F. Zhao, S. Mukherjee, J. Ma, D. Li, S. L. Elizondo, and Z. Shi, “Influence of oxygen passivation on optical properties of PbSe thin films,” *Appl. Phys. Lett.*, vol. 92, no. 21, p. 211110, May 2008, doi: 10.1063/1.2938417.
[27] L. Zhao, J. Qiu, B. Weng, C. Chang, Z. Yuan, and Z. Shi, “Understanding sensitization behavior of lead selenide photoconductive detectors by charge separation model,” *Journal of Applied Physics*, vol. 115, no. 8, Art. no. 8, Feb. 2014, doi: 10.1063/1.4867038.
[28] B. Weng, J. Qiu, L. Zhao, Z. Yuan, C. Chang, and Z. Shi, “Recent development on the uncooled mid-infrared PbSe detectors with high detectivity,” San Francisco, California, United States, Dec. 2013, p. 899311. doi: 10.1117/12.2041276.
[29] C. E. Ekuma, D. J. Singh, J. Moreno, and M. Jarrell, “Optical properties of PbTe and PbSe,” *Phys. Rev. B*, vol. 85, no. 8, p. 085205, Feb. 2012, doi: 10.1103/PhysRevB.85.085205.
[30] J. Berashevich, O. Semeniuk, J. A. Rowlands, and A. Reznik, “Anisotropy of the carrier effective masses in bulk α -PbO,” *EPL*, vol. 99, no. 4, p. 47005, Aug. 2012, doi: 10.1209/0295-5075/99/47005.
[31] K. Iinuma, T. Seki, and M. Wada, “Optical absorption coefficients of lead monoxide single crystal of the yellow modification,” *Materials Research Bulletin*, vol. 2, no. 5, pp. 527–532, May 1967, doi: 10.1016/0025-5408(67)90028-1.
[32] V. V. Tomaev, V. D. Smolyaninov, T. V. Stoyanova, and S. V. Egorov, “Preparation of $PbSeO_3$ as a new material, sensitive to the electromagnetic radiation in UV range,” *J. Phys.: Conf. Ser.*, vol. 741, p. 012036, Aug. 2016, doi: 10.1088/1742-6596/741/1/012036.
[33] D. Errandonea, A. Muñoz, P. Rodríguez-Hernández, J. E. Proctor, F. Sapiña, and M. Bettinelli, “Theoretical and Experimental Study of the Crystal Structures, Lattice Vibrations, and Band Structures of Monazite-Type $PbCrO_4$, $PbSeO_4$, $SrCrO_4$, and $SrSeO_4$,” *Inorg. Chem.*, vol. 54, no. 15, pp. 7524–7535, Aug. 2015, doi: 10.1021/acs.inorgchem.5b01135.

[34] X. Sun, K. Gao, X. Pang, H. Yang, and A. A. Volinsky, “Study on the growth mechanism and optical properties of sputtered lead selenide thin films,” *Applied Surface Science*, vol. 356, pp. 978–985, Nov. 2015, doi: 10.1016/j.apsusc.2015.08.195.
[35] D. Kazantsev, Y. Selivanov, V. Trofimov, and E. Chizhevskii, “Surface States of Lead Selenide Crystals,” *AIP*, vol. 62, no. 5, pp. 422–426, 1995.
[36] M. O. Kuzivanov, S. P. Zimin, A. V. Fedorov, and A. V. Baranov, “Raman scattering in lead selenide films at a low excitation level,” *Opt. Spectrosc.*, vol. 119, no. 6, pp. 938–942, Dec. 2015, doi: 10.1134/S0030400X15120140.
[37] X. Yang, Y. Liu, X. J. Liu, J. Z. Peng, H. Zhao, and C. Q. Sun, “Composition- and Temperature-Resolved Raman Shift of Silicon,” *Appl Spectrosc*, vol. 72, no. 4, pp. 598–603, Apr. 2018, doi: 10.1177/0003702817744218.
[38] C. Gautier, M. Cambon-Muller, and M. Averous, “Study of PbSe layer oxidation and oxide dissolution,” *Applied Surface Science*, vol. 141, no. 1–2, pp. 157–163, Mar. 1999, doi: 10.1016/S0169-4332(98)00606-0.
[39] H. F. Yang, W. Z. Shen, and Q. J. Pang, “Study of photocurrent characteristics in PbSrSe thin films for infrared detection,” *Appl. Phys. Lett.*, vol. 81, no. 13, pp. 2394–2396, Sep. 2002, doi: 10.1063/1.1509474.
[40] D. L. Partin, “Lead salt quantum effect structures,” *IEEE J. Quantum Electron.*, vol. 24, no. 8, pp. 1716–1726, Aug. 1988, doi: 10.1109/3.7102.
[41] M. Tacke, “New developments and applications of tunable IR lead salt lasers,” *Infrared Physics & Technology*, vol. 36, no. 1, Art. no. 1, Jan. 1995, doi: 10.1016/1350-4495(94)00101-P.
[42] B. Weng *et al.*, “Room temperature mid-infrared surface-emitting photonic crystal laser on silicon,” *Appl. Phys. Lett.*, vol. 99, no. 22, Art. no. 22, Nov. 2011, doi: 10.1063/1.3665402.
[43] H. Zogg, “Epitaxial lead-chalcogenide on silicon layers for thermal imaging applications,” Kiev, Ukraine, Nov. 1999, pp. 22–26. doi: 10.1117/12.368352.
[44] J. J. Choi *et al.*, “PbSe Nanocrystal Excitonic Solar Cells,” *Nano Lett.*, vol. 9, no. 11, Art. no. 11, Nov. 2009, doi: 10.1021/nl901930g.
[45] E. O. Wrasse and T. M. Schmidt, “Prediction of Two-Dimensional Topological Crystalline Insulator in PbSe Monolayer,” *Nano Lett.*, vol. 14, no. 10, Art. no. 10, Oct. 2014, doi: 10.1021/nl502481f.
[46] J. M. Woodall, “Heterogeneous integration of semiconductor materials: basic issues, current progress, and future prospects,” Baltimore, Maryland, USA, May 2012, p. 83731B. doi: 10.1117/12.917911.
[47] P. Müller, A. Fach, J. John, A. N. Tiwari, H. Zogg, and G. Kostorz, “Structure of epitaxial PbSe grown on Si(111) and Si(100) without a fluoride buffer layer,” *Journal of Applied Physics*, vol. 79, no. 4, pp. 1911–1916, Feb. 1996, doi: 10.1063/1.361076.
[48] S. Jin, C. Cai, G. Bi, B. Zhang, H. Wu, and Y. Zhang, “Two-dimensional electron gas at the metastable twisted interfaces of CdTe/PbTe (111) single heterojunctions,” *Phys. Rev. B*, vol. 87, no. 23, Art. no. 23, Jun. 2013, doi: 10.1103/PhysRevB.87.235315.
[49] X. J. Wang *et al.*, “Characterization of PbSnSe/CdTe/Si (211) Epilayers Grown by Molecular Beam Epitaxy,” *Journal of Elec Materi*, vol. 37, no. 9, Art. no. 9, Sep. 2008, doi: 10.1007/s11664-008-0480-x.

[50] S. Chusnutdinow, S. Schreyeck, S. Kret, A. Kazakov, and G. Karczewski, “Room temperature infrared detectors made of PbTe/CdTe multilayer composite,” *Appl. Phys. Lett.*, vol. 117, no. 7, Art. no. 7, Aug. 2020, doi: 10.1063/5.0018686.
[51] A. Pashaev, O. Davarashvili, Z. Akhvlediani, M. Enukashvili, R. Gulyaev, and V. Zlomanov, “Unrelaxed State in Epitaxial Heterostructures Based on Lead Selenide,” *JMP*, vol. 03, no. 06, pp. 502–510, 2012, doi: 10.4236/jmp.2012.36068.
[52] X. J. Wang *et al.*, “Heteroepitaxy of PbSe on GaAs(100) and GaAs(211)B by molecular beam epitaxy,” *Journal of Crystal Growth*, vol. 311, no. 8, pp. 2359–2362, Apr. 2009, doi: 10.1016/j.jcrysgro.2009.01.140.
[53] B. B. Haidet, E. T. Hughes, and K. Mukherjee, “Nucleation control and interface structure of rocksalt PbSe on (001) zincblende III-V surfaces,” *Phys. Rev. Materials*, vol. 4, no. 3, p. 033402, Mar. 2020, doi: 10.1103/PhysRevMaterials.4.033402.
[54] B. B. Haidet *et al.*, “Interface structure and luminescence properties of epitaxial PbSe films on InAs(111)A,” *Journal of Vacuum Science & Technology A*, vol. 39, no. 2, p. 023404, Mar. 2021, doi: 10.1116/6.0000774.
[55] Z. Shao *et al.*, “Epitaxial Growth of PbSe Few-Layers on $SrTiO_3$: The Effect of Compressive Strain and Potential Two-Dimensional Topological Crystalline Insulator,” *ACS Nano*, p. acsnano.9b00072, Feb. 2019, doi: 10.1021/acsnano.9b00072.
[56] K. Green, S.-S. Yoo, and C. Kauffman, “Lead salt TE-cooled imaging sensor development,” Baltimore, Maryland, USA, Jun. 2014, p. 90701G. doi: 10.1117/12.2053302.
[57] B. Weng, J. Qiu, Z. Yuan, P. R. Larson, G. W. Strout, and Z. Shi, “Responsivity enhancement of mid-infrared PbSe detectors using CaF_2 nano-structured antireflective coatings,” *Appl. Phys. Lett.*, vol. 104, no. 2, Art. no. 2, Jan. 2014, doi: 10.1063/1.4861186.
[58] R. Klann, T. Höfer, R. Buhleier, T. Elsaesser, and J. W. Tomm, “Fast recombination processes in lead chalcogenide semiconductors studied via transient optical nonlinearities,” *Journal of Applied Physics*, vol. 77, no. 1, Art. no. 1, Jan. 1995, doi: 10.1063/1.359388.
[59] P. C. Findlay *et al.*, “Auger recombination dynamics of lead salts under picosecond free-electron-laser excitation,” *Phys. Rev. B*, vol. 58, no. 19, Art. no. 19, Nov. 1998, doi: 10.1103/PhysRevB.58.12908.
[60] O. Ziep, M. Mocker, D. Genzow, and K. H. Herrmann, “Auger recombination in PbSnTe-like semiconductors,” *Phys. Stat. Sol. (b)*, vol. 90, no. 1, Art. no. 1, Nov. 1978, doi: 10.1002/pssb.2220900121.
[61] E. R. Youngdale *et al.*, “Auger lifetime enhancement in InAs–Ga_{1-x} In_x Sb superlattices,” *Appl. Phys. Lett.*, vol. 64, no. 23, Art. no. 23, Jun. 1994, doi: 10.1063/1.111325.
[62] J. R. Meyer *et al.*, “Auger coefficients in type-II InAs/Ga1−xInxSb quantum wells,” *Appl. Phys. Lett.*, vol. 73, no. 20, Art. no. 20, Nov. 1998, doi: 10.1063/1.122609.
[63] C. M. Ciesla *et al.*, “Auger recombination dynamics of Hg0.795Cd0.205Te in the high excitation regime,” *Appl. Phys. Lett.*, vol. 71, no. 4, Art. no. 4, Jul. 1997, doi: 10.1063/1.119588.
[64] A. R. Beattie and A. M. White, “An analytic approximation with a wide range of applicability for electron initiated Auger transitions in narrow-gap semiconductors,” *J. Appl. Phys.*, vol. 79, no. 2, Art. no. 2, 1996, doi: 10.1063/1.360828.
[65] C. Misbah, O. Pierre-Louis, and Y. Saito, “Crystal surfaces in and out of equilibrium: A modern view,” *Rev. Mod. Phys.*, vol. 82, no. 1, Art. no. 1, Mar. 2010, doi: 10.1103/RevModPhys.82.981.

[66] Nils. A. K. Kaufmann, L. Lahourcade, B. Hourahine, D. Martin, and N. Grandjean, "Critical impact of Ehrlich–Schwöbel barrier on GaN surface morphology during homoepitaxial growth," *Journal of Crystal Growth*, vol. 433, pp. 36–42, Jan. 2016, doi: 10.1016/j.jcrysgro.2015.06.013.
[67] T. N. Xu, H. Z. Wu, J. X. Si, and C. F. Cao, "Observation of triangle pits in PbSe grown by molecular beam epitaxy," *Applied Surface Science*, vol. 253, no. 12, pp. 5457–5461, Apr. 2007, doi: 10.1016/j.apsusc.2006.12.028.
[68] X. M. Fang, "Molecular beam epitaxial growth of Bi[sub 2]Se[sub 3]- and Tl[sub 2]Se-doped PbSe and PbEuSe on CaF[sub 2]/Si(111)," *J. Vac. Sci. Technol. B*, vol. 16, no. 3, p. 1459, May 1998, doi: 10.1116/1.589965.
[69] F. Zhao, H. Wu, A. Majumdar, and Z. Shi, "Continuous wave optically pumped lead-salt mid-infrared quantum-well vertical-cavity surface-emitting lasers," *Appl. Phys. Lett.*, vol. 83, no. 25, pp. 5133–5135, Dec. 2003, doi: 10.1063/1.1636246.
[70] P. Müller, A. N. Tiwari, and H. Zogg, "Growth and properties of epitaxial PbSe on Si(111) and Si(100) without buffer layer," *MRS Proc.*, vol. 379, p. 133, 1995, doi: 10.1557/PROC-379-133.
[71] H. Z. Wu, X. M. Fang, R. Salas, D. McAlister, and P. J. McCann, "Molecular beam epitaxy growth of PbSe on BaF[sub 2]-coated Si(111) and observation of the PbSe growth interface," *J. Vac. Sci. Technol. B*, vol. 17, no. 3, p. 1263, 1999, doi: 10.1116/1.590736.
[72] Y. Luo, L. McDowell, L. Su, Y. Liu, J. Qiu, and Z. Shi, "Enhanced performance in uncooled n-CdSe/p-PbSe photovoltaic detectors by high-temperature chloride passivation," *RSC Adv.*, vol. 12, no. 14, pp. 8423–8428, 2022, doi: 10.1039/D2RA00483F.
[73] H. Zogg, "Dislocation Reduction by Glide in Epitaxial IV–VI Layers on Si Substrates," *Journal of Elec Materi*, vol. 41, no. 7, pp. 1931–1935, Jul. 2012, doi: 10.1007/s11664-012-2031-8.
[74] B. Weng, F. Zhao, J. Ma, G. Yu, J. Xu, and Z. Shi, "Elimination of threading dislocations in as-grown PbSe film on patterned Si(111) substrate using molecular beam epitaxy," *Appl. Phys. Lett.*, vol. 96, no. 25, p. 251911, Jun. 2010, doi: 10.1063/1.3457863.
[75] F. Zhao *et al.*, "MBE growth of PbSe thin film with a 9×105cm−2 etch-pits density on patterned (111)-oriented Si substrate," *Journal of Crystal Growth*, vol. 312, no. 19, pp. 2695–2698, Sep. 2010, doi: 10.1016/j.jcrysgro.2010.05.041.
[76] J. G. Ma *et al.*, "Growth mechanism of cuboid growth pits in lead selenide epilayers grown by molecular beam epitaxy," *J. Phys. D: Appl. Phys.*, vol. 43, no. 45, p. 455411, Nov. 2010, doi: 10.1088/0022-3727/43/45/455411.
[77] J. Ma *et al.*, "Nature of Growth Pits in Lead Salt Epilayers Grown by Molecular Beam Epitaxy," *Journal of Elec Materi*, vol. 38, no. 2, pp. 325–329, Feb. 2009, doi: 10.1007/s11664-008-0566-5.
[78] L. L. McDowell, J. Qiu, M. R. Mirzaei, B. Weng, and Z. Shi, "Integration of Epitaxial IV–VI Pb-Chalcogenide on Group IV Vicinal Ge Substrate to Form p–n Heterogeneous Structures," *Crystal Growth & Design*, vol. 22, no. 1, pp. 461–468, Jan. 2022, doi: 10.1021/acs.cgd.1c01074.
[79] M. O. Petrushkov *et al.*, "Effect of the Crystallographic Orientation of GaSb Films on Their Structural Properties during MBE Heteroepitaxy on Vicinal Si(001) Substrates," *Semiconductors*, vol. 54, no. 12, pp. 1548–1554, Dec. 2020, doi: 10.1134/S1063782620120295.

[80] S. M. Hubbard, A. Podell, C. Mackos, S. Polly, C. G. Bailey, and D. V. Forbes, “Effect of vicinal substrates on the growth and device performance of quantum dot solar cells,” *Solar Energy Materials and Solar Cells*, vol. 108, pp. 256–262, Jan. 2013, doi: 10.1016/j.solmat.2012.09.026.
[81] J. Qiu, Y. Liu, Z. Cai, Q. Phan, and Z. Shi, “CdSe:In Mid-Infrared Transparent Conductive Films Prospering Uncooled PbSe/CdSe Heterojunction Photovoltaic Detectors,” *Mater. Adv.*, p. 10.1039.D1MA00760B, 2021, doi: 10.1039/D1MA00760B.
[82] M. Ates *et al.*, “An Evaluation Research About Effects of Characterized Cadmium Selenide (CdSe) and Lead Selenide (PbSe) Quantum Dots on Brine Shrimp (Artemia salina),” *Bull Environ Contam Toxicol*, vol. 105, no. 3, pp. 372–380, Sep. 2020, doi: 10.1007/s00128-020-02941-7.
[83] E. Sachet *et al.*, “Dysprosium-doped cadmium oxide as a gateway material for mid-infrared plasmonics,” *Nature Mater*, vol. 14, no. 4, pp. 414–420, Apr. 2015, doi: 10.1038/nmat4203.
[84] B. Saha, S. Das, and K. K. Chattopadhyay, “Electrical and optical properties of Al doped cadmium oxide thin films deposited by radio frequency magnetron sputtering,” *Solar Energy Materials and Solar Cells*, vol. 91, no. 18, pp. 1692–1697, Nov. 2007, doi: 10.1016/j.solmat.2007.05.025.
[85] R. Ferro and J. A. Rodríguez, “Influence of F-doping on the transmittance and electron affinity of CdO thin films suitable for solar cells technology,” *Solar Energy Materials and Solar Cells*, vol. 64, no. 4, pp. 363–370, Nov. 2000, doi: 10.1016/S0927-0248(00)00228-2.
[86] T. K. Subramanyam, G. Mohan Rao, and S. Uthanna, “Process parameter dependent property studies on CdO films prepared by DC reactive magnetron sputtering,” *Materials Chemistry and Physics*, vol. 69, no. 1–3, pp. 133–142, Mar. 2001, doi: 10.1016/S0254-0584(00)00376-X.
[87] X. Shi, “Research Progress on the Photoelectric Properties of Indium-Doped Cadmium Oxide Transparent Conductive Films,” *IOP Conf. Ser.: Mater. Sci. Eng.*, vol. 914, no. 1, p. 012007, Sep. 2020, doi: 10.1088/1757-899X/914/1/012007.
[88] B.-J. Kim, Y.-W. Ok, T.-Y. Seong, A. B. M. A. Ashrafi, H. Kumano, and I. Suemune, “Structural properties of CdO layers grown on GaAs (001) substrates by metalorganic molecular beam epitaxy,” *Journal of Crystal Growth*, vol. 252, no. 1–3, pp. 219–225, May 2003, doi: 10.1016/S0022-0248(02)02521-6.
[89] K. Ellmer, “Past achievements and future challenges in the development of optically transparent electrodes,” *Nature Photon*, vol. 6, no. 12, pp. 809–817, Dec. 2012, doi: 10.1038/nphoton.2012.282.
[90] D. S. Ginley, H. Hosono, and D. C. Paine, Eds., *Handbook of transparent conductors*. New York: Springer, 2010.
[91] A. N. Banerjee and K. K. Chattopadhyay, “Recent developments in the emerging field of crystalline p-type transparent conducting oxide thin films,” *Progress in Crystal Growth and Characterization of Materials*, vol. 50, no. 1–3, pp. 52–105, Jan. 2005, doi: 10.1016/j.pcrysgrow.2005.10.001.
[92] C. H. Champness and C. H. Chan, “Optimization of CdO layer in a Se□CdO photovoltaic cell,” *Solar Energy Materials and Solar Cells*, vol. 37, no. 1, pp. 75–92, Apr. 1995, doi: 10.1016/0927-0248(94)00199-5.

[93] D. J. Farrell, Y. Takeda, K. Nishikawa, T. Nagashima, T. Motohiro, and N. J. Ekins-Daukes, “A hot-carrier solar cell with optical energy selective contacts,” *Appl. Phys. Lett.*, vol. 99, no. 11, p. 111102, Sep. 2011, doi: 10.1063/1.3636401.
[94] M. Soylu and H. S. Kader, “Photodiode Based on CdO Thin Films as Electron Transport Layer,” *Journal of Elec Materi*, vol. 45, no. 11, pp. 5756–5763, Nov. 2016, doi: 10.1007/s11664-016-4819-4.
[95] F. A. Benko and F. P. Koffyberg, “Quantum efficiency and optical transitions of CdO photoanodes,” *Solid State Communications*, vol. 57, no. 12, pp. 901–903, Mar. 1986, doi: 10.1016/0038-1098(86)90920-8.
[96] D. Langley, G. Giusti, C. Mayousse, C. Celle, D. Bellet, and J.-P. Simonato, “Flexible transparent conductive materials based on silver nanowire networks: a review,” *Nanotechnology*, vol. 24, no. 45, p. 452001, Nov. 2013, doi: 10.1088/0957-4484/24/45/452001.
[97] J. Du, S. Pei, L. Ma, and H.-M. Cheng, “25th Anniversary Article: Carbon Nanotube- and Graphene-Based Transparent Conductive Films for Optoelectronic Devices,” *Adv. Mater.*, vol. 26, no. 13, pp. 1958–1991, Apr. 2014, doi: 10.1002/adma.201304135.
[98] J. A. Frantz, V. Q. Nguyen, A. J. Mäkinen, S. B. Qadri, J. D. Myers, and J. S. Sanghera, “Low-temperature deposition of BaCuSF, a visible through mid-infrared p-type transparent conductor,” *Opt. Express*, vol. 21, no. 25, p. 30674, Dec. 2013, doi: 10.1364/OE.21.030674.
[99] D. Sivalingam, J. B. Gopalakrishnan, and J. B. B. Rayappan, “Nanostructured mixed ZnO and CdO thin film for selective ethanol sensing,” *Materials Letters*, vol. 77, pp. 117–120, Jun. 2012, doi: 10.1016/j.matlet.2012.03.009.
[100] T. K. Subramanyam, B. Srinivasulu Naidu, and S. Uthanna, “Studies on dc magnetron sputtered cadmium oxide films,” *Applied Surface Science*, vol. 169–170, pp. 529–534, Jan. 2001, doi: 10.1016/S0169-4332(00)00714-5.
[101] A. J. Varkey and A. F. Fort, “Transparent conducting cadmium oxide thin films prepared by a solution growth technique,” *Thin Solid Films*, vol. 239, no. 2, pp. 211–213, Mar. 1994, doi: 10.1016/0040-6090(94)90853-2.
[102] G. Phatak and R. Lal, “Deposition and properties of cadmium oxide films by activated reactive evaporation,” *Thin Solid Films*, vol. 245, no. 1–2, pp. 17–26, Jun. 1994, doi: 10.1016/0040-6090(94)90871-0.
[103] *ICDD PDF4+ Database*. [Online]. Available: https://www.icdd.com/pdf-4/
[104] D. Ma, Z. Ye, L. Wang, J. Huang, and B. Zhao, “Deposition and characteristics of CdO films with absolutely (200)-preferred orientation,” *Materials Letters*, vol. 58, no. 1–2, pp. 128–131, Jan. 2004, doi: 10.1016/S0167-577X(03)00429-4.
[105] K. M. Yu *et al.*, “Defects and properties of cadmium oxide based transparent conductors,” *Journal of Applied Physics*, vol. 119, no. 18, p. 181501, May 2016, doi: 10.1063/1.4948236.
[106] R. Díaz, J. M. Merino, T. Martín, F. Rueda, and M. León, “An approach to the energy gap determination from reflectance measurements,” *Journal of Applied Physics*, vol. 83, no. 1, pp. 616–618, Jan. 1998, doi: 10.1063/1.366650.
[107] N. Manjula, A. R. Balu, K. Usharani, N. Raja, and V. S. Nagarethinam, “Enhancement in some physical properties of spray deposited CdO:Mn thin films through Zn doping towards optoelectronic applications,” *Optik*, vol. 127, no. 16, pp. 6400–6406, Aug. 2016, doi: 10.1016/j.ijleo.2016.04.129.

[108] I. H. Malitson, “A Redetermination of Some Optical Properties of Calcium Fluoride,” *Appl. Opt.*, vol. 2, no. 11, p. 1103, Nov. 1963, doi: 10.1364/AO.2.001103.
[109] G. J. Exarhos and X.-D. Zhou, “Discovery-based design of transparent conducting oxide films,” *Thin Solid Films*, vol. 515, no. 18, pp. 7025–7052, Jun. 2007, doi: 10.1016/j.tsf.2007.03.014.
[110] P. H. Jefferson *et al.*, “Bandgap and effective mass of epitaxial cadmium oxide,” *Appl. Phys. Lett.*, vol. 92, no. 2, p. 022101, Jan. 2008, doi: 10.1063/1.2833269.
[111] E. Sachet, M. D. Losego, J. Guske, S. Franzen, and J.-P. Maria, “Mid-infrared surface plasmon resonance in zinc oxide semiconductor thin films,” *Appl. Phys. Lett.*, vol. 102, no. 5, p. 051111, Feb. 2013, doi: 10.1063/1.4791700.